Effect of acoustic resonance on the dynamic lift in square tube arrays

Effect of acoustic resonance on the dynamic lift in square tube arrays

By

Ronald E. Hanson, B.Eng.

A Thesis

Submitted to the School of Graduate Studies

in Partial Fulfilment of the Requirements

for the Degree

Master of Applied Science

McMaster University

MASTER OF APPLIED SCIENCE (2007) McMaster University

(Department of Mechanical Engineering) Hamilton, Ontario

TITLE: Effect of acoustic resonance on the dynamic lift in square tube arrays

AUTHOR: Ronald Hanson, B.Eng.

SUPERVISOR: Samir Ziada

NUMBER OF PAGES: xv, 122

Abstract

An investigation of the dynamic lift on the central tube in square tube arrays is conducted. Three array spacing ratios with $P/D = 3.37$, 2.18 and 1.58, corresponding to large, intermediate and small spacing ratios are investigated. These three classes exhibit specific flow characteristics and distinct behavior during acoustic resonance. The aim of the present investigation is to determine the effect of the acoustic pressure field and its contribution to dynamic lift during acoustic resonance.

During acoustic resonance there are two sources of dynamic lift. One source is provided by the sound field. The standing wave excited during resonance causes dynamic lift from the acoustic pressure distribution on the surface of the cylinder. In the absence of flow, loud speakers are used to excite the first transverse acoustic mode over a range of sound pressure levels, effectively determining the relationship between the resultant dynamic lift and sound pressure level of the acoustic standing wave. The dynamic lift due to the sound field is well predicted by numerical simulation of the acoustic pressure distribution in the tube array. Using the validated numerical simulation it is possible to extend the results to a large range of cylinder diameter to wavelength ratios. The other source of dynamic lift is provided by the periodic flow though the tube array, known as vortex shedding, which is enhanced during resonance.

The total dynamic lift is dependant on the phase shift between the sound field and aerodynamic lift components. For small and intermediate tube arrays, acoustic resonance occurs before coincidence of the natural vortex shedding frequency and the acoustic mode. For the large tube array, frequency coincidence occurs within the resonance range. The phase shift between the dynamic lift due to sound and that due to the aerodynamic lift is small for the pre-coincidence resonance range observed

for small and intermediate tube arrays and therefore the total dynamic lift is well predicted by the sum of the magnitudes of the dynamic lift due to the sound field and aerodynamic lift components caused by vortex shedding. Past the frequency of coincidence, a phase jump occurs in the aerodynamic lift causing a large phase shift between the sound field and aerodynamic lift components in the large spacing ratio array. The summation of the aerodynamic lift and the lift due to the sound field over predicts the total dynamic lift measured during acoustic resonance in this case. The present results are used to develop a conservative guideline for estimating the total dynamic lift during acoustic resonance.

Acknowledgements

The author would like to acknowledge the guidance and support of his supervisor, Professor Samir Ziada. Professor Ziada has contributed much time in the development of this project, as well as guidance in areas pertaining to future career goals and the steps necessary to achieve them, wherein his advice is second to none.

The author would also like to recognize his friends and family, their involvement has enhanced the quality of the time spent at McMaster University, making it as socially rewarding as it was academically. The Deep Homers in conjunction with the GSA softball league made the summers very exciting and entertaining; faculty and staff, within the department have created an environment at McMaster which is friendly and encouraging.

Staff of the mechanical engineering machine shops have supplied me with hands on skills in engineering design and fabrication for the experimental setup manufactured for this project.

dedicated to my family

Table of Contents

List of Figures

List of Tables

Chapter 1

Introduction

Unsteady periodic flow is generated in the wake of bluff bodies such as a circular cylinder. These periodic flows cause dynamic pressure loading on the surface of the cylinder resulting in periodic lift forces in the direction normal to the flow and cylinder axis. The dynamic lift force is generally an order of magnitude larger than that in the direction parallel to the flow. In tube arrays, typical to those in heat exchangers and boilers, the dynamic lift forces are also dominant. Similar to dynamic loading, sound is generated proportional to the dynamic lift and drag as a dipole like source (Phillips, 1956). The sound generated by periodic vortex shedding enhances the acoustic mode as it nears the acoustic mode frequency. The sound field of the acoustic mode enhances the process of vortex shedding leading to a feedback cycle which causes synchronization of the acoustic mode and the vortex shedding frequency at the frequency of the acoustic mode. The dominant sound source from vortex shedding is in the lift direction and therefore the most susceptible natural acoustic modes are transverse modes of the duct housing the bluff body. This excitation mechanism and subsequent acoustic resonance is well understood for such cases as the single cylinder, see for example Blevins and Bressler (1993) or Mohany and Ziada (2005), and has also been investigated and characterized in tube arrays (Oengören and Ziada 1992b).

Of particular interest are the consequences of acoustic resonance on the dynamic lift in tube arrays. Before the onset of acoustic resonance in tube arrays, the lift coef-

ficients have been determined, see for example Chen and Jendrzejczyk (1987), Axisa et al. (1988), Oengören and Ziada (1992) and Inada et al. (2007). During acoustic resonance, measurements of the dynamic lift are yet to be determined, and are the focus of the present investigation. Mohany and Ziada (2006) recently measured the dynamic lift coefficients for a single cylinder in non-resonance conditions and during flow-excited acoustic resonance. The results show that the dynamic lift coefficient can increase by a factor of four during flow-excited acoustic resonance in some of the cases. For tandem cylinders, studied by Mohany and Ziada (2006), similar increases in the lift coefficients were observed. These results indicate the necessity of determining the dynamic lift in tube arrays during acoustic resonance. For single and tandem cylinders, the lift coefficients are large compared to those in arrays of cylinders. In these examples, the aerodynamic lift generated by the flow is very large compared to the effects of sound. It is expected that the pressure field of the acoustic mode will have a more dominate role in the dynamic lift on the cylinders in tube arrays.

Design of heat exchangers and boilers requires a good working knowledge of the forces acting on the tubes for estimating the service life. Fatigue limits and estimates of the service life are highly based on knowing these dynamic loads. Furthermore, underestimation of the dynamic loading can be hazardous and may lead to premature or catastrophic failures. Investigation of the affects of sound due to flow-excited acoustic resonance on the dynamic lift of tubes in an array is therefore of a significant importance.

Dynamic lift on the center tube in a square array for three different pitch ratios, $P/D = 3.37$, 2.18 and 1.58, is investigated. The dynamic lift force is measured before the onset of acoustic resonance and during flow-excited acoustic resonance. Before the onset of acoustic resonance the dynamic lift on the tubes in an array is due to the periodic flow exerting pressure forces on the tubes in the array. During resonance, the

dynamic lift is composed of an aerodynamic lift component, generated by the periodic flow though the tube array which is enhanced by the acoustic resonance and another component due to the acoustic pressure field generated by the acoustic standing wave.

Chapter 2 is an overview of the literature pertaining to the flow though tube arrays. This chapter also includes more fundamental survey of the flow over an isolated cylinder and extends to the more complex flow though tube arrays including the external effects on the interstitial flow though ducts containing both isolated and arrays of cylinders. Chapter 3 is a summary of the experimental setup used in the present study including the instrumentation used to measure aeroacoustic response and dynamic lift forces. The dynamic lift forces due to the acoustic mode and in the absence of flow are investigated in chapter 4 using both numerical and experimental methods. Chapter 5 introduces the aeroacoustic response of the three tube arrays. The mechanism of flow-excited acoustic resonance for the three spacing ratios and also the composition and magnitude of the dynamic lift during acoustic resonance is examined. Application of the present experimental results to industrial design applications is presented at the end of chapter 5. Conclusions are presented in chapter 6 summarizing the main findings of the present investigation.

Chapter 2

Literature Review

The following comprehensive review of the literature pertains to aspects of the current state of the knowledge of the topic. This review spans from fundamental studies of flow over an isolated cylinder to more complex cases of flow over tube arrays and influences on the flows such as flow-excited acoustic resonance.

2.1 Flow over a single cylinder

Flow over a single isolated cylinder is studied for both fundamental reasons and for contribution to practical applications. Practical applications motivating these studies include underwater tow lines used for sonar equipment, supports for offshore structures or risers and high tension electrical lines, all are sensitive to flow-induced excitation. The flow through heat exchanger tubes arrays and boilers is also sensitive to flow-induced vibration. The shells of heat exchangers and boilers contain natural acoustic modes, and are therefore sensitive also to flow-excited acoustic resonances. Systems such as these, and turbo machinery containing cascades of blades are complex. The complexity of the flow through these systems, and their susceptibility to acoustic resonances requires in depth understanding of the mechanism causing acoustic resonance. The flow over a single isolated cylinder is a "simplified" case used often to investigate the mechanism of flow-excited acoustic resonances, and therefore is of a fundamental interest in aeroacoustics research.

2.1.1 Strouhal number for a single cylinder

In 1878, Strouhal found the Aeolian tones generated by a wire in the wind to be proportional to the wind speed divided by the wire thickness. Strouhal developed a non-dimensional equation relating the flow velocity to the vortex shedding frequency which produces these tones. The Strouhal number (St), is defined as the vortex shedding frequency (f_v), multiplied by the cylinder diameter (D) and divided by flow velocity (U), shown in equation 2.1.

$$St_D = \frac{f_v D}{U} \tag{2.1}$$

The inverse of the Strouhal number is referred to as the reduced flow velocity, shown in equation 2.2. The variables of equation 2.2 are defined the same as those of equation 2.1 except for the frequency. The frequency, f_a, is the acoustic mode or natural vibration frequency.

$$U_r = \frac{U}{f_a D} \tag{2.2}$$

The Reynolds number is a dimensionless group relating the viscous and inertial effects. Notably, Lienhard (1966) and Marris (1964) compiled a complete description of the flow regimes exhibited by a single cylinder in cross-flow for a complete range of Reynolds numbers. Their findings are summarized as follows, and shown schematically in figure 2.1.

1. For $Re_D < 5$, the flow is laminar and unseparated. This symmetric flow is referred to as creeping flow.

2. For 5 *to* $15 < Re_D < 40$ two symmetric rotational zones form downstream of the cylinder, referred to as *Föppl* vortices.

3. For $40 < Re_D < 150$, the vortices become unstable and the first laminar periodic vortex shedding is observed which produces periodic forces on the cylinder. For Reynolds numbers greater than 90, the periodicity is governed by vortex shedding.

4. For $150 < Re_D < 300$, laminar vortex shedding develops into fully turbulent vortex shedding. Both the free shear layer and the vortices become turbulent. At $Re_D = 300$, the flow periodicity is mostly dissipated at 48 diameters downstream. The wake is fully turbulent above $Re_D = 300$.

5. At around $Re_D = 3 \times 10^5$, the laminar boundary layer on the cylinder surface has undergone transition to turbulent and a narrower wake is formed but without organized vortex structures.

6. At $Re_D = 3.5 \times 10^6$ the wake shows a turbulent vortex street again. The wake is thinner and the boundary layer is turbulent.

It is evident there will be variation in Strouhal number with the Reynolds number from the previous discussion. Lienhard (1966) effectively maps this relationship with compiled data, available in the literature at that time. In the sub-critical flow regime, the Strouhal number is approximately 0.2 as shown in figure 2.2.

2.1.2 Mean forces on a cylinder in cross-flow

Mean, non-zero drag force, for a single cylinder, occurs parallel to the flow direction. The mean drag force is composed of both frictional and pressure forces. For low Reynolds numbers, the frictional or *viscous* forces are dominant. At increased Reynolds numbers, the pressure drag is dominant due to induced negative pressure in the wake region on the downstream side of the cylinder, and high stagnation pressure

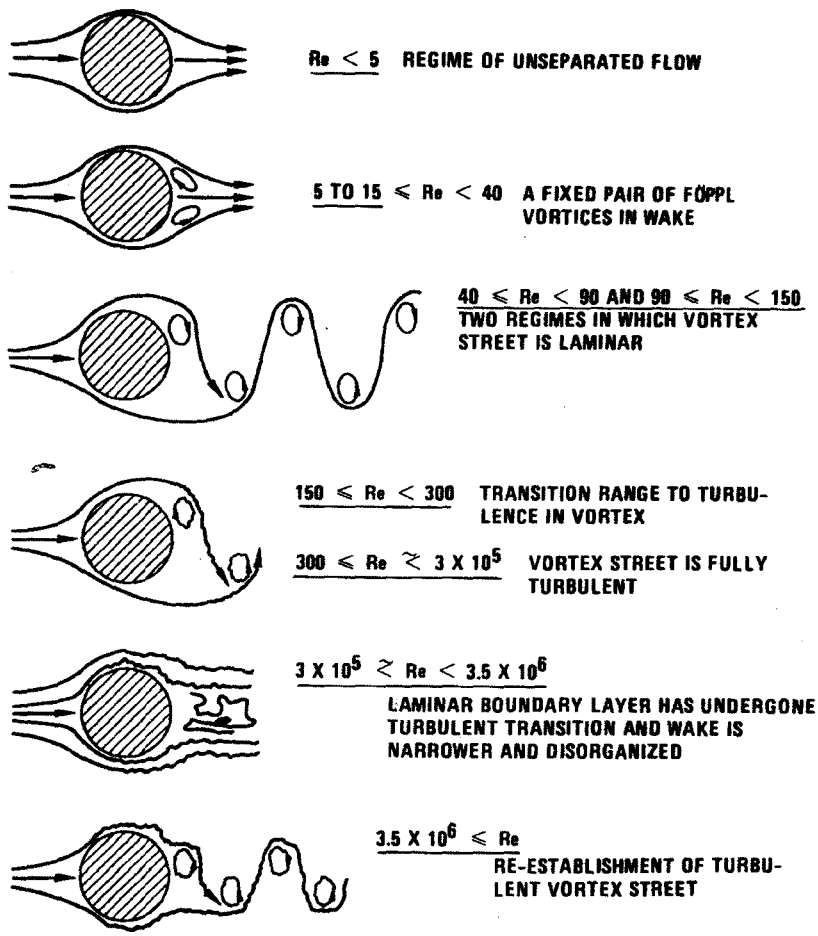

Figure 2.1: Flow regimes of a circular cylinder in cross-flow, Lienhard (1966). Digitized from Blevins (1990).

on the front surface caused by the deceleration of the inertial flow. The mean drag coefficient is defined in dimensionless form by equation 2.3:

$$C_D = \frac{F_D}{1/2\rho DU^2} \tag{2.3}$$

Where:

F_D is the mean drag force

ρ is the density of the fluid

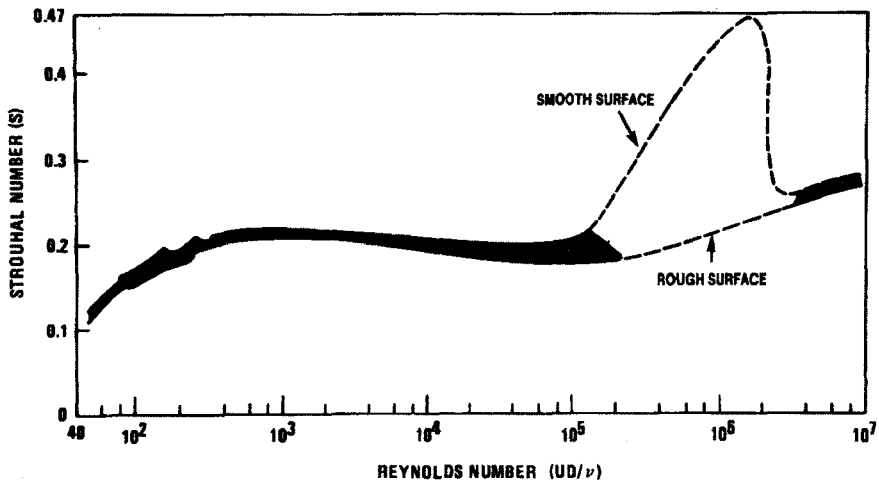

Figure 2.2: Strouhal number dependence on Reynolds number for a single cylinder in cross-flow, Lienhard (1966). Digitized from Blevins (1990).

D is the cylinder diameter

U is the mean stream flow velocity

In the lift direction, the mean force is zero. The time averaged flow is symmetric about the axis parallel to the mean flow direction, which causes a zero net transverse component.

2.1.3 Fluctuating lift forces exerted on the cylinder

At Reynolds numbers greater than 40, periodic vortex shedding occurs. This causes periodic forces on the cylinder. In the stream-wise direction, the drag force is composed of mean and fluctuating components In the cross-stream direction, normal to the cylinder axis and flow direction, only a periodic force component is observed. The frequency of the periodic forces corresponds with the vortex shedding frequency in the lift direction, and twice this value for the periodic forces in the stream-wise direction due to vortices shed alternately from either side of the cylinder.

Periodic lift forces are the dominant quantity of the dynamic forces for a single cylinder. For this reason, they are a major topic in the literature. Gerrard (1961) shows that in the sub-critical flow regime, the fluctuating lift coefficients are typically an order of magnitude larger than fluctuating drag coefficients. Etkin et al. (1957) shows that aerodynamic sound radiated by a single cylinder is a dominant sound source at the fundamental frequency of vortex shedding and is in a direction perpendicular to the mean flow field (in the lift direction). A second frequency twice that of the vortex shedding frequency is dominant in the direction parallel to the mean flow direction and associated with the dynamic drag but has a lesser magnitude than that in the lift direction. Dynamic lift forces motivate much of the previous literature, to determine the magnitude of the forces for prevention of damage due to fatigue failures, and also to explore novel ways to reduce these forces by disrupting the organized vortex shedding. Figure 2.3 shows the local pressure coefficients plotted along the surface of the cylinder over a cycle of vortex shedding.

Dynamic lift forces are expressed in terms of root-mean-squared or maximum amplitude. Similar to the equation for mean drag, an equation for the dynamic lift force is given by Bishop (1964) as:

$$C_{Lrms} = \frac{F_{Lrms}}{\frac{1}{2}\rho D l U^2} \tag{2.4}$$

Where:

F_{Lrms} is the root mean square (rms) amplitude of force

ρ is the fluid density

D is the cylinder diameter

U is the mean stream flow velocity

l is the cylinder length

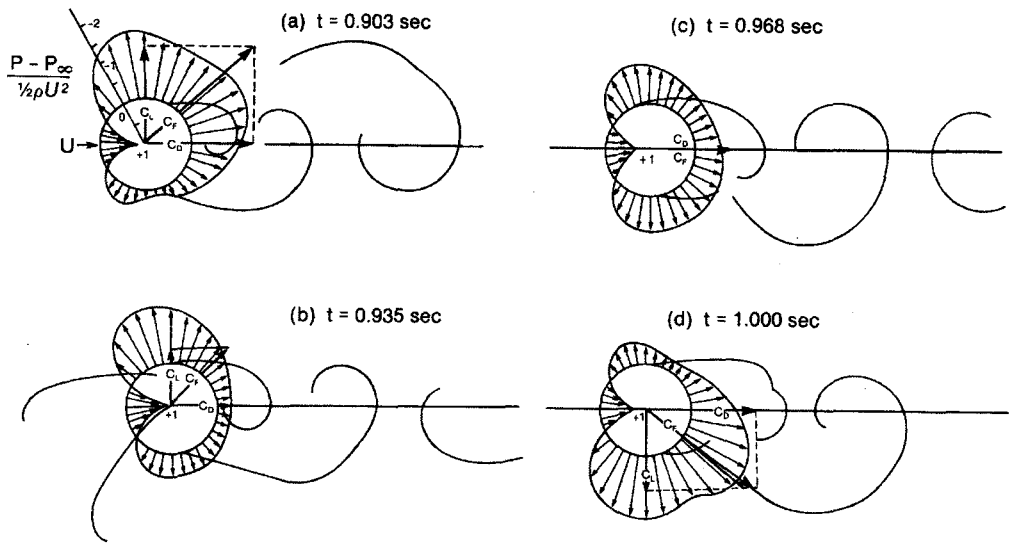

Figure 2.3: Local pressure coefficient distribution for a cycle of vortex shedding, Bishop (1964). Digitized from Blevins (1990).

There are several methods discussed in the literature for determining fluctuating lift forces. These methods are classified as either direct or indirect. Norberg (2003) reviews the available measurement techniques. Direct methods use a force sensing element such as a piezoelectric load cell or strain gauge arrangement attached to a cantilever beam or a simply supported beam which behaves as an active measurement element on the cylinder span. In some cases, the entire span of the cylinder is used as the active region. Indirect measurements differ, they typically invoke the use of single pressure taps, or rings of pressure taps. The lift coefficients are determined from integration of the point measurements around the circumference of the cylinder. In some cases a *dummy* cylinder is manufactured with an active measurement region. The active length (l_c) is used instead of the total cylinder span l in equation 2.4. Figure 2.4 is a compilation of lift coefficient data by Norberg (2003). There is much scatter in the data, primarily due to three-dimensionality of the flow. This

demonstrates the importance of considering both the measurement technique, and three-dimensionality of the flow, when comparing with sectional measurements.

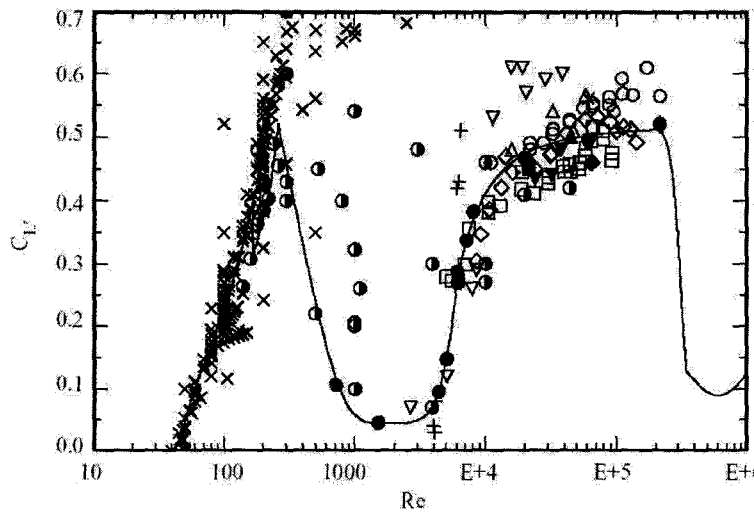

Figure 2.4: $C_{L'}$ for Reynolds numbers between 30 and 1×10^6, Norberg (2003).

2.2 Flow over pairs of cylinders

A natural extension to the study of the flow over a single cylinder is to the flow over pairs of equal diameter cylinders. Three main configurations are of interest, namely, tandem, side-by-side and staggered arrangements classified in the review by Zdravkovich (1977). The spacing ratio* for two cylinders is typically defined by the center to center distance divided by the cylinder diameter. This ratio is used for the defining of the proximity regions where the shear layers of either cylinder are known to interfere with each other. Data compiled by Zdravkovich (1985) maps the interaction regions shown in figure 2.5.

*Spacing ratios for tandem cylinders are defined using the longitudinal distance L divided by the cylinder diameter. Spacing ratios for side-by-side cylinders are defined using the transverse distance T divided by the cylinder diameter.

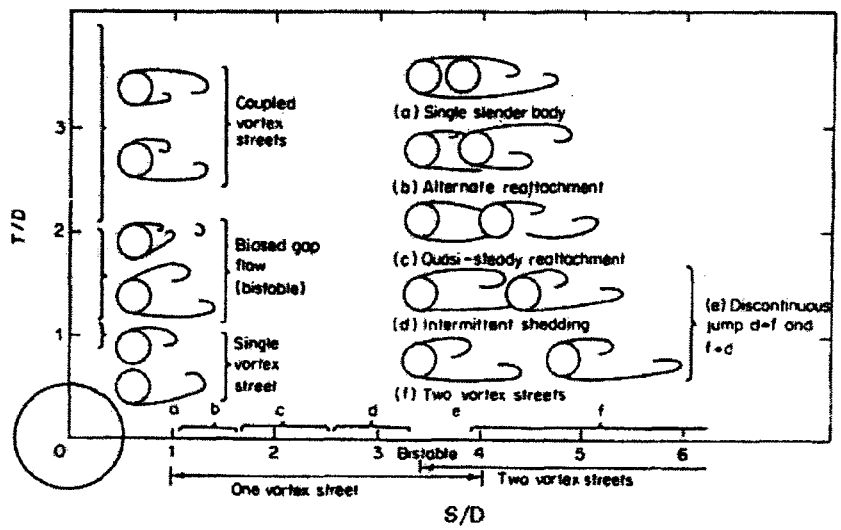

Figure 2.5: Proximity regions and corresponding flow regimes for the flow over tandem and side-by-side cylinders, (Zdravkovich 1985).

For tandem cylinders, the Reynolds number affects the position of the exact transition point between the defined regions. Zdravkovich (1985) classified the flow over tandem cylinders in terms of the spacing ratio (L/D), noting the dependence on Reynolds number. Spacing ratios in the range $1 < L/D < 1.2$ *to* 1.8, show wake behavior similar to a single slender bluff body. For 1.2 *to* $1.8 < L/D < 3.4$ *to* 3.8, the shear-layers detach from the upstream cylinder and reattach to the upstream surface of the downstream cylinder. A vortex street forms in the wake of the downstream cylinder. For $L/D > 3.4$ *to* 3.8, vortex shedding occurs in the gap formed between the two cylinders *and* behind the downstream cylinder.

The Strouhal number for tandem cylinders varies with both spacing ratio and the Reynolds number. Igarashi (1981) mapped the Strouhal numbers of tandem cylinders for two different Reynolds numbers. Small spacing ratios, with L/D near 1, are known to behave as a single body and exhibit a single Strouhal number near 0.27. As the spacing ratio increases, a strong dependence on Reynolds number is

observed for spacing ratios up to 2. Further increases in the spacing ratios diminishes the Reynolds number dependence.

The flow over side-by-side cylinders is discussed by Zdravkovich (1985) and Zdravkovich (1977). The observed flow regimes are classified. Three dominant flow regimes with distinctly different behavior exist. For the close spacing regime, where $1 < T/D < 1.1$ *to* 1.2, a single vortex street is formed. For the intermediate regime where $1.2 < T/D < 2$ *to* 2.2 one cylinder exhibits a narrow closed wake and the other a wide open wake. Between the two wakes, a jet, termed bistable (Kim and Durbin 1988) is directed toward the narrow wake, causing the wide open wake of the other cylinder. This jet can exist biased toward either the two cylinders for a few seconds, or in the order of minutes. The transition of the jet toward the other cylinder appears random, (Bearman and Wadcock 1973 and Kim and Durbin 1988). Kim and Durbin (1988) termed the close and intermediate proximity region as the *flip flop region* to describe the observed random movement of the biased jet toward either of the two cylinders. For large spacing ratios, each cylinder wake appears similar, however, they exist either in-phase or out of phase with each other (Williamson 1985).

Strouhal numbers vary with the spacing ratio for side-by-side cylinders due to the various flow regimes observed in the cylinder wakes. The results are summarized schematically in figure 2.6. This figure represents an average trend drawn from the available data, notably those compiled by Sumner et al. (1999). For small spacing ratios, only one Strouhal number, nearly half the value of a single isolated cylinder is present. In the intermediate range, the narrow wake produces a higher Strouhal number than the wide open wake, and at nearly twice the value. Further increases to the spacing ratio causes both Strouhal numbers to approach that of a single isolated circular cylinder, where the Strouhal number is approximately 0.2.

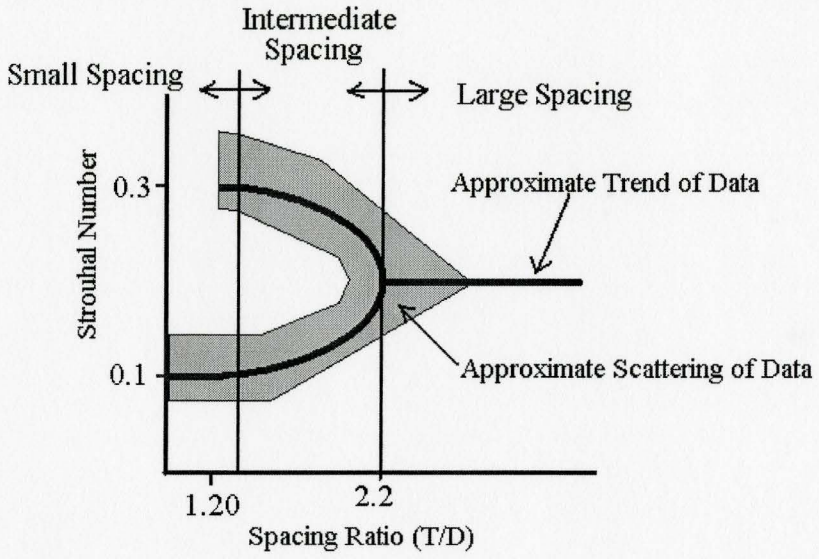

Figure 2.6: Strouhal number versus spacing ratio for side-by-side cylinders showing the approximate trend of the data, and scatter, Hanson et al. (2006).

2.3 Flow-excited acoustic resonance

Flow over a single cylinder produces a dipole like sound source (Curle 1955). The sound field is dominant in the direction transverse to the mean flow direction and cylinder axis (Etkin et al. 1957). Classical, Strouhal-excited acoustic resonances occur when the natural vortex frequency approaches the frequency of a transverse mode of the duct. Figure 2.7 shows this process schematically. The duct drawn in figure 2.7 is designed such that the natural frequency of vortex shedding coincides with the transverse acoustic mode of the duct as shown in figure 2.7(a) and (b). Figure 2.7(c) shows a typical frequency response during the locked-in resonance conditions. The natural frequency of vortex shedding is shifted up to the natural acoustic mode frequency. Further increases in the velocity causes the synchronization between the acoustic mode and vortex shedding frequency to weaken and deteriorate. After this, vortex shedding continues to occur at the natural Strouhal number. The acoustic

pressure, shown in figure 2.7(d), exhibits a large increase in pressure associated with the acoustic resonance phenomena. Parker and Stoneman (1989) and Welsh et al. (1990) have published excellent reviews on this topic.

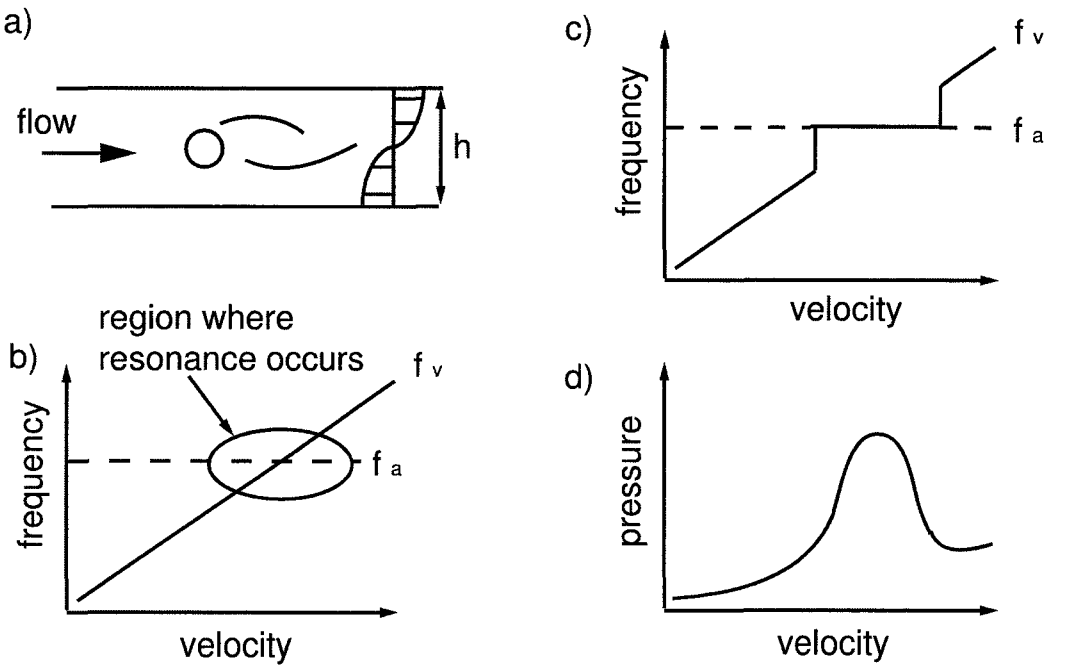

Figure 2.7: Schematic of the lock-in phenomena showing the typical aeroacoustic response during flow-excited acoustic resonance for a single isolated cylinder.

Blevins and Bressler (1993) investigated the flow-excited acoustic resonance of a single cylinder and plotted the frequency and acoustic sound pressure levels against the reduced velocity. This shows,in figure 2.8, digitized from Blevins and Bressler (1993), the lock-in phenomena and associated increase of the sound pressure level at the frequency of the acoustic mode. Mohany and Ziada (2005) explains, from the theory of aerodynamic sound of Lighthill (1952), that the sound generated by a vortex is proportional to the length scale of the vortex, the dynamic head and Mach number. The theoretical analysis by Blake (1986) shows that the acoustic sound pressure can be normalized by the dynamic head multiplied by the Mach number, $\rho U^3/c$. This is found to greatly collapse the acoustic sound pressure level data for single cylinders

in flow-excited acoustic resonance with different tube diameters, (Mohany and Ziada 2005).

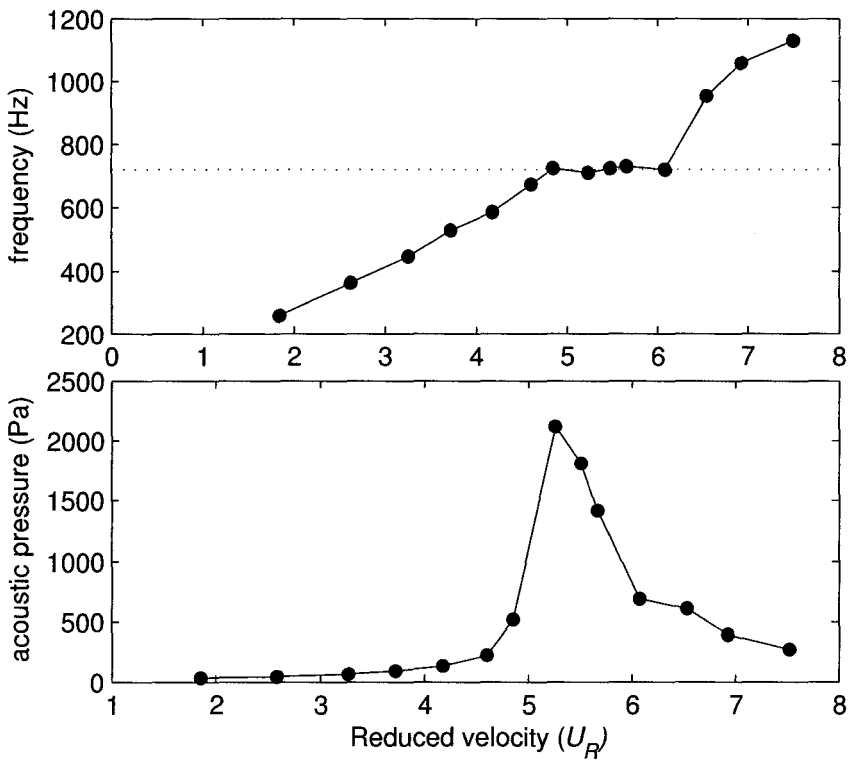

Figure 2.8: Aeroacoustic response of a single tube in cross-flow. Figure (a) is the frequency of vortex shedding versus reduced velocity. Figure (b) is the acoustic pressure level at the frequency of vortex shedding versus the reduced velocity, (Blevins and Bressler 1993).

Acoustic resonance effects on characteristics of the flow over tandem cylinders is well understood from recent investigations. In their study of the effects of applied sound on vortex shedding of tandem cylinders, Hall et al. (2003) note that the lock-in region is much broader than of the single cylinder. Mohany and Ziada (2005) focuses on flow-excited acoustic resonance of tandem and single cylinders. For the flow-excited acoustic resonance of tandem cylinders, at the same acoustic mode, their results shows that acoustic resonance occurs over two different velocity ranges. Co-

incidence resonance, or classical Strouhal excited resonance, is excited by a natural vortex shedding, present in the off resonance conditions. Before the onset of classical resonance, a pre-coincidence range exists for the intermediate and small spacing ratios. In this range, the reduced velocity at resonance is lower than that for the classical coincidence type resonance. The excitation source is attributed to the shear layers in the gap between the cylinders. These shear layers detach from the upstream cylinder and reattach to the downstream cylinder, behaving much like the flow over cavity, which is also known to be sensitive to flow-excited acoustic resonance. An interesting finding of Mohany and Ziada (2005) is that for similar longitudinal spacing between tandem cylinders and inline tube arrays, the excitation of acoustic resonance occurs over a similar range of reduced velocities. This confirms that the excitation mechanism is indeed similar in these cases. The tandem cylinder results are overlaid with the resonance results for an inline tube array of Ziada and Oengören (1990) in figure 2.9, digitized from Mohany and Ziada (2007). The results shows the similar trends of the pre-coincidence resonance range and corresponding sound pressure levels of similar magnitude and behavior.

The aeroacoustic response of side-by-side cylinders is recently investigated by Hanson et al. (2006). The non-resonance Strouhal numbers are well defined in the literature, however, in the intermediate spacing ratios, acoustic resonance is not excited by the natural Strouhal numbers, but at an intermediate Strouhal number. For small and intermediate spacing ratios, the lock-in region is significantly broader than that of the single isolated cylinder. It occurs at a similar Strouhal number of the single cylinder, approximately 0.2. For the larger spacing ratios, acoustic resonance is excited over a narrower lock-in range than that for the intermediate spacing ratios, and the resonance is excited by the natural Strouhal number observed in the off resonance conditions.

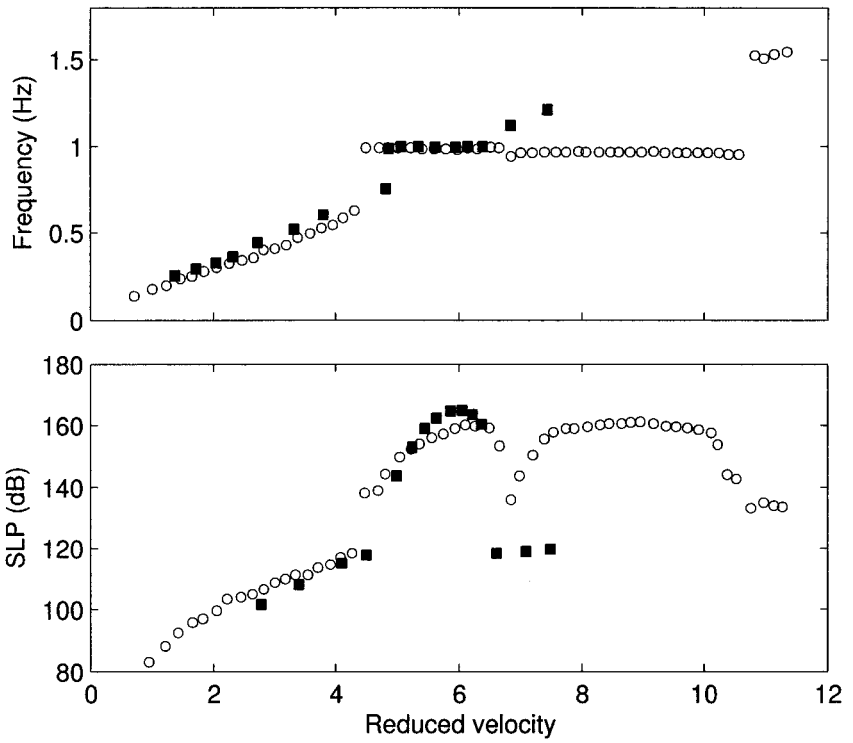

Figure 2.9: Comparison between the acoustic response of two tandem cylinders and that of the in-line tube array. ○, tandem cylinders with $L/D = 2.5$, (Mohany and Ziada 2005); ■, inline bundle with $X_L/X_T = 2.6/3.0$, (Ziada and Oengören 1990). Digitized from Mohany and Ziada (2007).

2.3.1 Effect of excitation on vortex shedding

Blevins (1985) excited, with loud speakers, the first transverse acoustic mode of the test section. Excellent agreement between the acoustic pressure along the test section height, and that calculated from theory is observed. Due to this agreement, it is expected the acoustic particle velocity prediction from theory is also valid. The calculated acoustic particle velocity is shown to be only a few percent of the mean velocity of the tests, but is comparable with the *rms*[†] turbulence characteristics of the

[†]*rms* is a shortform for the root mean squre or standard deviation of values from the mean.

vortices. Blevins (1985) shows that natural vortex shedding generated from the flow over a cylinder does not occur at discrete frequency, it can vary such that $f_v = f_o \pm 2\%$.

Blevins (1985) varies the position of the cylinder from the center of the test section towards the test section upper wall. Entrainment of the vortex shedding frequency to the excitation at the frequency of the first transverse acoustic mode of the test section is observed. The level of entrainment tends to increase as the cylinder is moved towards the test section center. When a cylinder is oscillated transversely to the flow field at a frequency close to the vortex shedding frequency, increased correlation and increased vortex strength occurs. The associated dynamic forces also increase; see for example Koopmann (1967) and Bishop (1964). This effect is similar to the effect of acoustic resonance, where the fluid is essentially oscillated over the cylinder. Carberry et al. (2001) investigate the dynamic lift forces for oscillating cylinders with Reynolds number of 2.3×10^3, and discussed the behavior of the lift forces and cylinder oscillations with the phase measurements between these quantities. As the excitation frequency (f_e) nears the natural vortex shedding frequency (f_o), large increases of the lift forces occur, associated with a phase shift reduction between the cylinder oscillation and dynamic lift forces at $f_e/f_o = 0.81$. Carberry et al. (2001) attribute the abrupt changes in lift coefficients with mode changes observed in the near wake structures and phase shift.

2.3.2 The effect of acoustic resonance on the dynamic lift force

The dipole sound source caused by vortex shedding can be expressed in terms of dynamic lift and drag coefficients on the cylinder (Phillips 1956). This aeroacoustic source excites acoustic resonance, wherein, as shown previously in figure 2.8, the acoustic pressure is amplified and dominant in the lift direction, due to the shape

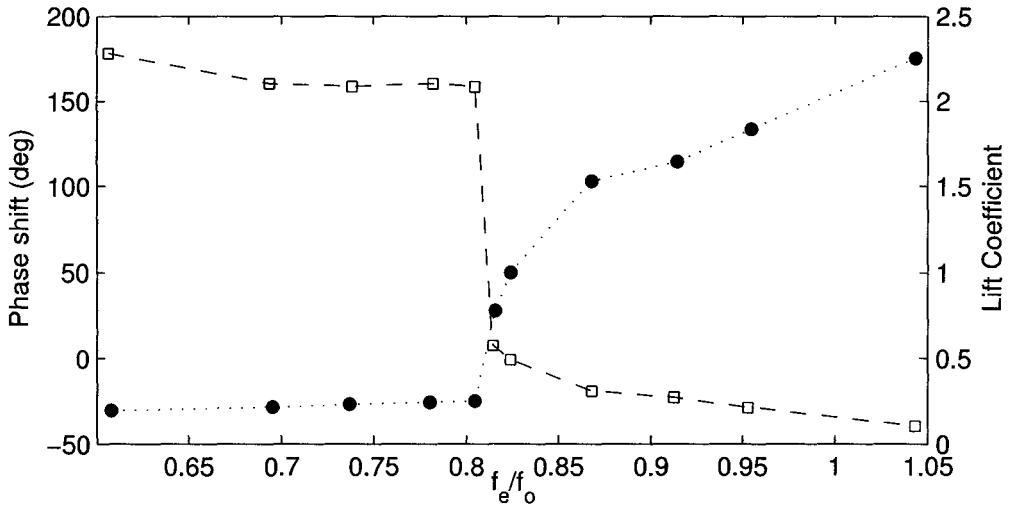

Figure 2.10: Lift coefficient, •, and phase, □, plotted against the ratio of the excitation frequency of the cylinder oscillations over the natural frequency of vortex shedding, f_e/f_o, Carberry et al. (2001).

of the transverse acoustic mode excited. The dynamic lift force is expected to increase with the sound pressure level during acoustic resonance, from the relationships determined by Phillips (1956). Direct measurements of the dynamic lift forces during flow-excited acoustic resonance of a single cylinder are investigated by Mohany and Ziada (2006). For a cylinder with a diameter of 15.8 mm, the lift coefficient varies between 0.24 and 0.28 during off-resonance conditions for a range of Reynolds numbers between 6×10^4 and 10^5. During acoustic resonance, the lift coefficient increases to 0.89, around four times higher than that measured during the off resonance conditions, as shown in figure 2.11.

The dynamic lift forces are decomposed into in-phase and out-of-phase components with respect to the acoustic pressure field measured at the top of the test section by Mohany and Ziada (2006). The out-of-phase component becomes negative during acoustic resonance and this component is therefore considered to be *negative acoustic damping*. Vortex shedding, in this case, behaves as an acoustic source, en-

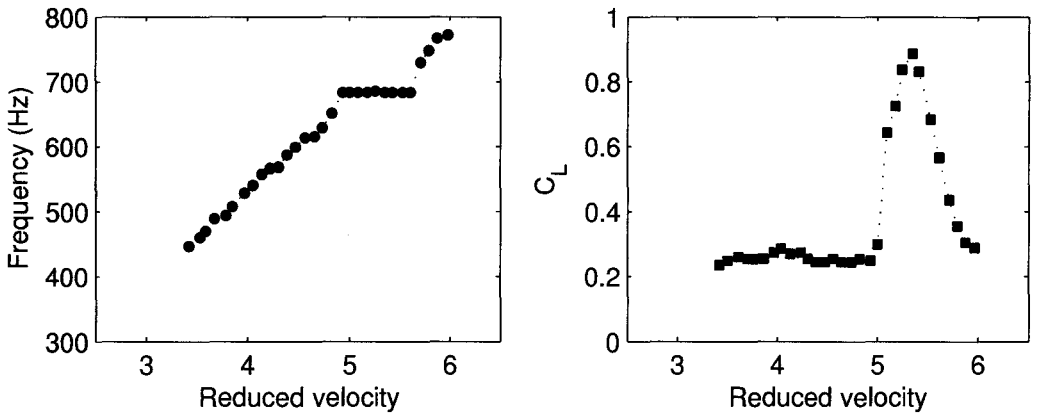

Figure 2.11: Frequency of vortex shedding (left) and the lift coefficient (right) as a function of reduced velocity for a single cylinder, (Mohany and Ziada 2006).

hancing the acoustic resonance, the opposite of typical (positive) damping effects. At off-resonance conditions the natural vortex shedding behaves as *positive acoustic damping* which acts to suppress the acoustic resonance.

In addition to single cylinders, the dynamic lift forces of tandem cylinders during the presence and absence of resonance are well understood (Mohany and Ziada 2006). These results, however, are much more complicated for tandem cylinders as there exists a pre-coincidence range of acoustic resonance as described in §2.3. For $L/D = 1.75$, the aeroacoustic response is plotted in figure 2.12(a) and (b). The corresponding dynamic lift force is plotted in figure 2.12(c). The dynamic lift forces on the downstream cylinder are much higher than those on the upstream cylinder. Furthermore, the dynamic lift is less in the pre-coincidence range than in the coincidence range. In the pre-coincidence range, the lift forces are out of phase for each cylinder. During classical type Strouhal excited acoustic resonance both cylinders show dynamic lift forces with a zero phase shift. This confirms that pre-coincidence and post coincidence resonance occurs due to different mechanisms.

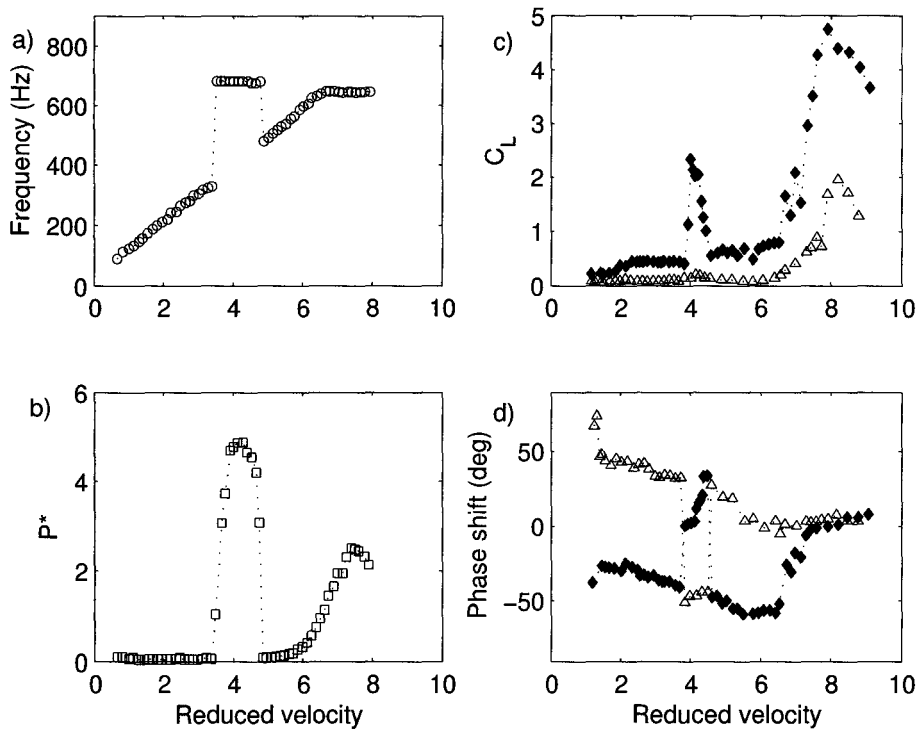

Figure 2.12: Aeroacoustic and dynamic lift response of tandem cylinder with $L/D = 1.75$. Figure (a) is the vortex shedding frequency as a function of the reduced velocity (U_R). Figure (b) shows the non-dimensional pressure at the frequency of vortex shedding. Figure (c) is the lift coefficient as a function of U_R. Figure (d) shows the phase shift between the microphone and dynamic lift. △, upstream cylinder; ♦, downstream cylinder. Digitized from Mohany and Ziada (2006).

2.4 Flow through tube arrays

The flow though tube bundles motivates the present investigation. Previous research develops a firm knowledge basis of the flow through more simplified and fundamental geometrical configurations. Applying the concepts and insights gained on unsteady flow phenomena from the previous research lays ground work for in-depth study into the behavior of the flow in tube bundles.

The excitation mechanisms for flow-induced vibration in tube arrays are: turbulent buffeting, vortex shedding, acoustic resonance and fluid elastic instability. Re-

views of these are summarized well by Weaver (1993), Weaver and FitzPatrick (1988) and Paidoussis (1983). The idealized response of a cylinder in a tube array subjected to a cross-flow is shown in figure 2.13. This demonstrates the effects and consequences of these excitation mechanisms on the vibration amplitude of a tube in an array.

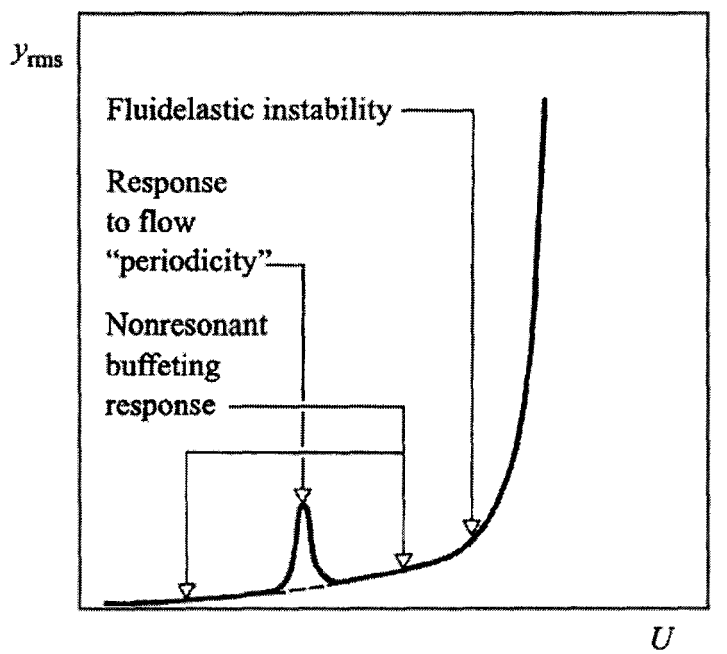

Figure 2.13: Idealized response of a cylinder in an array subject to cross-flow, Paidoussis (2006).

Several typical tube bundle arrangements are classified in a review by Weaver (1993), and shown schematically in figure 2.14. The past few decades have led way to significant contributions to the global understanding of the flow through tube bundles, and to the excitation mechanisms that leads to destructive damage of the tubes and/or shells of heat exchangers and boilers. The excitation sources in tube arrays has had some debate in the literature. Weaver (1993) presents an excellent review covering the debate of vortex shedding as an excitation source, and the previous beliefs. Much of this debate is focused at a common goal; determining a reliable way to

predict when problematic situations such as flow-excited resonances, both structural and acoustic in nature, can occur. Understanding the sources of excitation, such as periodic structures in the flow, and predicting when the excitation frequency will near a mechanical or acoustic natural frequency of the systems is highly important to design.

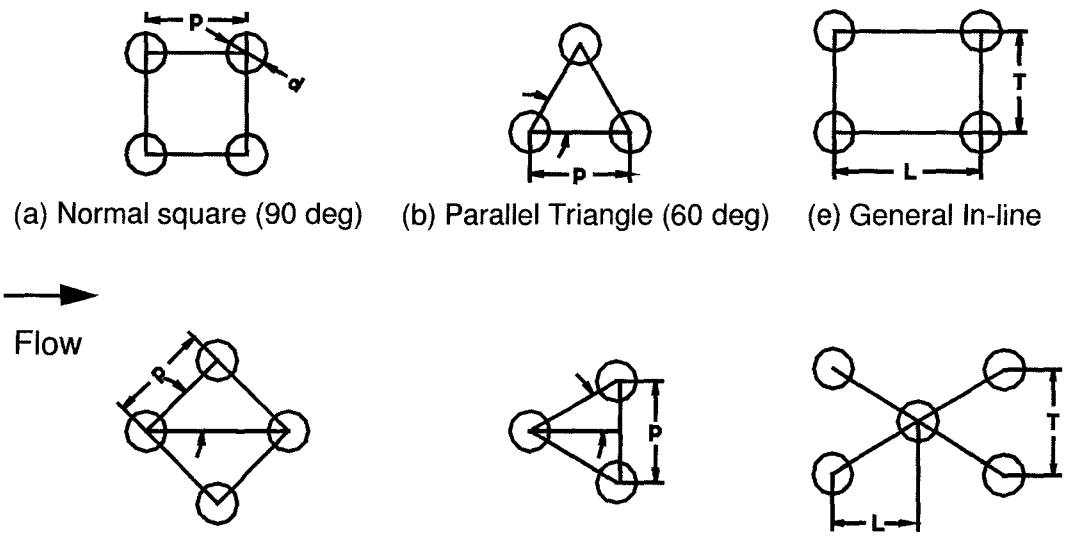

Figure 2.14: Array geometry definitions of standard array patterns, Weaver (1993).

Owen (1965) argues that vortex shedding cannot occur deep inside a tube bank as the flow would develop into a nearly homogenous turbulence. Since then, however, a number of papers have supported the idea of vortex shedding as the dominant source of periodic excitation. Fitzpatrick (1985) concludes that vortex shedding, turbulent buffeting and broadband turbulence contribute to sustaining and exciting resonance. Attempts to clarify some of the arguments addressed in the current literature are made for example by Weaver and FitzPatrick (1988). It is explained that broadband turbulence is always present in tube bundles. The tubes will indeed respond to this as demonstrated in figure 2.13. Broadband turbulence, however, is only likely to

contribute to fretting wear of tube supports, and this would take many years for considerable damage to accumulate. The broadband turbulence response should be considered in such applications as nuclear steam generators, designed for thirty plus years of service.

Strouhal periodicity or vortex shedding is distinctly different from turbulent buffeting in that it exist as a narrow band peak in the turbulence spectrum. Buffeting response is typically broadband (Weaver and Yeung 1984). Strouhal periodicity with frequencies in the vicinity of natural acoustic modes, or structural natural vibration frequencies can lead to flow-excited resonances. A foreknowledge of the associated Strouhal numbers in heat exchangers and boilers is necessary to avoid resonance conditions. Thus, much research has been directed in determining these quantities. The flow patterns in tube arrays have shown some major differences with varied spacings and geometries. One such reason that can be identified, described by Ziada (2006), is the existence of free flow lanes in the inline tube arrays compared to staggered arrays, shown in figure 2.15. Normal square arrays have open flow lanes, whereas the normal triangular and rotated square arrays, belonging to the staggered array category, have tubes that obstruct the flow lanes. The parallel triangular array, although belonging to the staggered array category, has open flow lanes, and exhibits some features similar to that of the square inline geometries as discussed by Ziada and Oengören (2000).

2.4.1 Flow periodicity through inline and square tube arrays

The characteristics of the flow through inline and square tube arrays are distinct from other tube arrays. They contain unobstructed flow lanes which allow the fluid to proceed, unobstructed. The open flow lanes allow the formation of a jet like structure.

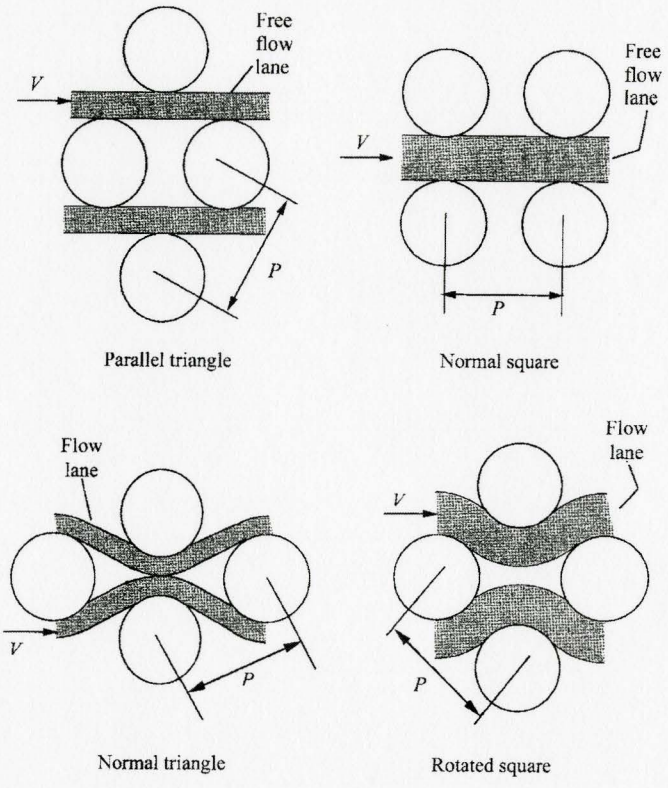

Figure 2.15: Standard layout patterns for tube bundles and corresponding flow lanes for $P/D = 1.4$, Ziada and Oengören (2000).

The complex flow through these flow lanes leads to vortex shedding Strouhal numbers which are different from those of staggered arrays.

It is of interest to discuss first the various structures, and flow patterns, present in the inline or square bundles. Small, intermediate and large spacing ratios exhibit different vortex shedding behavior, and flow characteristics in the interior of each bundle. Intermediate and large spacing tube arrays typically show a single Strouhal number, with a higher harmonic present in the air tests. For small inline bundles, when X_L and X_T are less than 1.5, vortex shedding occurs only in the upstream rows, the flow further downstream becomes fully turbulent. Oengören and Ziada (1992a) found three dominant Strouhal numbers for the small pitch ratio with $X_L/X_T =$

1.5/1.4. The Strouhal numbers identified are 0.92, 0.65 and 0.46, based on the gap flow velocity. The largest Strouhal number, 0.92, is associated with the symmetric jet instability, and the Strouhal number of 0.46 is suspected to be its sub harmonic. Flow visualizations by Ziada et al. (1989) shows that even small spacing ratio inline bundles exhibit vortex shedding at the interior tubes, although with little associated strength due to the close packing of the array and the development of highly turbulent flow. The flow structure through the bundle is dominated by a symmetric jet mode which suppresses an anti-symmetric mode. This produces symmetric vortices on both sides of the jet at non-resonant conditions. It is explained that the presence of the tubes, with the jet passing though the flow lanes is analogous to the jet-slot system shown to enhance a symmetric mode of vortex shedding (Rockwell 1983).

Intermediate spacing ratios show distinct differences from small spacing ratios. Oengören and Ziada (1992b) show that vortex shedding occurs over the entire depth of an intermediate inline tube array with $X_L/X_T = 1.75/2.25$. In the flow lanes, a symmetric mode of an unstable jet occurs with anti-symmetric vortex shedding in the wakes of tubes. This jet instability is the source of vortex shedding excitation. The intermediate range for inline tube bundles exists from around 1.75 to 2.7 (Ziada and Oengören 1993). Jet instability dominates the vortex shedding mode and exists up to longitudinal spacing ratios near 2.7. This mode also dominates the vortex shedding excitation in small spacing arrays studied by Ziada et al. (1989) for an array geometry with $X_L/X_T = 1.4/1.5$.

For the large spacing ratio inline arrays, investigated by Ziada and Oengören (1993), the flow structure is summarized as follows. Two distinct modes are present; a global jet mode and a local wake mode which appear to not occur simultaneously. The global jet mode occurs when the upstream turbulence is low, and is the same mode as in inline arrays with intermediate tube spacings. The local wake mode

caused by vortex shedding occurs in the front rows when exposed to highly turbulent upstream flow. Increasing the turbulence intensity trips the global jet mode, leading to a local wake mode. This change in mode is associated with a shift in the Strouhal number from 0.14 to 0.16. Vortex shedding at each tube is found to be independent of the adjacent tubes, and existed to a depth of approximately 5 tube rows. The wake instability mode is expected to be dominant, in practical applications, since the upstream turbulence intensity is typically high.

Charts of Strouhal numbers for square and inline tube arrays are available in the literature, two are shown in figure 2.16 by Weaver and Yeung (1984) and Ziada (2006). The Strouhal number plots developed by Weaver and Yeung (1984), contain both experimental data from various investigations, wherein references can be found from Weaver and Yeung (1984), along with empirical relationships developed by Zukauskas and Katinas (1980), given by equation 2.5, and by Owen (1965), given by equation 2.6. The Strouhal number is typically based on either the gap velocity (V_g) or the upstream velocity approaching the tubes (V_u). It is possible to convert between these values using equation 2.7. X_P is the spacing ratio of the tubes, S_u is the Strouhal number based on the upstream velocity, S_g is the Strouhal number based on the gap velocity, p is the distance between the center points of adjacent transverse tubes, and D is the cylinder diameter. One of the major drawbacks of the empirical relationships developed is that they fail to account for multiple Strouhal numbers observed in the flow through small spacing ratio square and inline arrays.

$$S_g = 0.2 + \exp\left[-\frac{X_p^{1.83}}{0.88}\right] \tag{2.5}$$

$$S_U = \frac{1}{2(X_P - 1)} \tag{2.6}$$

$$V_g = \frac{V_u}{(p - D)/p} \tag{2.7}$$

From the Strouhal number maps given in figure 2.16(a), the amount of scatter, and apparent disagreement is evident in the literature. For large spacings, good agreement is shown in all the results since only one Strouhal number exists. The maps by Murray et al. (1983), Fitz-Hugh (1973) and Weaver et al. (1987) show data collected by the authors, and data they also drew from the literature. Weaver et al. (1987) note that much effort has been taken to produce maps without resonance data included. However, the removal of the resonance data has not eliminated this confusion as found by Murray et al. (1983). The scatter can be attributed to other factors as well, including the Reynolds number, measurement location and the number of tube rows for example. For square arrays with small spacing ratios, the Strouhal numbers are inconsistent throughout the literature. Grotz and Arnold (1956) give $S_u = 1.02$, whereas Weaver et al. (1987) give the lowest Strouhal number as 1.44. In fact, Weaver et al. (1987) give three Strouhal numbers for the small spacing ratio array, namely 1.44, 1.72 *and* 2.04. The intermediate value of 1.72 observed by Weaver et al. (1987) only exists over a small range of Reynolds numbers between 420 and 590, based on the upstream flow velocity. The other two values were found to exist in their study for a range of Reynolds numbers between 760 and 1130. The Strouhal number observed by Grotz and Arnold (1956) is exactly half of the highest result determined by Weaver et al. (1987), indicating that it may indeed be a subharmonic. Chen (1968) gives $S_u = 0.87$ in his map for the same spacing ratios of Weaver et al. (1987), but drew his values from higher Reynolds numbers in the range of 0.5 to 2×10^4. The maps by Fitz-Hugh (1973) predicts $S_u = 0.93$ where Zukauskas and Katinas (1980) predicts $S_u = 0.88$. It is clear that Strouhal numbers for inline and square tube arrays are highly dependant on the testing conditions.

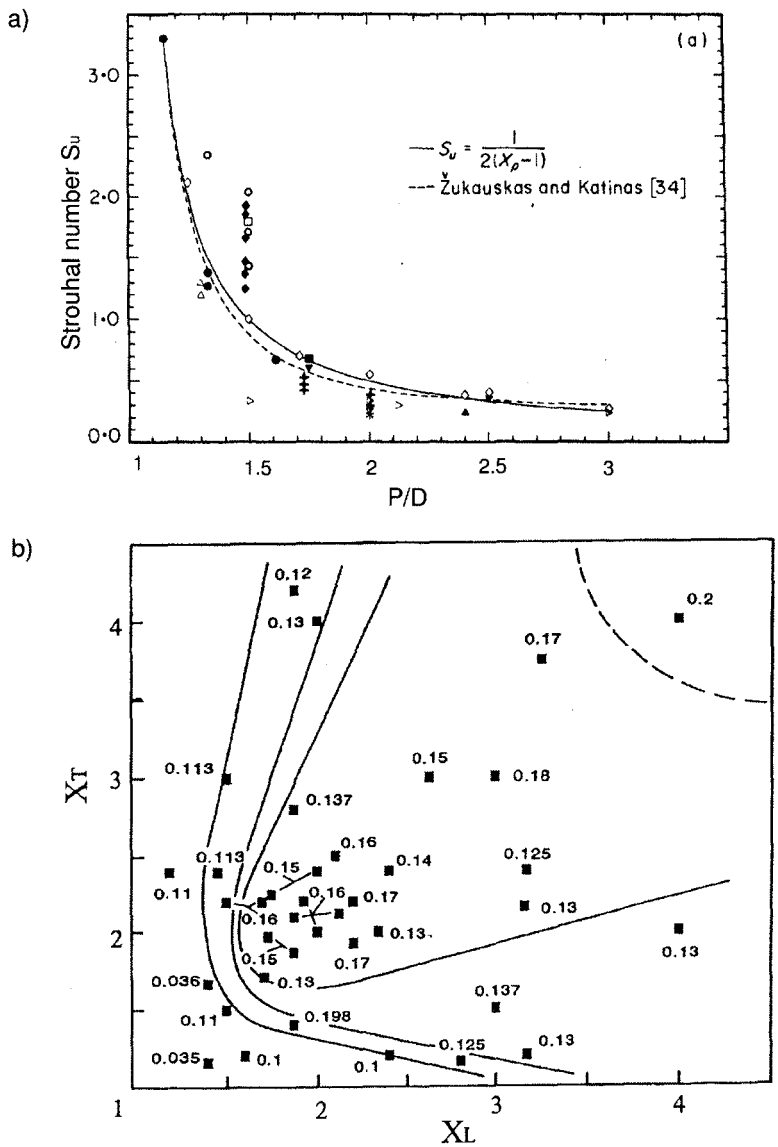

Figure 2.16: Strouhal number charts for square and inline tube arrays. (a) Compilation by Weaver et al. (1987), (St_u). (b) From Ziada (2006), (St_g).

2.4.2 Flow-excited acoustic resonance of tube bundles

Of particular interest to the present work is the research of Ziada et al. (1989), Oengören and Ziada (1992b), Ziada and Oengören (1993) and Oengoren and Ziada (1998). A major finding in these works is the fundamental differences in the mechanisms of acoustic resonance between inline and staggered tube arrays. Furthermore, the various spacing ratios of the inline arrays, small, intermediate and large, shows distinct characteristics during acoustic resonance. In the infancy of research on the acoustic resonance in tube bundle arrays, it was believed that vortex shedding is the primary source of excitation. See for example the works of Grotz and Arnold (1956) and Chen (1968). Later it was disputed, based on observed acoustic resonances not necessarily occurring at flow velocities predicted by Strouhal excitation, that the former belief is not necessarily valid. These arguments can be identified in the literature by Baylac et al. (1973), Fitzpatrick and Donaldson (1977), Rae and Murray (1987), Ziada et al. (1989) and Oengören and Ziada (1992b).

Oengören and Ziada (1992b) investigated the aeroacoustic response of an intermediate inline and staggered tube arrays. Figure 2.17 is a plot of the response of a staggered array with $X_L/X_T = 2.7/1.6$, along with two inline bundles with $X_L/X_T = 2.6/3$ and $X_L/X_T = 2.1/2.5$. For the two intermediate inline tube arrays, a common characteristic of the aeroacoustic response is the pre-coincidence resonance. The pre-coincidence resonance is an acoustic resonance that occurs before coincidence of the natural Strouhal number an acoustic mode of the test section. Acoustic resonance, in these arrays, occurs only before coincidence with the first transverse acoustic mode. Although another resonance range is shown, it is not related to the first mode acoustic resonance, and is at a higher mode frequency. This response is inherently different from the response observed for a single isolated cylinder indicating that the excitation mechanism is essentially different than flow-excited acoustic resonance

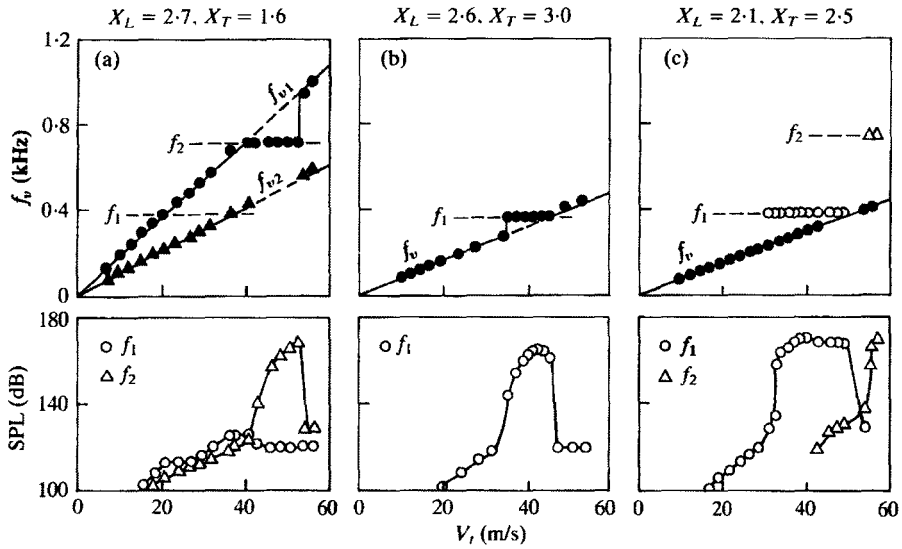

Figure 2.17: Frequency of vortex shedding, and sound pressure level at resonance frequencies, as functions of the gap flow velocity. (a) Staggered array (Ziada et al. 1989); (b) and (c) in-line array (Ziada and Oengören 1990). Source, Oengören and Ziada (1992b).

excited by vortex shedding indigenous to the unexcited flow. Oengören and Ziada (1992b) show detailed flow visualizations that expose changes in the flow patterns when acoustic resonance occurs. Before acoustic resonance, a symmetric jet instability mode is observed in the flow lanes as shown in figure 2.18. Along the tube rows, the cylinders shed vortices out of phase. Symmetry occurs along the centerline of the flow lanes as the tubes on either side of the jet exhibit out of phase vortex shedding. During resonance, the symmetric jet mode is suppressed, and an anti-symmetric shear layer mode becomes dominant. This is associated with in-phase vortex shedding along both the columns and the rows of tubes. Figure 2.18 shows this change in mode and is accompanied by a sketch to clarify the structures observed. It is suggested that acoustic resonance in the intermediate spacing tube bundles is excited by unstable shear layers formed in the gap between tubes in one column.

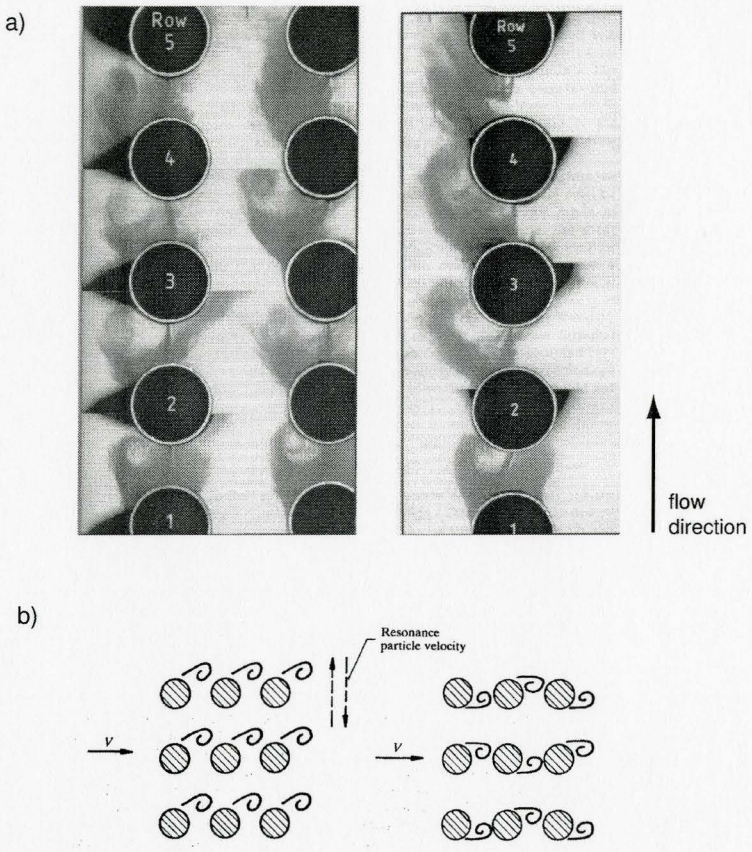

Figure 2.18: Flow visualization, shown in figure (a), of the flow structure during acoustic resonance. Figure (b) shows a schematic of flow structure during resonance (left) and before the onset of acoustic resonance (right) (Oengören and Ziada 1992b).

Large spacing inline tube arrays exhibit a classical Strouhal excited acoustic resonance. This response, shown in figure 2.19, is clearly different from that of the inline arrays shown in figure 2.17. Only the post-coincidence resonance range is excited for large spacing ratios, defining the major difference between this array and the intermediate tube arrays. Thus the mechanism of acoustic resonance is essentially different in the large spacing arrays, compared to intermediate and small spacing arrays. Contrary to these results, Ziada and Oengören (1993) found some similarity to intermediate spacing ratios when using a water tunnel. With low turbulence, two modes exist, the global jet mode and local wake mode, as discussed in §2.4.1. Pre-coincidence resonance can be excited with surface waves in the water tunnel if the

global wake mode persists. It is believed that this occurs due to switching between the jet and wake modes. The water tunnel tests, which excites free surface waves are believed to be distinct from the test done in air, and unlikely to occur in air since the jet mode occurs only in extremely low upstream turbulent conditions.

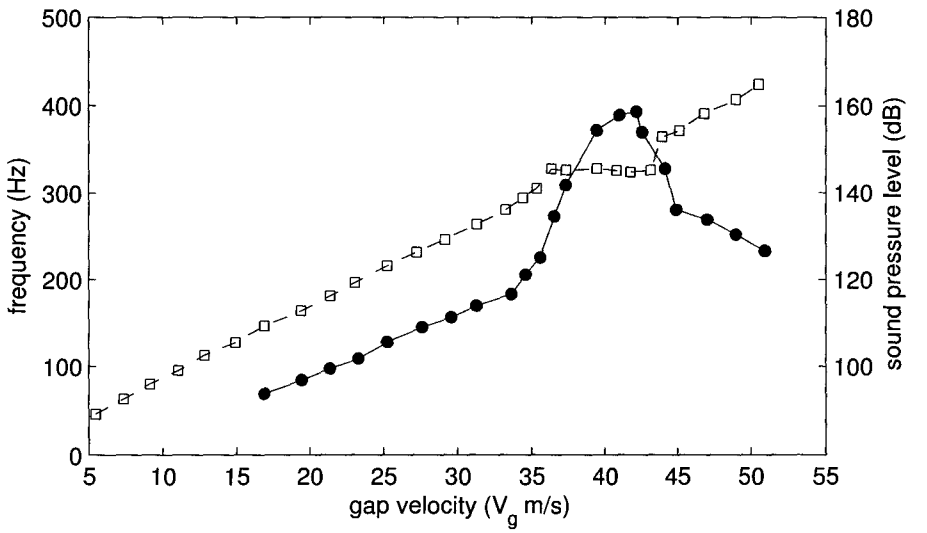

Figure 2.19: Aeroacoustic response of a large spacing inline array with $X_L/X_T = 3.23/3.75$. Digitized from Ziada and Oengören (1993).

Much of the past research is directed towards understanding and characterizing acoustic resonances in order to avoid destructive problems in the design phase. In some cases, acoustic resonance can occur due to changes in operating conditions, or from build up on the tube surfaces, not considered in the original design, requiring methods to disrupt the resonance. Blevins and Bressler (1987) discusses four methods to suppress acoustic resonance:

1. Installation of baffle plates to alter standing wave frequencies (D/h)
2. Selective tube removal
3. Addition of tuned Helmholtz resonators

4. Alteration of tube surfaces to suppress organized vortex shedding

Tube removal is considered an impractical solution. To appreciably reduce the sound pressure level of a noisy array, the removal of nearly sixteen percent of the tubes is required for tube arrays studied by Blevins and Bressler (1987). A Helmholtz resonator can suppress resonance; however, Blevins and Bressler (1987) note that the resonator would have to be of comparable size to the shell of the heat exchanger, also an impractical solution. Chen (1968) suggest acoustic baffles as the most practical and likely solution to acoustic resonance problems. It is generally accepted that acoustic baffles are the overall best way to suppress resonance, since they are typically effective if done properly and are the simplest way to retrofit a noisy heat exchanger. Baffle plates, however, can reduce the service life of a heat exchanger, due to increased fretting wear, when baffles are parallel to the tubes. Eisinger (1980) discusses the effects of solid baffle plates, but generally accepts that porous plates will reduce the negative effects of thermal distributions and baffle vibrations. It is clear that troubleshooting a noisy heat exchanger maybe difficult, or has negative impacts. Thus prediction and avoidance of acoustic resonances remains a primary goal.

2.4.3 Dynamic lift in tube arrays

Unsteady forces generated by the flow over the tubes in tube arrays is an excitation source that can lead to damage, noise and vibration (Paidoussis 1980). Several sources of excitation lead to increased amplitude in tube vibrations, identified in figure 2.13. Determining the strength of these unsteady fluid forces is important to the design and service life calculations of heat exchangers and boilers. Unsteady fluid forces on a tube in a square array with $P/D = 1.95$ are directly measured by Oengören and Ziada (1992). The dynamic lift and drag coefficients from this investigation are

plotted in figure 2.20. The Reynolds number causes considerable variation in the lift coefficients for the square array; it can either increase or decrease the lift coefficients, as evident in figure 2.20. Periodic lift forces are dominant over broadband turbulence in this array, typically at two to three times higher in magnitude. Furthermore it is shown that the dynamic lift tends to increase from the first row though the array. At sufficiently high Reynolds numbers the maximum dynamic lift is achieved at the fourth tube in the array presented. Several other studies exists in the literature, such as those by Chen and Jendrzejczyk (1987) and Axisa et al. (1988), however, the latter is directed at single row studies, and the former is in highly turbulent conditions. Recently, Inada et al. (2007) studied the fluid excitation forces acting on a rotated square tube with $P/D = 3.1$. The excitation forces are found to be three to ten times higher on the interior tubes than leading tubes.

The fluctuating lift and drag coefficients plotted in figure 2.20 are determined by integrating the normalized power spectral density. Previous literature on the dynamic lift response aimed to determine upper bounds of the NPSD[‡], and at creating empirical relationships for these bounds to be used for design purpose. Oengören and Ziada (1992) note that there exists a discrepancy in the literature due to how the data is determined and analyzed. Using models of the NSPD bounds may not accurately model the magnitude of the spectral peaks.

2.4.4 Speed of sound in a tube array

The presence of the tubes in the duct reduces the speed of sound in the duct. The amount of reduction is dependant on the fraction of the total volume occupied by the tubes. Determining the speed of sound in a tube bundle is necessary to properly

[‡]normalized power spectral density, $\phi = [F(V_g/d)/[(1/2)\rho V_g^2 Ld]^2]$

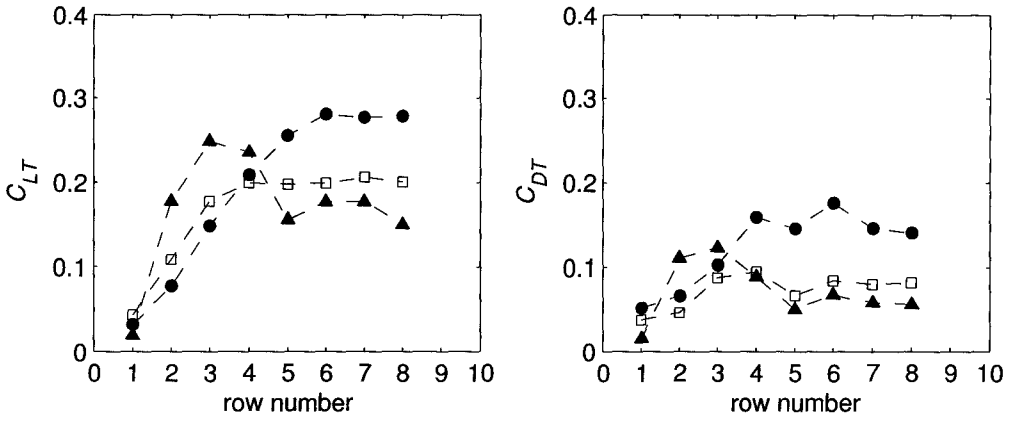

Figure 2.20: Fluctuating lift and drag coefficients as a function of row depth; •, $Re = 13,330$; □, $Re = 33,300$; ▲, $Re = 53,300$; (Oengören and Ziada 1992).

predict the frequency of acoustic modes. Equation 2.8 is used to determine the effective speed of sound in a heat exchanger by considering the effects of the solidity ratio, or volume fraction occupied by the tubes (Parker 1978).

$$\frac{c}{c_o} = \frac{1}{(1+\sigma)^{\frac{1}{2}}} \tag{2.8}$$

Where:

c is the speed of sound propagation perpendicular to the tube axis

c_o is the speed of sound without tubes present

σ is the solidity coefficient which is dependant on the array geometry

For the normal triangular and square arrays, σ is given as:

$$\sigma = 0.7853 \left(\frac{P}{D}\right)^2 \rightarrow \text{for square arrays} \tag{2.9}$$

$$\sigma = 0.9069 \left(\frac{P}{D}\right)^2 \rightarrow \text{for triangular arrays} \tag{2.10}$$

Another factor shown to cause variability in the effective speed of sound is the ratio between the depth and height of a test section. Ziada et al. (1989) found that this factor must be considered for depth to height ratios less than 2.5.

2.5 Discussion

The literature presented spans a wide range from basic fundamental investigations of the flow over an isolated cylinder to the more complex flow though tube arrays. Much of the current literature is directed toward the interstitial flow in tubes arrays for the purposes of predicting dynamic loading on the tubes and identifying sources of periodicity which can lead to flow-excited acoustic and structural resonance. For isolated and tandem cylinders, the dynamic lift increases abruptly during acoustic resonance. These results lead way to the question of how dynamic lift forces will respond to acoustic resonance in arrays of cylinders.

The square array is of interest since the mechanism leading to acoustic resonance is similar to the tandem cylinders investigated by Mohany and Ziada (2007), wherein a pre-coincidence and coincidence resonance range is observed. Similar to the tandem cylinders, large spacing ratio square arrays exhibit a coincidence resonance range, but the small and intermediate spacing ratios exhibit pre-coincidence resonance. For the square tube arrays, the dynamic lift forces in the absence of acoustic resonance have been determined, however, during acoustic resonance the dynamic lift forces are yet to be investigated. Increase in the total dynamic lift forces during acoustic resonance shown by Mohany and Ziada (2006) for tandem and single cylinders, underlines the necessity for this investigation, thus the purpose of the present investigation is to determine the behavior and characteristics of the dynamic lift response during acoustic resonance. The dynamic lift response in the pre-coincidence and coincidence

resonance ranges reported by Mohany and Ziada (2006), exhibits major differences for tandem cylinders and therefore it is expected that the dynamic lift response in square arrays may behave very differently for different spacing ratios. Both dynamic lift forces and aeroacoustic responses have been investigated over a large range of spacing ratios for the tandem cylinders creating a excellent database for comparison and extension to square arrays. Furthermore, the phase response between the sound field and the dynamic lift forces for tandem cylinders indicates that the dynamic lift in tube arrays may exhibit also a different phase shift response during the two resonance ranges.

The effect of the acoustic pressure field on the dynamic lift force during flow-excited acoustic resonance in square tube arrays is investigated in this study. It is shown that the lift coefficients on single and tandem cylinders is large compared with square arrays. For tandem cylinders, the lift coefficient on the downstream cylinder can be an order of magnitude higher than those in square tube arrays. For the single and tandem cylinders, the dynamic lift due to sound is negligible since the lift forces generated by the periodic flow are dominant during acoustic resonance. However, in square arrays this may not be true. The lift coefficients are lower due to the confinement of the tube wakes. It is therefore necessary to investigate the dynamic lift in the presence of the acoustic pressure distribution imposed on the surface of the cylinders during acoustic resonance.

Chapter 3

Experimental Setup

The following chapter describes in detail the experimental facilities and instrumentation used in the present investigation.

3.1 The Wind Tunnel

The wind tunnel is an open loop configuration, consisting of a 50 HP AC induction motor powering a centrifugal type blower. This setup draws air in though the test section inlet and exhausts into the main section of the tunnel. The motor is controlled by a Toshiba TOSVERT 3-phase industrial, variable frequency inverter, allowing fine increment adjustment of flow velocity and repeatability of a selected velocity. A schematic of the configuration is shown in figure 3.1. The main components identified are the parabolic inlet, test section, diffuser, flexible connections, centrifugal blower, 50 HP Motor and controller and the outlet side of the main tunnel.

3.2 The Main Test Section

The test section is a rectangular duct 810 mm in length by 254 mm in height and 76.2 mm in width. The tube bundle spacings and tube diameters are varied to achieve the desired spacing ratios. Birch plywood, 19 mm thick, is used to construct the top, bottom and sidewalls of the test section. The inlet of the test section is fitted with a smooth parabolic contraction to reduce pressure drop, prevent flow

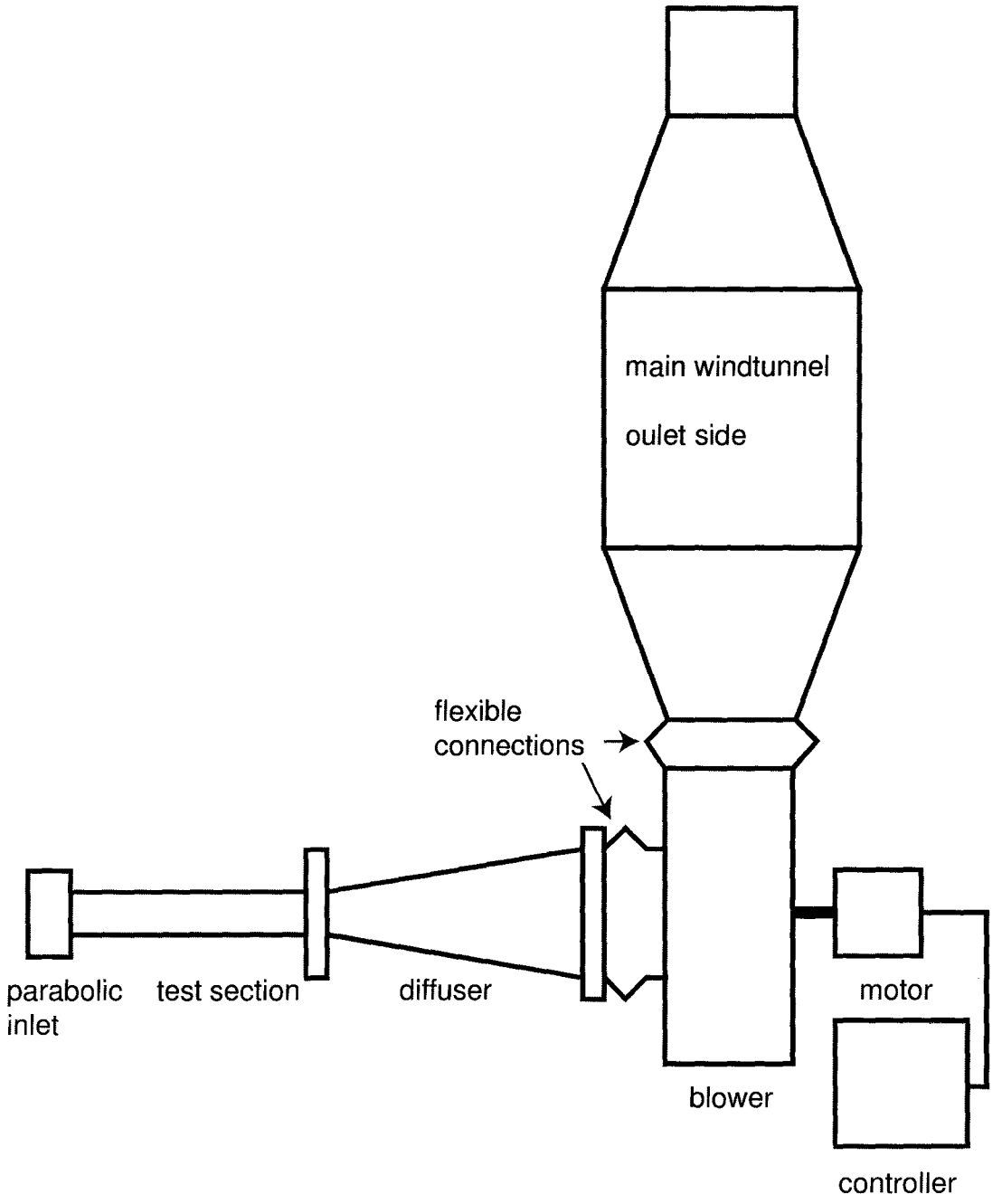

Figure 3.1: A schematic of the general layout of the windtunnel.

separation and create an approximately uniform upstream flow field. The parabolic contraction was designed by Macleod (1995), wherein further properties and velocity profile information can be found. At the exit of the test section a diffuser recovers the pressure losses that would be lost to a smaller exiting section and is also used for attachment to the blower inlet, designed by She (2000).

Mohany and Ziada (2006) designed the initial test section which was later modified for the purposes of the present research. The dimensions are chosen in such a way to ensure coincidence between the natural Strouhal periodicity and the first transverse acoustic mode for a variety of cylinder diameters between 9 and 26 mm. Although coincidence with a transverse acoustic mode is necessary, it is not necessarily sufficient to ensure flow-excited acoustic resonance. Other considerations, such as the Mach number, Reynolds number as well as the dynamic head are taken into account in the initial design. The test section design also accounts for blockage ratios, typically less than ten percent with aspect ratios approximately six for a single isolated cylinder. A schematic of the parabolic inlet, test section and diffuser is shown in figure 3.2.

3.3 The tube bundles

Only square tube arrays are investigated. Each of the three arrays fell into a different category of spacings, namely the small, intermediate and large spacings. A summary of the tube arrays, including the spacing, and tube diameter is given in table 3.1. The flow velocity in the test section, based on the gap velocity typically ranged from 10 m/s to 80 m/s in the large spacing array, and a maximum velocity of up to 65 m/s in the smaller spacing arrays, due to a higher pressure drop imposed by the smaller flow lanes of these smaller arrays. The Reynolds number is defined in equation 3.1, where V_g is the gap velocity, D is the cylinder diameter and υ is the

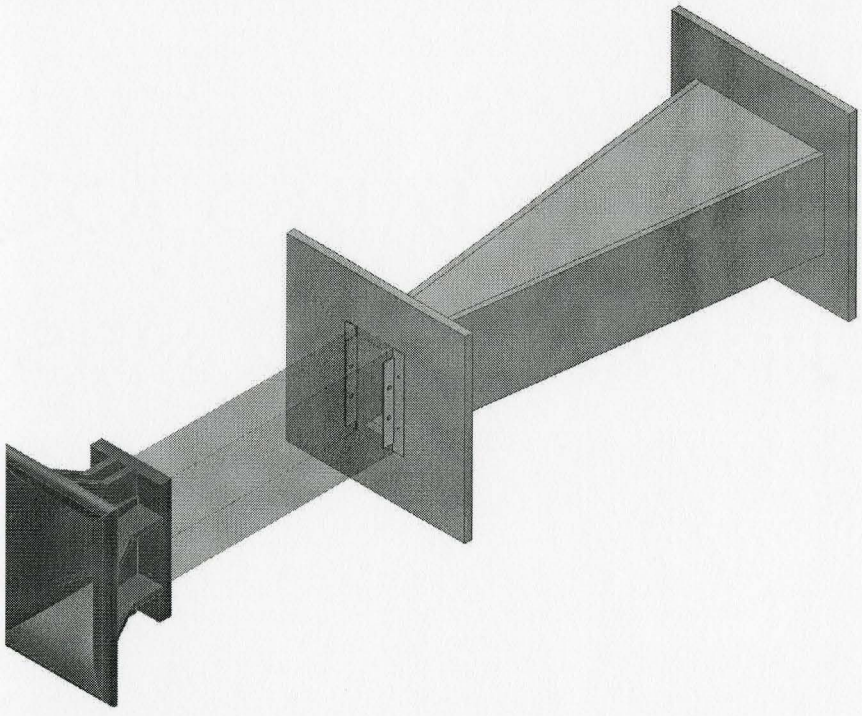

Figure 3.2: The test section showing the parabolic inlet and diffuser.

kinematic fluid viscosity. In the present experiments, the Reynolds number typically varied from 1×10^3 to 8×10^4.

Table 3.1: Summary of the three tube arrays investigated

Array	Class	Diameter	Spacing	# Rows	# Columns
$P/D = 3.37$	large	15.08 mm	50.8 mm	7	7
$P/D = 2.18$	intermediate	16.67 mm	36.34 mm	7	9
$P/D = 1.58$	small	15.08 mm	23.83 mm	7	11

$$Re = \frac{V_g D}{\upsilon} \tag{3.1}$$

A schematic of a tube array is shown in figure 3.3. Half tubes are not used along the wall, however, the top and bottom walls were positioned at the centerline of the flow lanes. The speakers are inlaid into the top and bottom wall and covered with perforated plates, as shown in figure 3.3, to maintain the test section inner dimensions

while allowing the speakers to excite the transverse acoustic mode. Eight Misco* 8 Watt speakers (DC3WP, 3" diameter cone) are used to excite the acoustic mode, four on the top, and four on the bottom as shown in figure 3.3 for the imposed sound testing. During the aeroacoustic test with flow, the top and bottom sections are replaced with solid section without holes for the speakers. For the instrumented cylinder, measuring the dynamic lift, an insert is used on the test section side walls to eliminate possible dynamic pressure effects in the area the tube passes though in the wall as shown in figure 3.4. The wall thickness of the insert is 1.6 mm, limiting the uncertainty in the cylinder effective length to 4%. The hole through which the cylinder passes through the insert is slightly oversized of the cylinder, creating a gap of 0.4 mm. The oversized hole is necessary to ensure the cylinder does not contact the walls of the test section, leading to transmission vibration from the test section to the load measurement rig. Seals cut from latex are used to prevent flow though the gap, shown in figure 3.4. The measurement rig is mounted to a heavy steel frame, isolated from the ground with vibration pads.

The speakers are wired in a parallel/series circuit wherein the top and bottom rows of speakers are connected in parallel, and the two parallel setups are wired in series, but with the polarity of the two sets of speakers reversed. This circuit design increases the effective resistance of the circuit over other schemes, therefore drawing less current to achieve the same total power output. Essentially, this circuit, given an input sinusoidal wave form, will output a sine wave to the top and bottom rows of speakers. The top and bottom speakers will produce acoustic waves with a phase shift of 180 degrees. Since the goal is to impose a sound field at the first transverse acoustic mode frequency, this is a necessary condition (see figure 3.6 for diagrams of the acoustic mode shapes).

*Misco is a registered trademark of the Misco Speaker Company

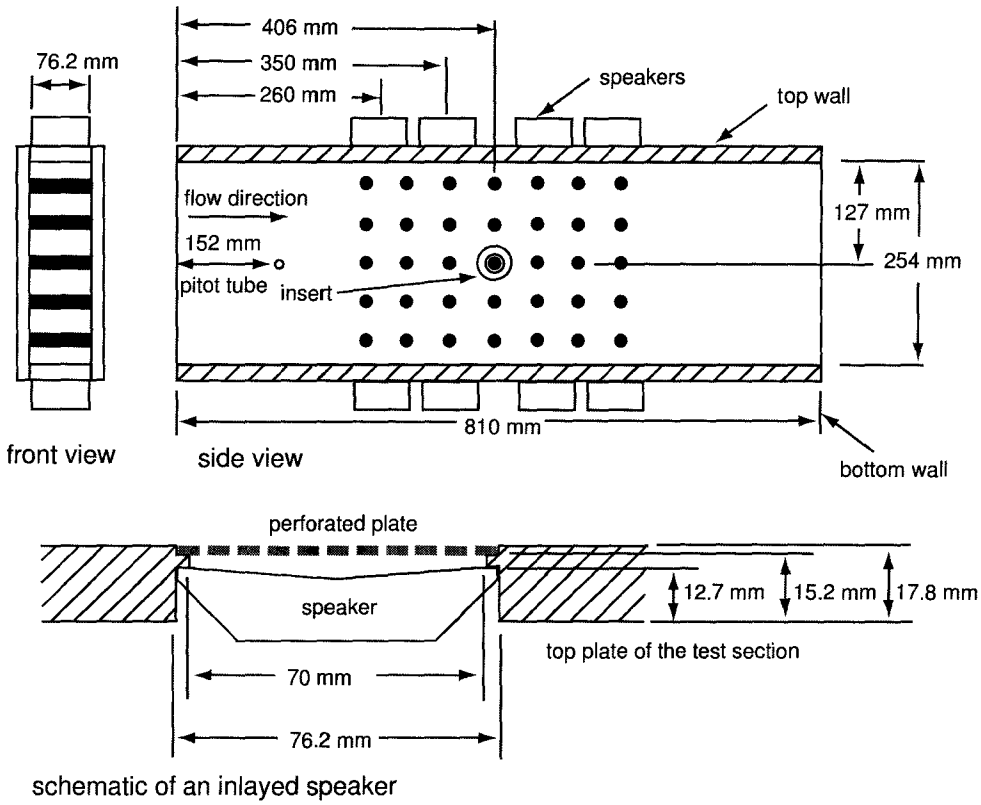

Figure 3.3: The general tube bundle layout showing the inlaid speakers, (P/D = 3.37).

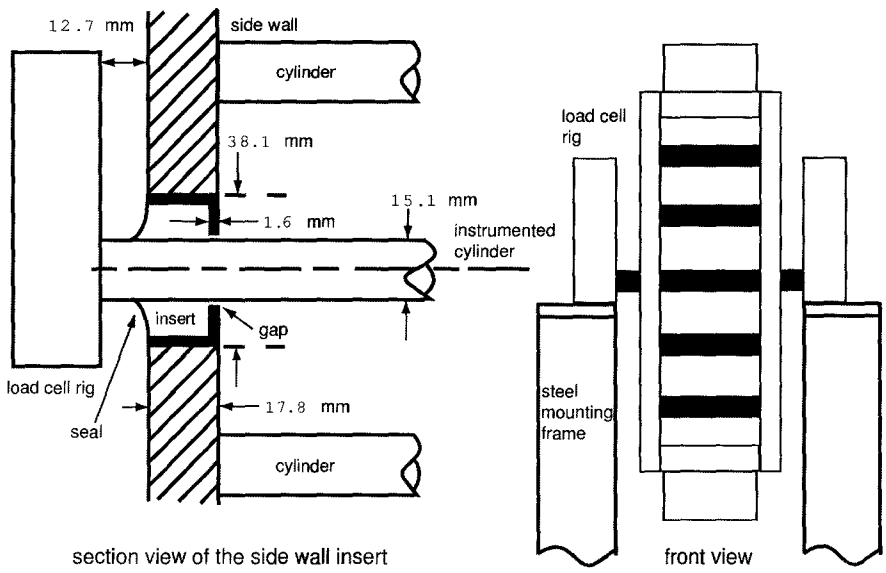

Figure 3.4: Schematic of the insert inlaid in the side wall, ($P/D = 3.37$).

3.3.1 Acoustic modes of the test section

The wave equation (equation 3.2), or as commonly referred to in the literature as the linear, lossless wave equation (Kinsler et al. 2000), is solved for the harmonic solution using assumed boundary conditions. For the transverse acoustic mode of a rectangular duct open at opposite ends, with the coordinate system defined in figure 3.5, the corresponding boundary conditions at the top and bottom walls are a zero particle velocity, or zero pressure gradient, given in equation 3.3. The boundary conditions at the open outlet and inlet, with zero pressure, are given in equation 3.4.

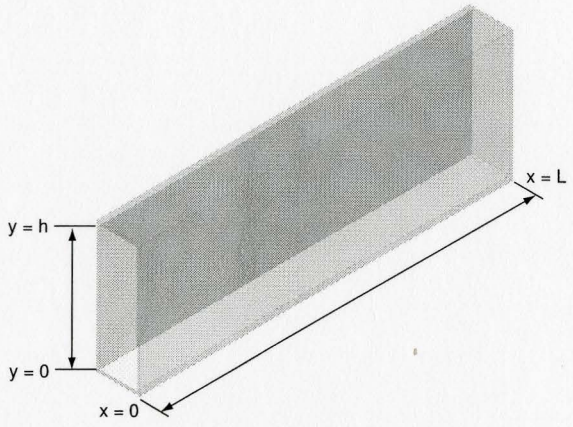

Figure 3.5: The open cavity.

$$\nabla^2 p = \frac{1}{c^2}\frac{\partial^2 p}{\partial t^2} \tag{3.2}$$

$$\left(\frac{\partial p}{\partial y}\right)_{y=0} = \left(\frac{\partial p}{\partial y}\right)_{y=h} = 0 \tag{3.3}$$

$$p(x=0) = p(x=L) = 0 \tag{3.4}$$

The boundary conditions defined in equation 3.3 and 3.4 shows that sine and cosines are appropriate forms for the solution to equation 3.2. Using this assumption and

application of the given boundary conditions, the pressure in a two dimensional duct can be expressed as:

$$\overline{p}(x,y,t) = P\sin\left(\frac{l\pi x}{L}\right)\cos\left(\frac{m\pi y}{h}\right)\cos\omega t \tag{3.5}$$

Kinsler et al. (2000) shows that the angular frequencies can be solved from the sine and cosine terms as (where l and m are integers):

$$f_a = \frac{c}{2}\sqrt{(l/L)^2 + (m/h)^2} \tag{3.6}$$

Along the middle of the test section, for $x = L/2$, the acoustic pressure will exhibit a maximum fluctuating amplitude, since the first sine term goes to unity at this point. For the test section, similar to that used by Mohany and Ziada (2005), Hanson et al. (2006) and Blevins (1985), the opposite ends in the stream wise direction are open, however, for simplicity, the first flow-excited resonance mode corresponds to $l = 0$ and $m = 1$, neglecting loses in the stream wise direction, which yields equation 3.7. This assumption is valid away from the open ends, where end effects are small.

$$\overline{p}(y,t) = P\cos\left(\frac{m\pi y}{h}\right)\cos\omega t \tag{3.7}$$

Thus, the frequency of the first mode acoustic resonance is given as:

$$f_a = \frac{c}{2h} \tag{3.8}$$

For a speed of sound, $c = 344$ m/s, and a test section height of 254 mm, the frequency of the first mode is approximately 677 Hz.

The Euler equation, equation 3.9, is used to determine the acoustic particle velocity.

$$\frac{\partial p}{\partial y} + \rho\frac{\partial v}{\partial t} = 0 \tag{3.9}$$

Solving for v, the acoustic particle velocity, assuming the $(0,1)$ mode, we arrive at:

$$v = \frac{P\pi}{\rho\omega L} \sin\left(\frac{\pi y}{L}\right) \cos\omega t \tag{3.10}$$

Plots of the normalized acoustic pressure, from equation 3.7, and acoustic velocity from equation 3.10, are given in figure 3.6 for the two extreme cosine terms (± 1). As shown, the acoustic particle velocity lags the acoustic pressure by $\pi/2$.

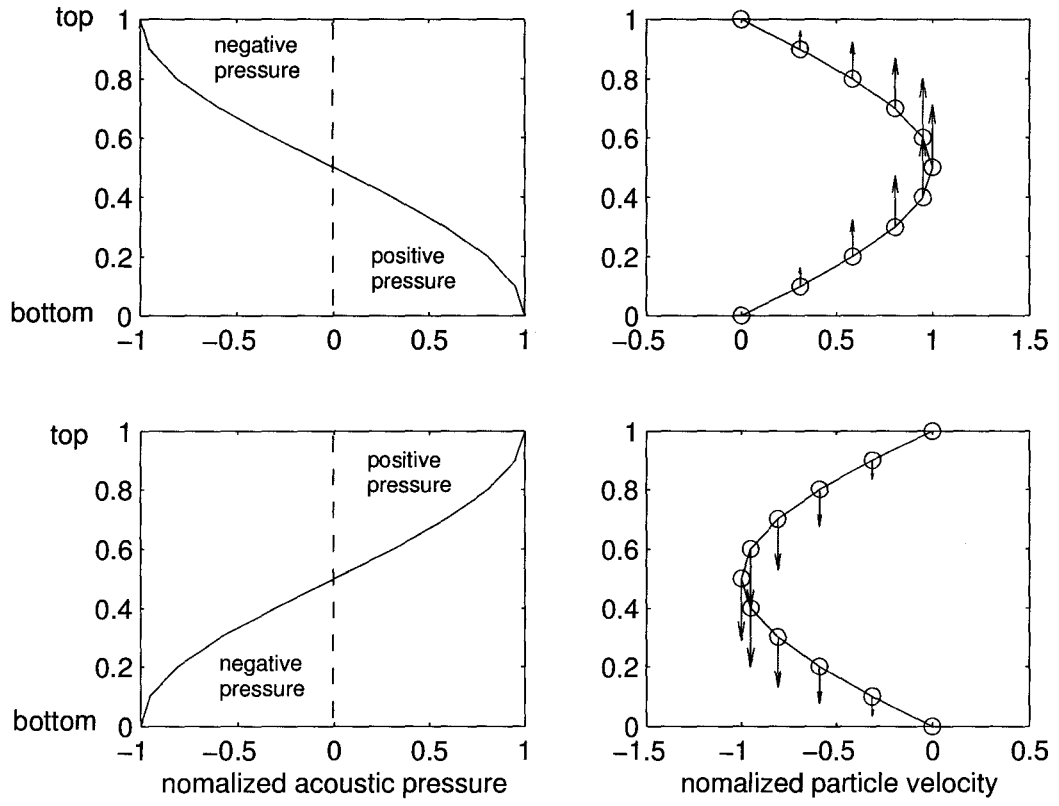

Figure 3.6: Acoustic pressure (left, top and bottom) and corresponding particle velocity, (right of each acoustic pressure schematic), in the test section, where arrows indicate the relative magnitude and direction described by the waveform.

3.4 Instrumentation

The following section is a summary of the instrumentation used in the experimental program, specifically that used for the dynamic lift measurements, and sound pressure level measurements.

3.4.1 Flow velocity

The flow velocity upstream of the tube bundle is measured using a pitot-static tube. The pitot-static tube is located 152 mm from the end of the parabolic contraction of the test section, shown in figure 3.3. This is used to measure the difference between the stagnation and static pressure allowing the calculation of the flow velocity using Bernoulli's equation. Solved for velocity, this is given by equation 3.11. V_u is the upstream flow velocity, ρ is the density of the air and $p_t - p_s$ is the difference in the stagnation and static pressure. The pitot-static tube is used only during calibration of the flow velocity for each tube array tested, and is then removed before aeroacoustic testing is conduced.

$$V_u = \sqrt{\frac{2(p_t - p_s)}{\rho}} \tag{3.11}$$

3.4.2 Microphones

G.R.A.S. 1/4" condenser microphones are used to measure the fluctuating sound pressure at the top wall (directly above the instrumented cylinder) of the test section. The microphones have a flat response over a wide frequency range (10 - 25k Hz) within 1dB. The microphone is mounted flush against the top plate of the test section. Microphones are calibrated using a *G.R.A.S*[†] Sound calibrator, Type 42*AB*, which

[†]G.R.A.S is a registered trademark of G.R.A.S. Sound and Vibration

delivers a sinusoidal wave of 114 dB at 1 kHz. The calibration of the microphone was done according the following steps:

- Determine the output voltage of the microphone corresponding to 114 dB generated by the pistophone, at 1000 Hz, by applying equation 3.12 where P_{ref} is the threshold of human hearing, $(20\mu\ Pa_{rms})$.

$$114dB = 20\log(\frac{P_{rms}}{P_{ref}}) \tag{3.12}$$

- Find the relationship between the signal from the microphone (V_{rms}) and the acoustic pressure (P_{rms}). The graph in figure 3.7 is a typical amplitude spectrum for the applied signal from the pistophone.

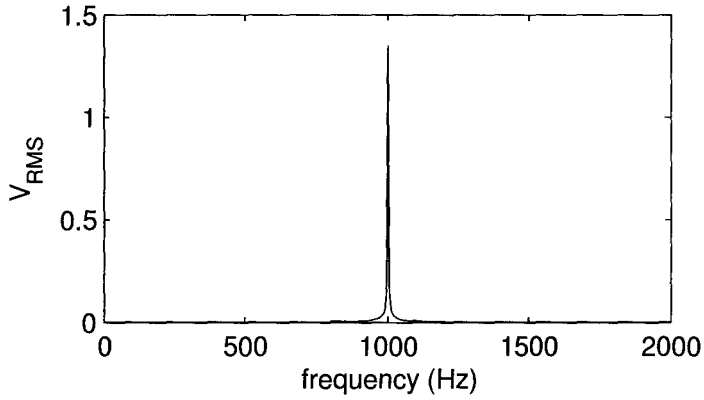

Figure 3.7: Typical amplitude spectra from the microphone during calibration.

3.4.3 Load cells and the dynamic lift

To measure the fluctuating lift forces, a rig similar to that constructed by Mohany and Ziada (2006) is used. A primary component in the rig constructed by Mohany and Ziada (2006), is the beam spring. This is designed to be extremely stiff parallel

to the flow direction, but less stiff in the lift direction, where it must be sensitive enough to measure the dynamic lift. The reason for this design criteria stems from the requirement to measure the lift forces only, which are investigated in the present study. For the beamspring/cylinder combination of Mohany and Ziada (2006), the natural frequency of the translational mode is near 1300 Hz.

A characteristic of the flow through a tube bundle is the strong broadband turbulence response, compared to measurements of single and tandem cylinders. The beam spring/load cell system is reconstructed to be stiffer in all directions, to reduce the effects of broadband turbulent buffeting occurring in tube bundles, (Paidoussis 1983). The natural frequency, $\omega_n = (k/m)^{0.5}$, will increase with an increased stiffness. An isometric view of the dynamic lift measurement rig, is shown in figure 3.8 and mounted on the test section in figure 3.4.

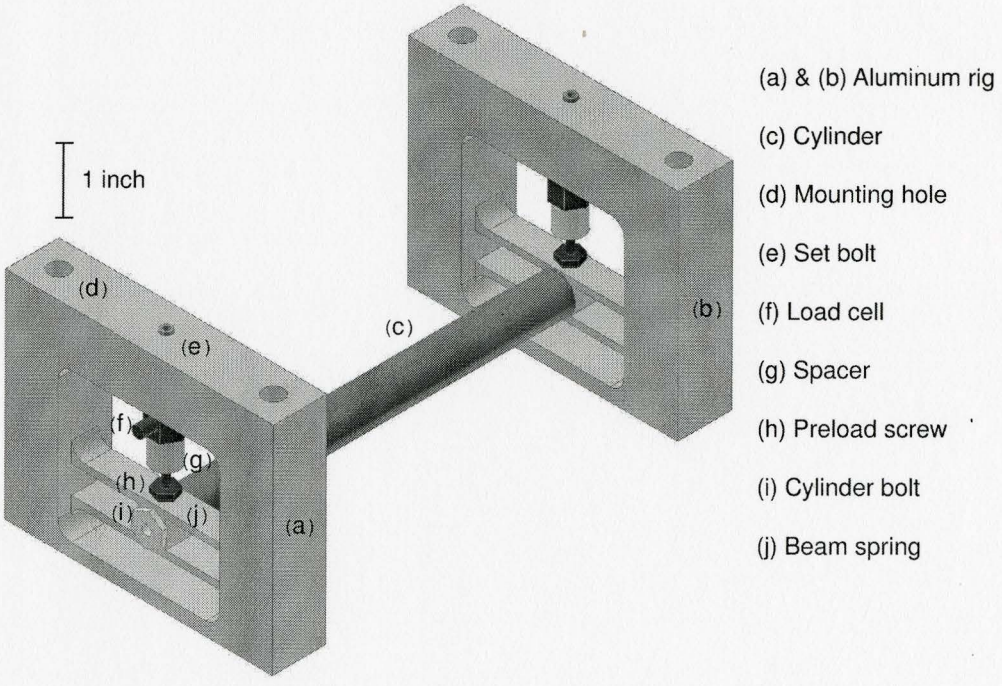

Figure 3.8: Dynamic force measurement rig shown with labeled components.

The beamspring/cylinder system is essentially a two degree of freedom system; there is one mass (the cylinder) and two springs (beam springs) at either end of the cylinder as shown in figure 3.8. For a system with one mass, its position and orientation is determined by knowing the rotational angle, and center of mass location. Two modes of vibration can occur. Typically, the translational mode (shown in figure 3.9) will be at a lower frequency than the rotational mode (shown in figure 3.9), but depends on the moment of inertia, mass of the cylinder and spring stiffness.

For the translational and rotational mode, shown in figure 3.9, the equations of motion, assuming an undamped system, are given by equation 3.13 and 3.14, respectively. The length of the cylinder is L, and the springs are assumed to have a stiffness of $k/2$. The moment of inertia about the center of mass is assumed to be $(1/12)mL^2$. A reference point is set at the center of mass, where the angle is measured from the cylinder axis. It is clear from these equations that the natural frequency of the rotational mode will be a factor of $(6/L)^{0.5}$ higher than the translational mode. For a cylinder length of 0.152 m, this corresponds to a factor of 6.3.

$$m\ddot{x} + kx = 0 \tag{3.13}$$

$$\frac{1}{12}mL^2\ddot{\theta} + \frac{1}{2}kL\sin\theta = 0 \tag{3.14}$$

No attempts were made to analytically determine the values of the natural frequencies, this is done using experimental methods such as the pluck test. Results of the pluck test are shown in figure 3.10. It is clear that only one dominant frequency component is visible, near 1800 Hz. This is typical for pluck tests done at the center of the cylinder span. Test are also conduced off center in an attempt to determine the rotational mode frequency, however they were unsuccessful in identifying a higher mode frequency. As shown previously this frequency would be much higher, and therefore far removed from the frequency range of interest in this study.

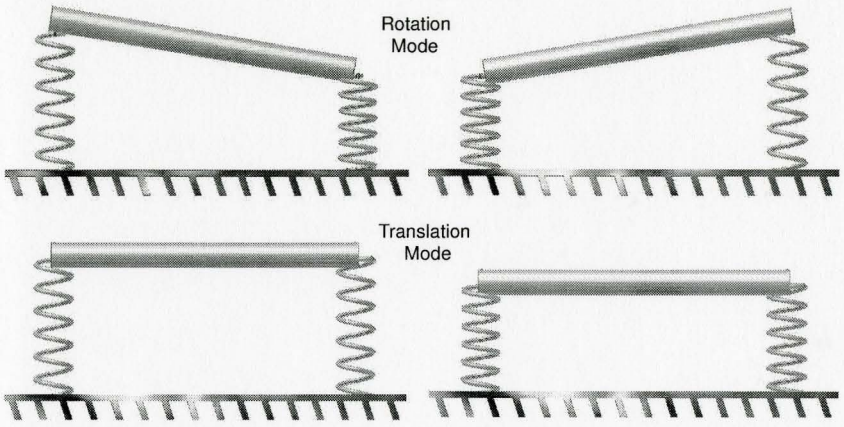

Figure 3.9: Two vibration modes possible for the two degree of freedom system.

3.4.4 Phase lag and magnification

Consider a single degree of freedom system, a simplification of the beamspring/cylinder, assuming the second mode effects are negligible, the ordinary differential equation governing the damped harmonic oscillator is given by equation 3.15. The damping ratio for a damped harmonic oscillator with mass m, damping coefficient c, and spring constant k, is given by equation 3.16. The natural frequency of a simple harmonic oscillator is given by equation 3.17,

$$m\frac{d^2x}{dt^2} + c\frac{dx}{dt} + kx = 0 \tag{3.15}$$

$$\zeta = \frac{c}{2\sqrt{k \cdot m}} \tag{3.16}$$

$$\omega_n = \sqrt{k/m} \tag{3.17}$$

Using the natural frequency of the simple harmonic oscillator, given in equation 3.17, and the damping ratio from equation 3.16, equation 3.15 can be written in the form given by equation 3.18.

$$\frac{d^2x}{dt^2} + 2\zeta\omega_n\frac{dx}{dt^2} + \omega_n^2 x = 0 \tag{3.18}$$

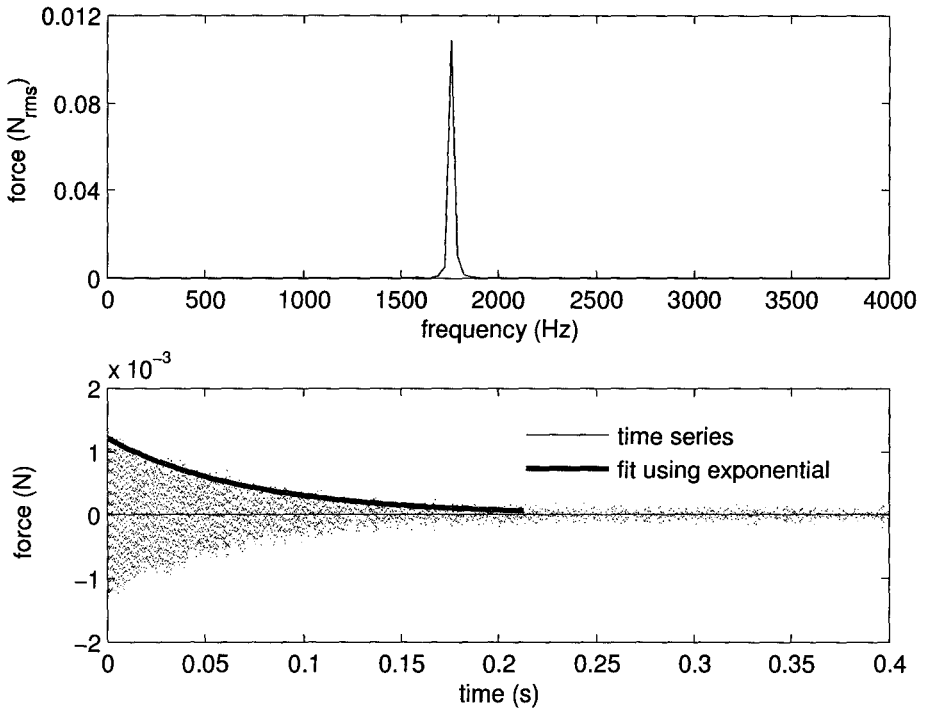

Figure 3.10: Frequency response of the dynamic load measurement rig during a pluck test (top). Time trace of the decaying amplitude after the pluck test showing the exponential fit of the data (bottom).

Assuming that the system is a damped harmonic oscillator, equation 3.19 will be a solution to the linear homogenous equation 3.18 .

$$x(t) = Ce^{st} \tag{3.19}$$

For the beam spring, the damping will be small. There will be two solutions to equation 3.15 of the form given by equation 3.20 & 3.21 .

$$x_1(t) = C_1 e^{s_1 t} \tag{3.20}$$

$$x_2(t) = C_2 e^{s_2 t} \tag{3.21}$$

Equation 3.20 and 3.21 are used to determine the general solution. The solution form will contain the exponential decay term:

$$e^{-\zeta\omega_n t} \tag{3.22}$$

The motion of a damped oscillator will have an angular frequency given by equation 3.23, and the amplitude of vibration will decay with time, as given by equation 3.22.

$$\omega_d = \sqrt{1-\zeta^2}\omega_n \tag{3.23}$$

From the exponential fit determined from figure 3.10, the following result is obtained:

$$\zeta\omega_n = 14.48$$

For a natural frequency of 1780 Hz from figure 3.10, the damping ratio is calculated to be: $\zeta = 0.0013$.

The phase lag for a single degree of freedom system, can be expressed in terms of the frequency (natural and driving) and the damping ratio, of which all are known. The phase lag is defined by equation 3.24, where ζ is the damping ration, Ω and ω are the driving and natural system frequency respectively. The phase response is plotted in figure 3.11 and shows that for frequencies less than the natural dynamic system frequency, the phase shift is essentially zero. For this reason, no corrections are made to the phase shift between the microphone and the dynamic lift measurements.

$$\phi = \cos^{-1}\left[\frac{\Omega^2-\omega^2}{\left(\left(\Omega^2-\omega^2\right)^2+4\zeta^2\Omega^2\omega^2\right)^{1/2}}\right] \tag{3.24}$$

For the single degree of freedom system, the load cells will measure a force amplified by the natural response of the system. The theory on force amplification can be found in Rao (2004), or in Oengören and Ziada (1992). The ratio of the force measured to the real force can be evaluated using equation 3.25, in which r is the frequency ratio, Ω/ω. The magnification of the force measured is shown in figure 3.11. At the frequency of interest, 680 Hz, the correction factor is approximately 1.17.

$$\frac{F_{MEAS}}{F_{REAL}} = \sqrt{\frac{1+(2\zeta r)^2}{(1-r^2)^2+(2\zeta r)^2}} \tag{3.25}$$

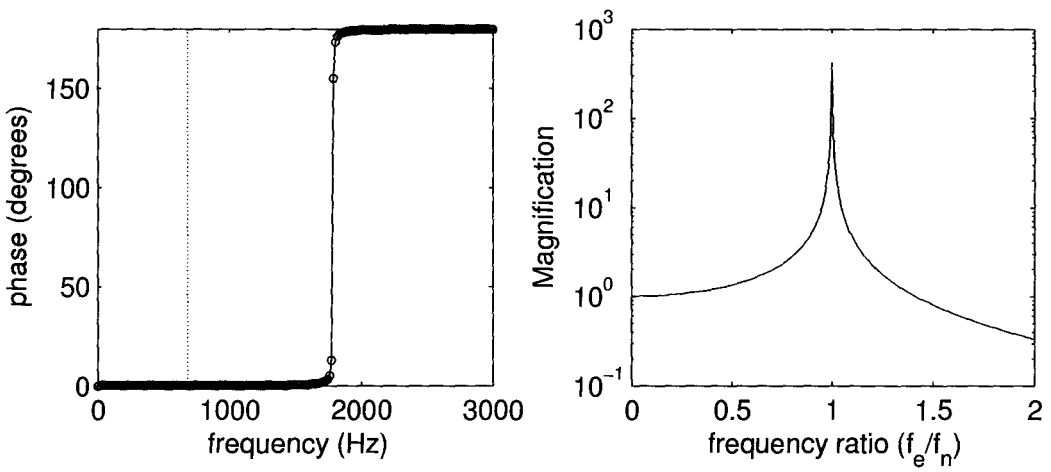

Figure 3.11: Phase shift between the excitation source the dynamic response (left). The dashed line is shown at the first transverse acoustic mode frequency of the test section. Magnification factor of the force response as a function of the driving frequency (right).

Plots of the force magnification and phase shift are dependant on the value of the damping ratio. It is interesting to note the effect of a small damping ratio on these plots. Neglecting the damping term, equation 3.25 reduces to equation 3.26. Since the damping measured is small, the reduced equation gives a magnification factor within 0.1%.

$$\frac{F_{MEAS}}{F_{REAL}} = \frac{1}{1-r^2} \tag{3.26}$$

Chapter 4

Dynamic Lift Due To Sound

Standing acoustic waves produce time dependant pressure gradients in the test section. The result of this pressure gradient is an induced pressure on the surface of the cylinders in the tube array causing a net periodic lift force. This section investigates the pressure gradients on the cylinder surfaces, its origins and the magnitude of the induced lift forces.

4.1 Dynamic lift amplitude in an acoustic standing wave - analytical

The shape of the first transverse acoustic mode in the test section, without tubes, with the dimensions used in these experiments and with an open inlet and exit is shown in figure 4.1.

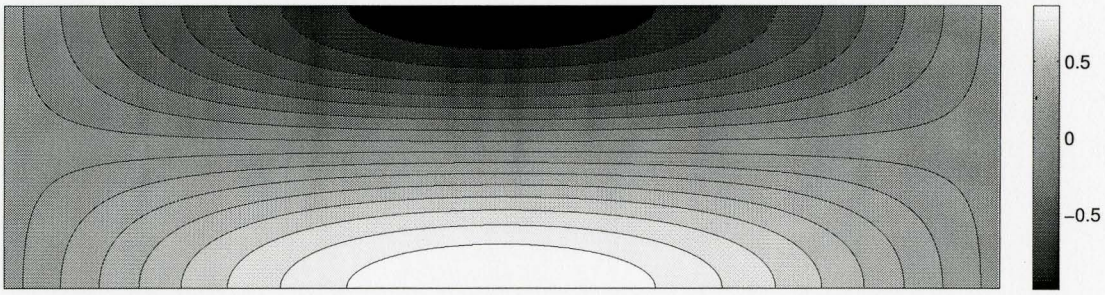

Figure 4.1: Normalized mode shape of the first transverse acoustic mode solved in ANSYS. The colorbar is a linear scale showing the pressure distribution.

At the center of the test section, the vertical pressure distribution of the first transverse acoustic mode yields a sinusoidal pressure distribution with a pressure node in the middle. Assuming this is valid with tubes present, it is possible to calculate the amplitude of the dynamic load that would be applied at the tube surface due to an imposed sinusoidal pressure distribution. Feenstra et al. (2005) did precisely this and explain the method and mathematical derivation. For a cylinder at the test section center, or pressure node location, the centerline of the cylinder would essentially see zero pressure, however the top and bottom halves of the cylinder surface would see positive and negative pressures respectively at an instant in time. The standing wave will, in one instant, produce positive pressure along the top of the cylinder, and negative pressure along the bottom surface. At another instance in time, the pressure loading will be reversed, thus over time, the loading of the cylinder will be periodic at the frequency of the standing wave. Feenstra et al. (2005) derived the equation for the lift amplitude generated for a cylinder in a standing wave. The spatial distribution of the acoustic pressure would be given by equation 4.1.

$$P(x) = P_o \sin\left(\frac{nx}{h}\right) \tag{4.1}$$

Where: h is the test section height, P_o is the peak acoustic pressure and n is the mode number. For a cylinder located at the center of the test section, the dynamic lift, per unit length, can be expressed as a function of P_o, the cylinder diameter D, and the test section height h. Feenstra et al. (2005) also added a component due to the drag forces expected from the acoustic particle velocity as shown in equation 4.2. The value U_{peak} is determined from equation 3.9.

$$w = \underbrace{P_0 D \int_0^{\pi} \sin\left[\frac{\pi}{h}\left(\frac{D}{2}\cos\theta\right)\right]\cos\theta d\theta}_{\text{Pressure Contribution}} + \underbrace{\frac{D}{2}\rho C_D U_{peak}^2}_{\text{Particle Velocity Contribution}} \tag{4.2}$$

Using the method of Feenstra et al. (2005), the dynamic lift amplitude as a function of the maximum acoustic pressure at the top center of the test section is determined as shown in figure 4.2. The two cylinder diameters used in the present study are shown for a test section height of 254 mm.

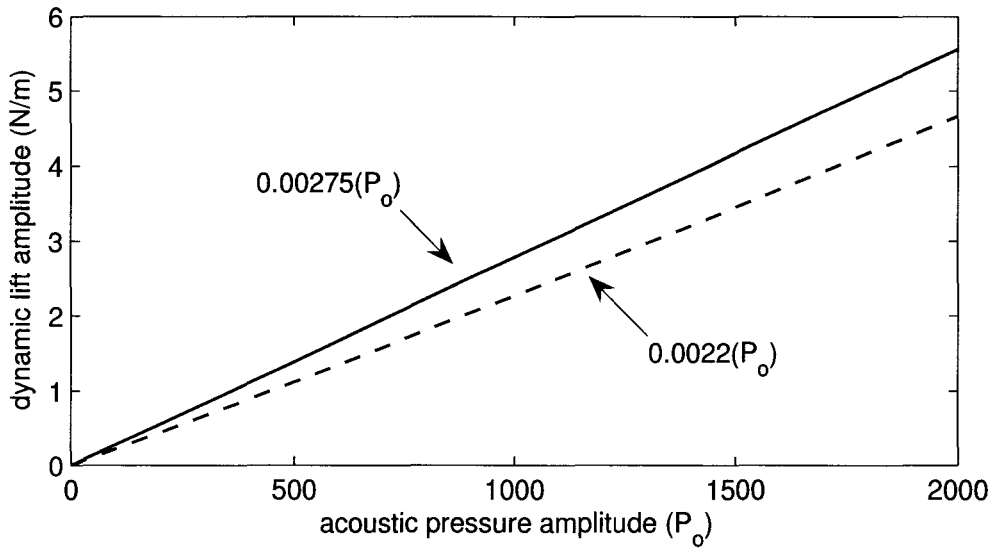

Figure 4.2: Dynamic lift amplitude as a function of the acoustic pressure using the equation developed by Feenstra et al. (2005). *solid line*, $D = 16.67$ mm; *dashed line*, $D = 15.08$ mm.

An important finding for the present geometry is that the particle velocity contribution can be neglected. The response shown in figure 4.2 is linear with a slope of $0.0022(P_o)$ for the smaller cylinder with $D = 15.08$ mm, and a slope of $0.00275(P_o)$ for the larger cylinder with $D = 16.67$ mm. Since the plot is linear, it is evident that the contribution due to the acoustic particle velocity is small, and can be neglected in these cases. The results determined from the method of Feenstra et al. (2005) are referred to hereafter as the sine wave distribution results.

4.2 Numerical simulation of the acoustic mode

4.2.1 Background and theory

The finite element program, ANSYS*, is used to solve the acoustic mode shape and the acoustic pressure distribution in the modeled test section. Discretization of the wave equation (3.2), from §3.3.1, is used to determine the equation of motion for acoustic nodal pressures, in matrix form, by equation 4.3, assuming the system is undamped.

$$M\ddot{p}(t) + Kp(t) = 0 \tag{4.3}$$

Where M is the mass matrix and K is the stiffness matrix.

For a linear system, the vibration will be harmonic and of the form:

$$P_i = \varphi_i \cos(\omega_i t) \tag{4.4}$$

Where φ_i is the eigenvector associated with the *ith* natural frequency, ω_i is the *ith* natural angular frequency and t is the time. Substituting 4.4 into 4.3 yields:

$$(K - \omega_i^2 M)\varphi_i = 0 \tag{4.5}$$

For a non-trivial solution this corresponds to the following equation:

$$K - \omega_i^2 M = 0 \tag{4.6}$$

This equation represents an eigenvalue problem, for which the determinant can be solved for n values of ω eigenvalues, and n eigenvectors, where n is the number of all the degrees of freedom.

*ANSYS is a registered trademark of ANSYS, Inc.

4.2.2 Numerical results

For each of the three tube arrays, the first transverse acoustic mode is simulated numerically. The domain is two dimensional, wherein the dimensions correspond to those of the actual test section. The domain is meshed with 2D acoustic elements. This resulted in a minimum of 30000 nodes for the three cases studied. The surface of the cylinders typically contains a minimum of 100 equally spaced nodes.

To determine the force amplitude of the imposed pressure field, the pressure field is integrated around the cylinder surface. For the three tube arrays, the pressure field around the cylinder surface is plotted in figure 4.3 along with the sine wave distribution for both cylinder diameters. Note that for the smaller cylinder diameter, the sine wave distribution follows the same curve as the larger diameter but ends at the y-coordinate of the numerical results corresponding to the same diameter. Integration of the pressure distribution around the surface of the centrally located cylinder for the small, intermediate and large spacing ratio square tube arrays yields a maximum lift amplitude of 0.0033, 0.0046 and 0.0041 N/m, respectively, for the normalized pressure distributions. In order to compare the results for the different tube arrays, the acoustic pressure on the test section wall is normalized to 1 Pa.

An important finding from the present results is the disagreement between the sine wave distribution and that of the numerical results. Figure 4.3 shows that the sine wave distribution underestimates the pressure distribution determined by the numerical simulation. Mohany and Ziada (2006) observed in the simulation of the acoustic modes that the particle velocity distribution was distorted in the region near the cylinders, as the acoustic streamlines had to go around the cylinder. Since the instrumented cylinder is located at a pressure node in the test section, it experiences the greatest pressure derivative and the highest particle velocity. At the walls of the cylinder, the normal particle velocity is zero, meaning that normal to the cylinder

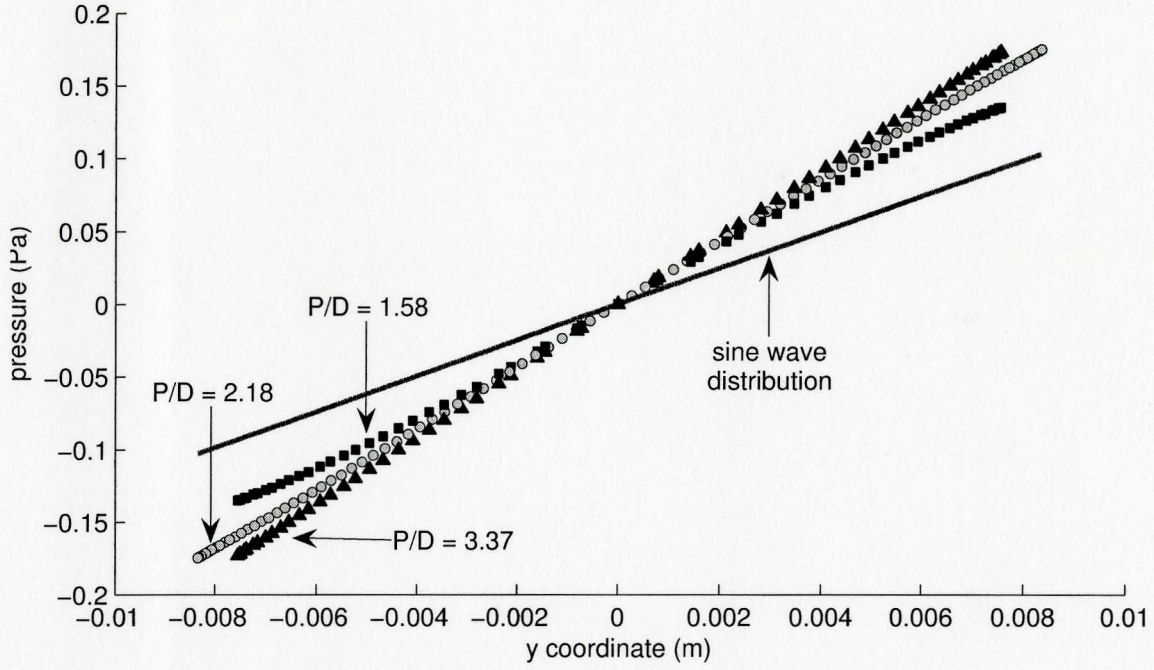

Figure 4.3: Surface pressure contours determined by numerical simulation for the tube arrays. ■, small array, $D = 15.08$ mm; ○, medium array, $D = 16.76$ mm; ▲, large array, $D = 15.08$ mm; *solid line*, sine wave distribution.

walls, the pressure derivative is also zero. This distortion is believed to cause the changes in the observed lift force amplitude when comparing the sine wave analytical method with the numerical method.

It is shown in §4.1 by figure 4.1 that the acoustic pressure is a maximum along the center of the top of the test section for the first transverse acoustic mode. Below this point, at the center of the test section, the derivative of the acoustic pressure is a maximum at this pressure node, as can be justified from a sinusoidal pressure distribution. It is therefore expected that the cylinder located at this pressure node should experience the maximum lift amplitude due to the acoustic pressure loading on the cylinder surface. To investigate the changes in acoustic lift amplitudes for the other tubes in the large spacing array, the acoustic pressure loading around the cylinders

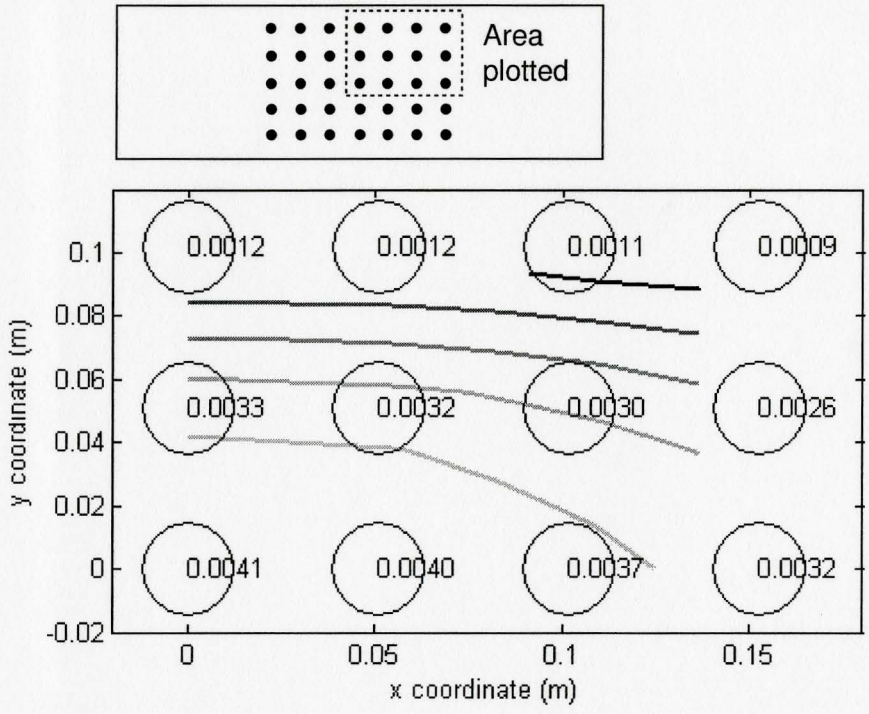

Figure 4.4: Maximum lift amplitude of tubes in an inline array with $P/D = 3.37$, subject to the first transverse acoustic mode for one quadrant. The numbers given in this figure are lift values in N/m and are referenced to a normalized acoustic pressure of 1 Pa at the top of the array

located in one quadrant of the test section is determined numerically. The results are displayed in figure 4.4. Clearly, the maximum lift amplitude due to the acoustic loading occurs at the center tube, and decreases away from the center location.

4.3 Dynamic lift of a central tube in an acoustic standing wave - experimental

The experimental results of the amplitude of the lift on the central tube are performed using the tube arrays in the presence of an acoustic standing wave, excited by the loud speakers, as described in the previous chapter. Corrections of the magnification factor are made, as well to the effective length of the cylinder. It is found that for the three different test sections, the cylinder length exposed to the standing wave was increased by as much as +3% due to bowing of the test section walls which occurred during assembly. The arrays were excited at their resonance frequency of the first transverse acoustic mode, which varied slightly from one array to another because of the difference in the number of tubes which are known to affect the speed of sound in the array as discussed in §2.4.4. White noise is used first to determine the appropriate resonance frequency from the fast fourier transform (fft) of the microphone response. The array was then excited at this frequency. Typical responses of the load cells and microphone are shown in figure 4.5 with excitation provided by the loudspeakers.

4.3.1 Protected cylinder tests

Using the load cell rig, described in section 3.4, an initial test, similar to that of Oengören and Ziada (1992), was performed to confirm that the vibration transmission to the measurement apparatus from the test section is indeed small. The cylinder was enclosed in larger diameter hollowed aluminum cylinder, shown in figure 4.6, to shield it from the periodic acoustic pressure.

A standing wave was applied both with and without the cylindrical shield. This was done over several levels of excitation, and it is found that the vibration transmission accounts for only 2% to 3% of the measured lift force without the shield.

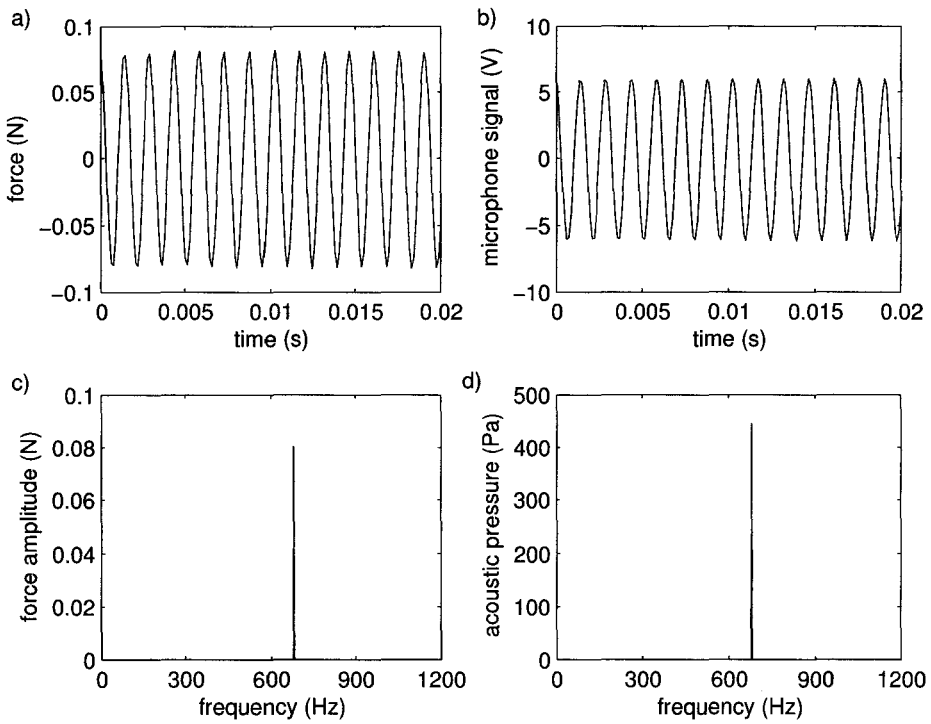

Figure 4.5: Typical time signal from the load cell (a), microphone, (b), and the corresponding amplitude spectra, (c) and (d).

Figure 4.7 shows the results for one level of excitation, illustrating amplitude spectra of the load cell signal with and without the shield.

4.3.2 Experimental results

All the three inline tube arrays are tested in the presence of an acoustic standing wave over various excitation levels ranging in amplitude from 50 to 1500 Pa. The results are shown in figure 4.8. Both the experimental (data markers), as well as the numerical solutions (dashed lines) are shown. In all the cases, it is found that the measured dynamic lift amplitudes are slightly lower than the numerical solution, in the range of 5%. It should be noted that the numerical solution is two dimensional, but in the experiments there will be some distortions of the acoustic mode at the

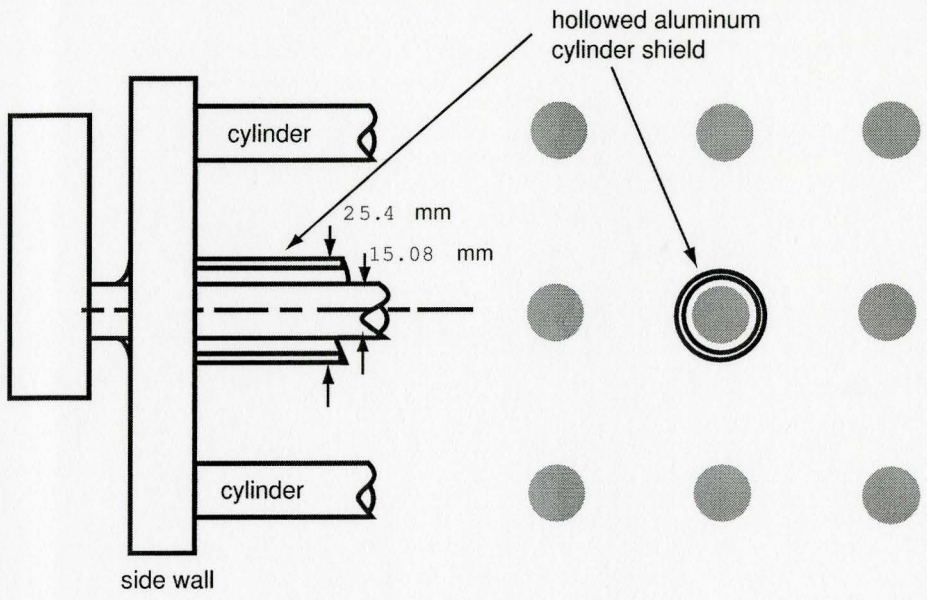

Figure 4.6: Schematic of the large spacing inline array with the hollowed aluminum cylinder shielding the central tube.

ends of the cylinders. The dynamic lift is found to increase linearly with the acoustic pressure, as expected from the numerical simulations. The figure also shows the prediction of the sine wave distribution which underestimates the measured dynamic lift forces by up to 70%. A summary of the experimental and numerical results are listed in table 4.1.

Table 4.1: Results of the dynamic lift in N/m referenced to a normalized acoustic pressure of 1 Pa at the top wall of the test section.

Array	Diameter	Experimental	Numerical	Sine wave distribution
$P/D = 3.37$	15.08 mm	0.0038	0.0041	0.0022
$P/D = 2.18$	16.67 mm	0.0043	0.0046	0.00275
$P/D = 1.58$	15.08 mm	0.0031	0.0033	0.0022

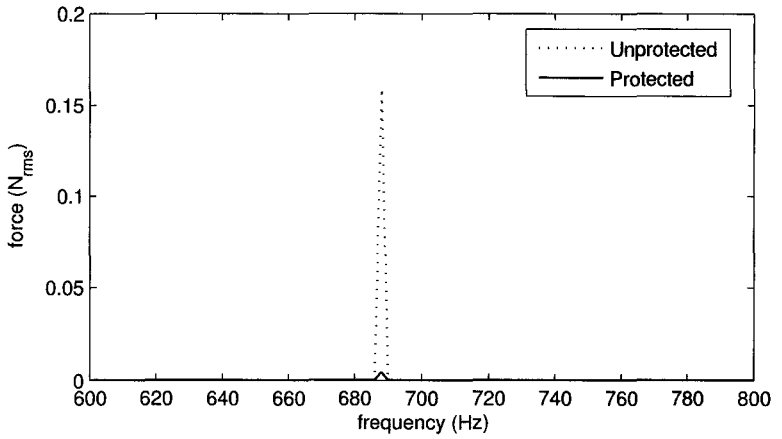

Figure 4.7: Dynamic lift measurement with and without the hollowed aluminum cylinder shielding the central tube.

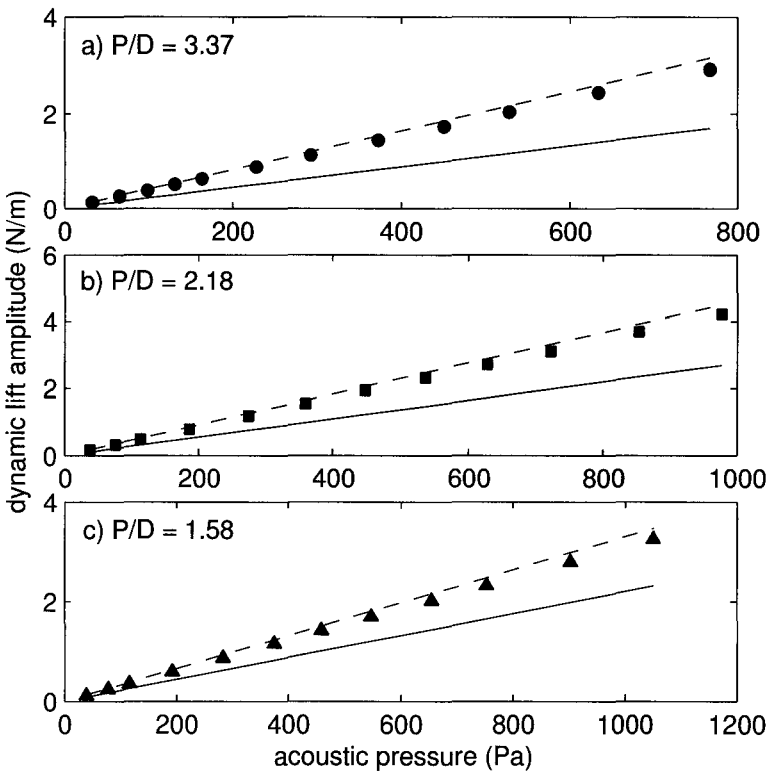

Figure 4.8: Acoustic lift force on the central cylinder in the square tube array obtained experimentally (using acoustic excitation only) and by means of the numerical solutions. (a), large spacing; (b), intermediate spacing; (c), small spacing ratio. Data markers show the experimental points, the dashed lines show the solution determined by the numerical simulation. The solid lines show the prediction of the sine wave distribution.

4.4 Effect of the tube diameter to wavelength ratio

From section 4.3.2, it is found that the direct dynamic lift measurements, conducted using loudspeakers, agree well with the numerical simulation. The present results are therefore extended to a large range of shell and tube geometries by determining the effect of the ratio between the tube diameter and the acoustic wavelength ($D/lambda_{1/2}$) on the dynamic lift using the numerical simulation. For the first transverse acoustic mode, the acoustic mode length scale is referred to $lambda_{1/2}$, since this mode consists of a half wavelength, with a pressure node located at the test section center, as shown in figure 4.1. A summary of the effect of $D/lambda_{1/2}$ is shown in figure 4.9.

The diameter of the cylinders is kept the same as those used in the previous geometries, however the test section height is increased by the factors of 2, 4, 6 and 8 to produce the ratios of $D/lambda_{1/2}$ which are plotted on the *x-axis* in the range of 0.0074 to 0.06 for the small and large arrays, and in the range of 0.0082 to 0.065 for the intermediate array. The larger values from the pairs of numbers represent the ratio of $D/lambda_{1/2}$ used in the current experimental investigation. Additional tubes are added to fill in the area spanning from the top to bottom wall of the test section.

A linear behavior between the ratio of $D/lambda_{1/2}$ and the predicted dynamic lift amplitude is shown in figure 4.9. The effect of increasing the test section height is to decrease the ratio of $D/lambda_{1/2}$. It is shown by figure 4.10(a) that the ratio of the numerical simulation results, or actual dynamic lift due to sound, denoted by L_{ACT}, to those of the sine wave distribution, L_{SWD}, remain constant over the range of diameter to wavelength ratios tested. For the three arrays with $P/D = 3.37$, $P/D = 2.18$ and $P/D = 1.58$ this ratio is 1.86, 1.71 and 1.52, respectively. For the

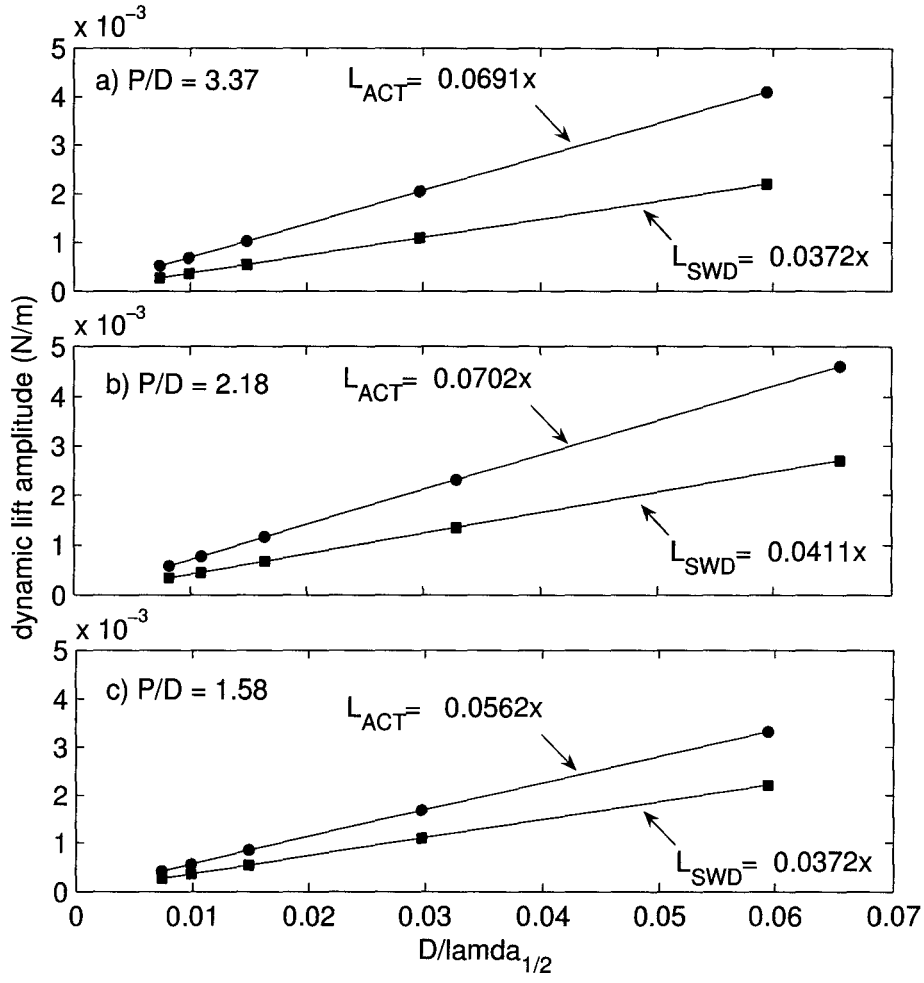

Figure 4.9: Effect of $D/lambda_{1/2}$ on the dynamic lift amplitude for, (a), $P/D = 3.37$; (b) $P/D = 2.18$; (c), $P/D = 1.58$. •, Numerical results; ■, Prediction using the sine wave distribution.

three arrays, the variation in the ratio is found to be less than two percent and may be attributed to numerical error associated with the integration of the points around the cylinder surface.

Figure 4.10(b) shows the variation in L_{ACT}/L_{SWD} with the spacing ratio of the arrays. For the large and small array, with the same tube diameters and wavelength, the sine wave distribution model gives the same value for the dynamic lift amplitude in each of these two arrays as shown in table 4.1. It is shown by figure 4.10(b) that the

dependance of the dynamic lift force on the spacing ratio is non-linear. The spacing ratio effect on the dynamic lift becomes stronger as the spacing ratio is reduced. Increasing the spacing ratio will decrease this observed effect, and although only three points are plotted, further increases in the spacing ratio are likely to exhibit little change in the ratio between L_{ACT}/L_{SWD}.

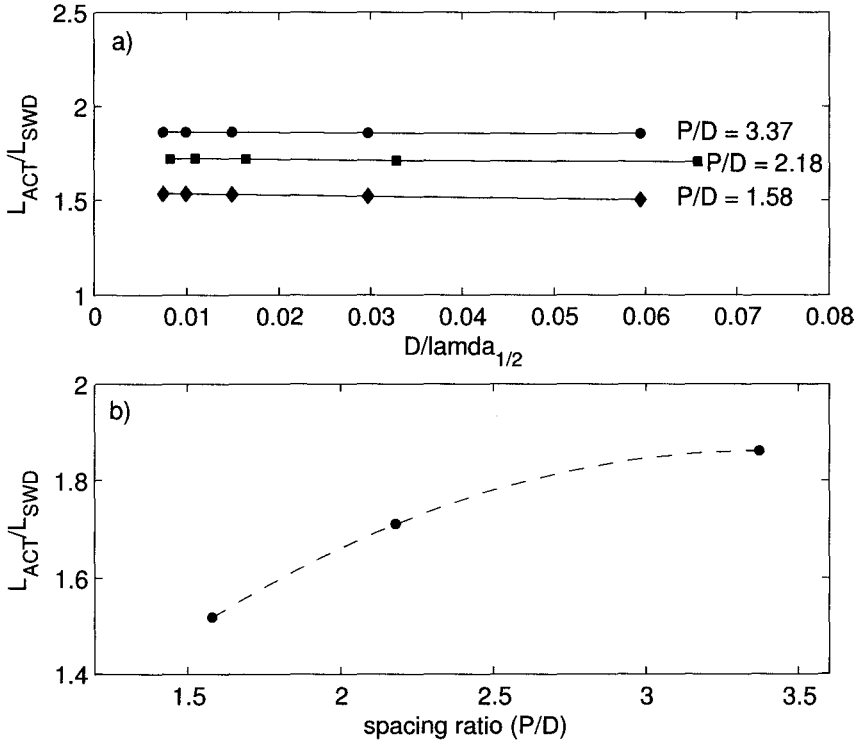

Figure 4.10: Ratio of the actual dynamic lift amplitude to that determined from the sine wave pressure distribution method, L_{ACT}/L_{SWD}, with respect to the diameter to wavelength ratio, $D/lambda_{1/2}$, in figure (a), and with respect to the spacing ratio in figure (b).

4.5 Discussion

The current chapter investigated the dynamic lift amplitude due to a first mode transverse acoustic standing wave on the center cylinder in an array and thereby located at the pressure node. First, using a simple approach, the dynamic lift ampli-

tude is determined by the sine wave distribution. The sine wave distribution method underestimates the dynamic lift amplitude determined by the two dimensional numerical simulations of the acoustic pressure mode shapes. Experimental results validated the numerical simulation, and showed linear increase in the dynamic lift amplitude with the acoustic pressure level. It is observed that the acoustic pressure distribution is distorted around the surface of the cylinder. The distortion of the acoustic pressure distribution, in the region of the cylinders, caused the underestimation of the numerical and experimental results by the sine wave distribution method.

The investigation is extended to a larger operating range of tube diameter to wavelength ratios after it was shown that the numerical simulations agreed well with the experimental results. The numerical simulations show a linear behavior between the dynamic lift and $D/lambda_{1/2}$, with a constant ratio between these results and those of the sine wave distribution. This ratio can be used to determine the actual lift amplitude by multiplying the ratio by the result of the sine wave distribution. A non-linear behavior between L_{ACT}/L_{SWD} and the spacing ratio is observed. This ratio is found to increase with the spacing ratio.

The results from this chapter extend the experimentally determined results to a much more complete range of spacing ratios and diameter to wavelength ratios using the validated numerical simulation. Boilers and heat exchangers found in industry may have shell diameters as large as several meters, and tube diameters as small as several centimeters, encompassing a large range of $D/lambda_{1/2}$ ratios. In some experiments, such as those of Oengören and Ziada (1992b) and Ziada and Oengören (1993), for example, higher order acoustic modes are excited. The present investigation did not consider these higher modes, however it is believed that the present results are applicable to the higher order modes as long as the ratio, $D/lambda_{1/2}$, is considered.

Chapter 5

Experimental Results

This chapter presents the experimental results of the effects of flow-excited acoustic resonance on the dynamic lift of square tube arrays. Three spacing ratios are investigated, large, intermediate and small spacing arrays corresponding to $P/D = 3.37$, $P/D = 2.18$ and $P/D = 1.58$, respectively. Both the aeroacoustic response and the dynamic lift of a central tube in the tube bundles is presented. Phase measurements compliment measurements of sound pressure level and dynamic lifts. From these phase measurements, it is possible to decompose the total dynamic lift forces measured on the central tube into two components. One caused by the acoustic standing wave excited in the test section, and the other caused by the aerodynamic forces. The total dynamic lift force measured is due to the combined effects of both the acoustic pressure field and aerodynamic forces.

5.1 Large spacing square array results

5.1.1 Aeroacoustic response

Large spacing square tube arrays exhibit a single Strouhal number which is relatively constant over a large range of Reynolds numbers. The gap velocity is varied between approximately 10 and 80 m/s, corresponding to a range of Reynolds numbers between 1×10^3 to 8×10^4. Increasing the flow velocity leads to proportional increases

in the flow periodicity identified in these arrays. As the flow velocity is increased, the frequency of vortex shedding approaches that of the first transverse acoustic mode of the test section defined in §3.3.1. The aeroacoustic response of the large spacing ratio square tube array is shown in figure 5.1. This response is presented as a waterfall plot, where the *x-axis* defines the frequency of the amplitude spectra (Hz), the *y-axis* defines the flow velocity in terms of gap velocity (m/s), and the *z-axis* is the acoustic pressure level (Pa_{rms}).

The response shown by figure 5.1 reveals a familiar response identified as classical Strouhal excited acoustic resonance. Similarity between this response, and that of a single cylinder is evident, see for example Mohany and Ziada (2005). The lock-in region is readily identified in the waterfall plot. During lock-in, between 60 and 80 m/s, there is a large increase in sound pressure level to nearly 3500 Pa_{rms}, which corresponds to 165 dB.

For each of the spectra presented in figure 5.1, the frequency of vortex shedding, as well as the corresponding sound pressure level at that frequency is determined. The frequency of vortex shedding and the corresponding sound pressure levels are presented in figure 5.2. The points plotted show the frequency response as a function of the gap velocity and the corresponding acoustic pressures.

Increase in the vortex shedding frequency with gap velocity leads to a Strouhal number, based on the gap velocity, of $St_g = 0.16$. This result is typical of square arrays with a similar spacing ratio. Ziada (2006) reports a Strouhal number of 0.17 (shown in figure 2.16(a)), Weaver et al. (1987) report values between 0.15 and 0.21 obtained from empirical relationships developed by Zukauskas and Katinas (1980) and Owen (1965), which agree well with experimental data for large spacings. Lock-in occurs at the frequency of the first transverse mode excited in the test section. The lock-in region is identified in figure 5.2 as the series of points over a range of

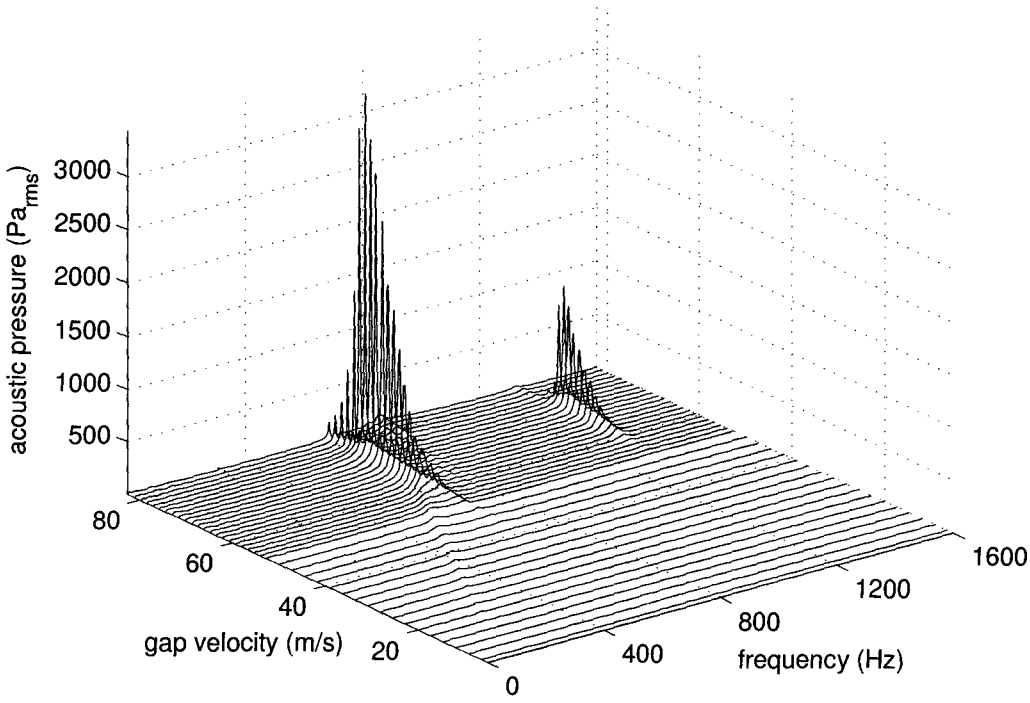

Figure 5.1: Waterfall plot of the aeroacoustic response of the square array with $P/D = 3.37$.

flow velocities remaining at a frequency of approximately 680 Hz. During lock-in, the acoustic sound pressure level increases to nearly 3500 Pa_{rms}. Maximum sound pressure level occurs at a gap velocity greater than where coincidence of the acoustic mode and the natural vortex shedding frequency occurs.

The present results shown by figure 5.2 compare well with the results of Ziada and Oengören (1993) shown in figure 2.19 in §2.4.2 for an inline array with $X_L/X_T = 3.23/3.75$. Large inline and square arrays exhibit classical Strouhal excited resonance, wherein acoustic resonance is excited by the vortex shedding periodicity present in the unexcited flow before coincidence. The coincidence acoustic resonance shown by figure 2.19 is similar to the square tube array results shown by figure 5.2. Thus, the

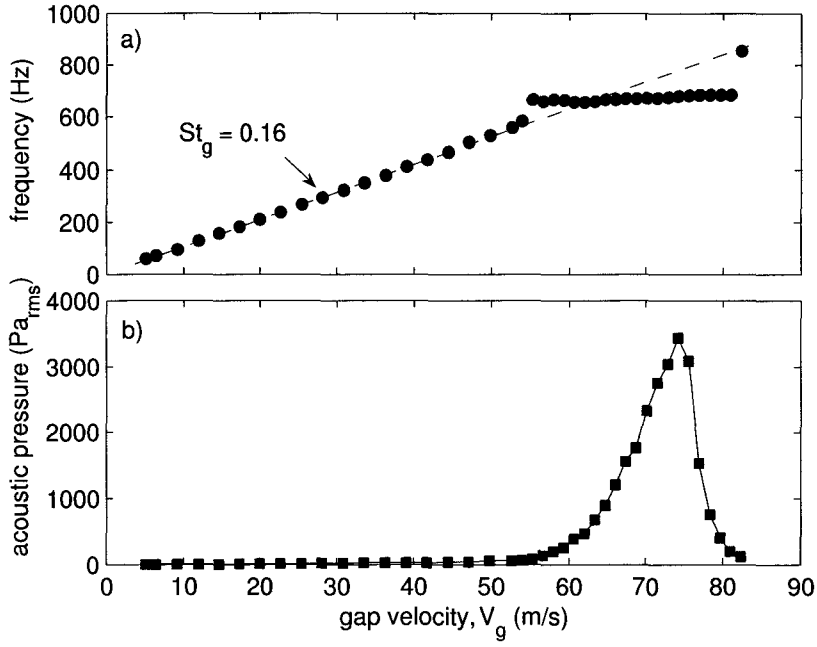

Figure 5.2: Aeroacoustic response for a square tube array with $P/D = 3.37$. Figure (a) shows the frequency response, •; figure (b) shows the acoustic pressure, ■, at the frequency of vortex shedding and with respect to the gap velocity.

excitation mechanism is expected to be the same for the present case and that of Ziada and Oengören (1993).

5.1.2 Dynamic lift response

Dynamic lift measurements of the central cylinder in the array are conduced over the entire range of gap velocities, in both non-resonant and acoustic resonance conditions. The lift amplitude per unit length of the cylinder is calculated by summing the measured lift amplitude by each of the two load cells, and dividing by length of the cylinder exposed to the flow field.

The waterfall plot given by figure 5.3 shows the lift amplitude spectra for one of the load cells. The *x-axis* defines the frequency of the amplitude spectra (Hz), the *y-axis* defines the flow velocity in terms of gap velocity (m/s), and the *z-axis* is

the amplitude of the lift force (N). Before the onset of acoustic resonance, a linear increase in the dynamic lift frequency is visible which corresponds to the Strouhal number of 0.16 identified in §5.1.1. During the peak acoustic resonance pressures, additional peaks in the spectra appear and are attributed to higher harmonics. The second peak is at a frequency of $2f_a$, where f_a is the frequency of the first transverse acoustic mode, approximately 680 Hz.

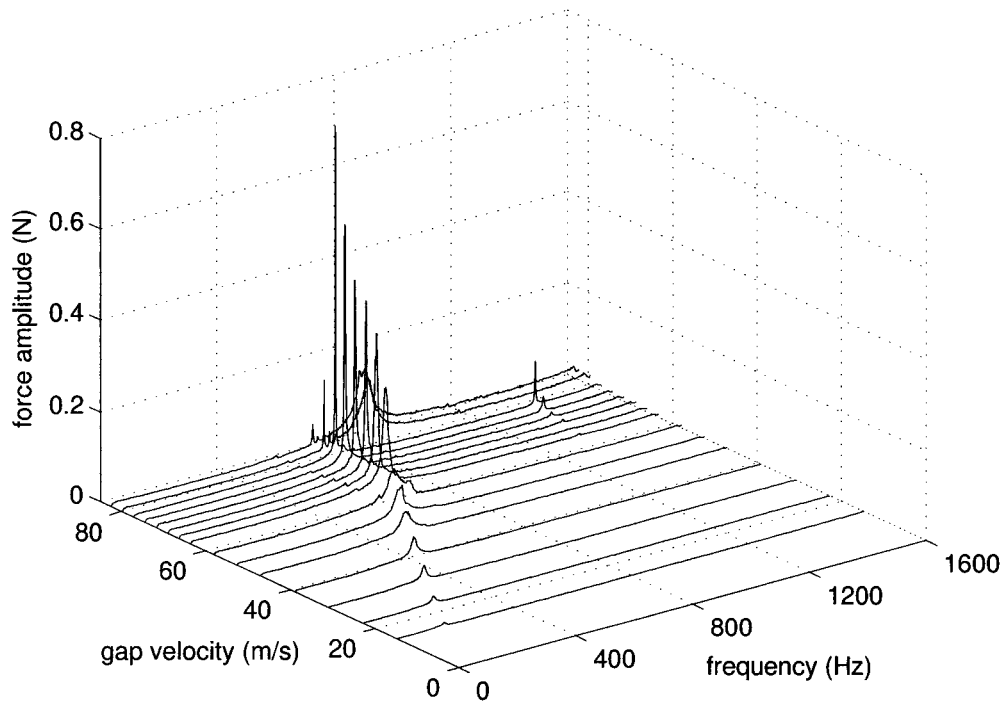

Figure 5.3: Dynamic lift amplitude spectra from one load cell for the square tube array with $P/D = 3.37$.

Figure 5.4 shows sets of spectra wherein each set is composed of the acoustic pressure amplitude spectrum and corresponding dynamic lift amplitude spectrum. The dominant contribution to the dynamic lift occurs at the same frequency as the flow periodicity observed in the acoustic response at the vortex shedding frequency. The microphone signals show spectral peaks at approximately 680 Hz corresponding

to the first transverse acoustic mode in each set of spectra of figure 5.4. Peaks in the acoustic pressure spectra are shown also at the vortex shedding frequency (f_v) and at the higher harmonic ($2f_v$). The corresponding lift amplitude spectra in figures (a) and (b) show only the vortex shedding component. At the onset of acoustic resonance, the acoustic pressure maximum peak is at the resonance frequency and the dominant dynamic lift on the cylinder is at a slightly lower frequency at the natural frequency of vortex shedding, shown by figure 5.4(c). Further increases in the velocity leads to lock-in as shown in figure 5.4(d). Both signals from the load cells and microphone coincide with the same dominate frequency peak at the resonate mode frequency and its higher harmonic. The acoustic pressures at the resonant mode in figure 5.4(a) and (b) are small. The relationships for the lift amplitude due to sound alone predicts lift forces below the broadband response in the corresponding lift amplitude spectra.

Preceding and during acoustic resonance, the dynamic lift amplitude of the center cylinder exhibits major changes. The occurrence of resonance at the first transverse acoustic mode of the duct can be clearly seen in the spectra of both figure 5.1 and figure 5.3 between 60 and 80 m/s. Similar to the acoustic response, the dynamic lift shows a lock-in region where the dynamic lift response is locked-into the acoustic resonant frequency. Vortex shedding becomes highly correlated at the resonant frequency, as is similar with the acoustic response, and is manifested by a decrease in the width of the spectral peaks. This is a typical effect of lock-in as discussed in §2.3.1 by Blevins (1985). The vortex shedding response and lock-in with the resonant frequency, combined with the total dynamic lift forces and those due to the sound field alone are shown by figure 5.5.

The dynamic (acoustic) lift due to an imposed sound field, in the absence of flow, is modeled numerically and validated experimentally using loud speakers to excite a standing acoustic wave in the absence of flow. For the large square tube array,

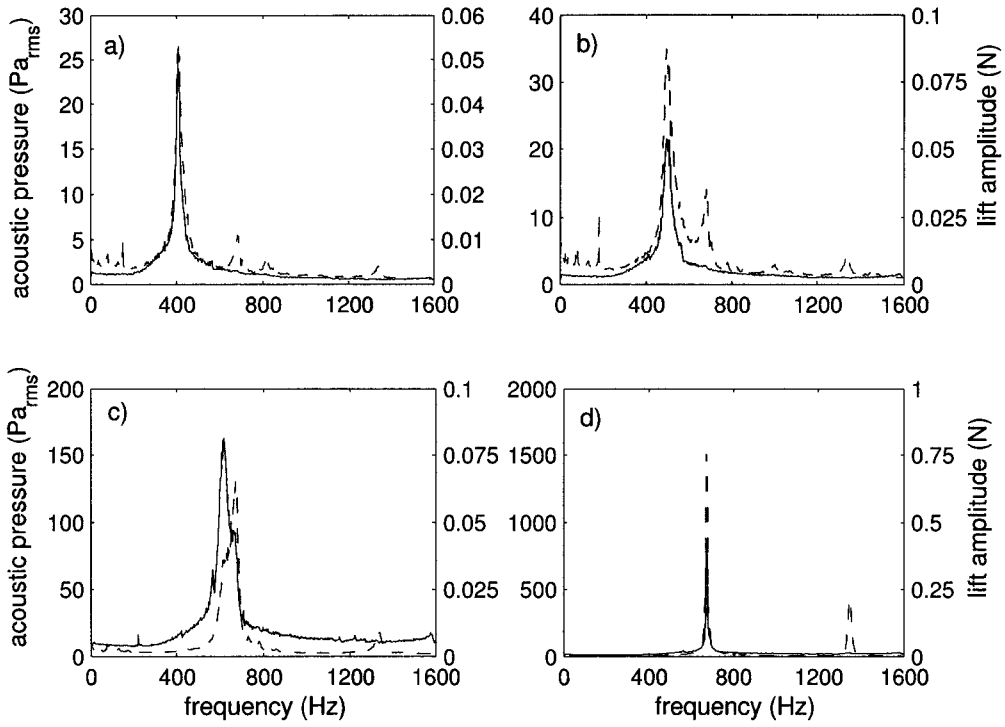

Figure 5.4: Acoustic pressure amplitude spectra, dashed lines, and dynamic lift amplitude spectra, solid lines, for the square array with $P/D = 3.37$, at four gap flow velocities; (a), 39 m/s; (b), 47 m/s; (c), 58 m/s; (d), 69 m/s.

the dynamic lift amplitude per unit length (N/m) is equal to 0.0041 multiplied by the acoustic pressure level in pascals. Both the experimental and numerical results are already discussed in chapter 4. This allows the dynamic (acoustic) lift due to the sound field to be calculated at the acoustic pressures determined during flow-excited acoustic resonance. Thus, for a given sound pressure, such as those shown in figure 5.2, the magnitude of the loading due to sound alone can be determined.

The experimental results of the dynamic lift in the absence of flow are plotted with the total dynamic lift during flow-excited acoustic resonance in figure 5.5(b). It is clear, from figure 5.5(b), that the total dynamic lift amplitude is greater than the predicted lift due to sound alone at the onset of acoustic resonance. However, the total dynamic lift becomes less than the dynamic lift due to sound alone at the

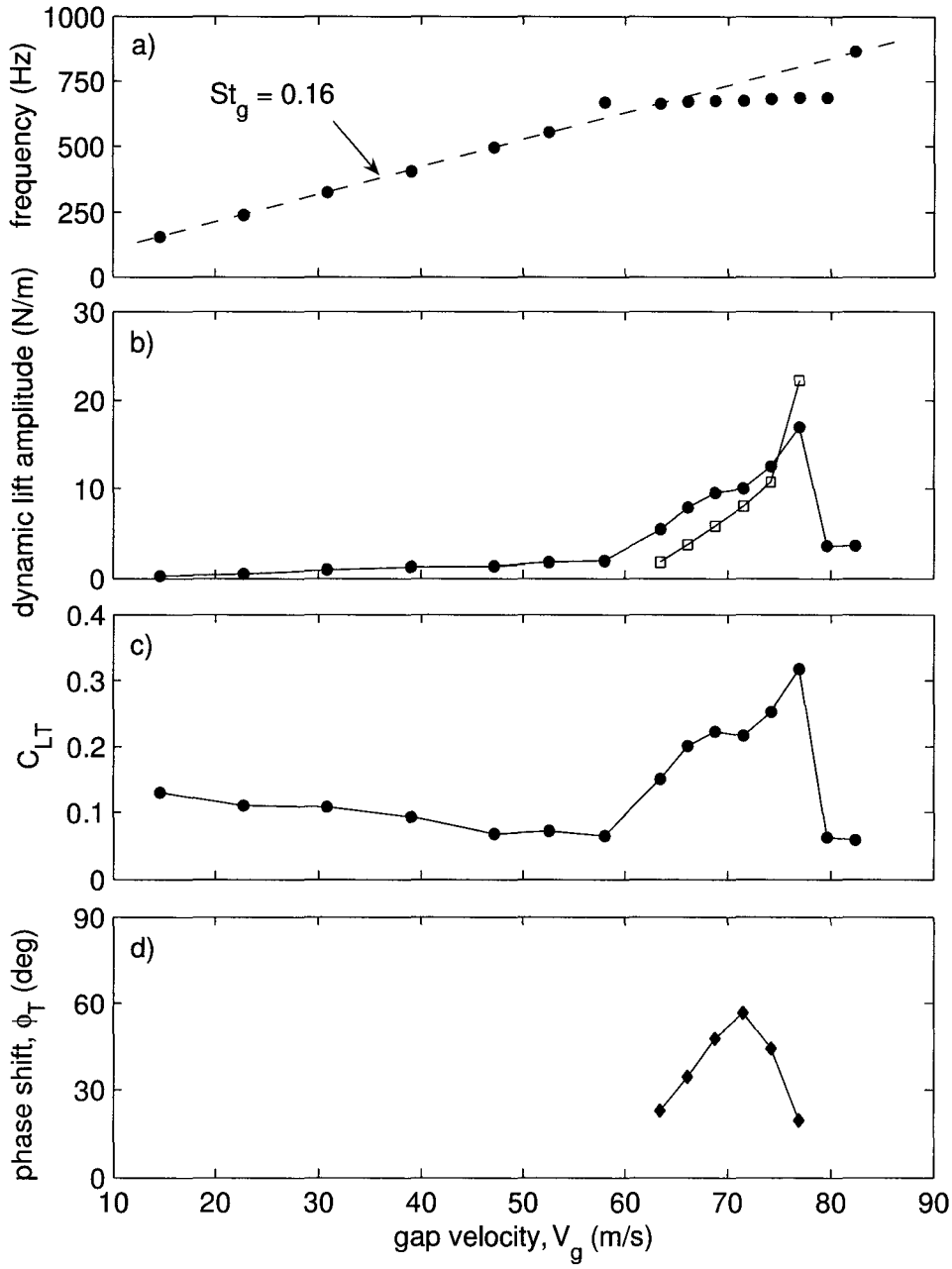

Figure 5.5: Dynamic lift response for a square tube array with $P/D = 3.37$. The frequency response is shown in figure (a). The corresponding total dynamic lift amplitude, •, and lift due to the sound field at resonance, □, at the frequency of vortex shedding is shown in figure (b). The total dynamic lift coefficient, C_{LT}, is shown in figure (c). The phase shift, ϕ_T, between the sound field and total dynamic lift is shown in figure (d).

maximum measured acoustic pressure. The reason for this can be determined from the measured phase shift, ϕ_T, between the sound pressure on the top wall of the test section and the total dynamic lift as explained in the next section.

5.1.2.1 Phase measurements and force decomposition

The phase measurements in figure 5.5(d) are between the sound field, measured at the top of the test section and the dynamic lift measured by the load cells. In the absence of flow, the phase difference between the dynamic lift and sound field is zero. A *negative* signal from the microphone corresponds with a *positive* acoustic pressure, and a *negative* signal from the load cells corresponds with a *downward* force. A vector diagram describing the dynamic lift amplitudes with the relative phases is shown in figure 5.6, for two measurements corresponding to gap velocities of 66 and 76 m/s. Note that the scale of the first diagram is at thirty percent of the second for clarity. These diagrams define the phase shift, ϕ_T, between the total lift vector, L_T, and the sound field dynamic lift vector, L_S. The phase shift, ϕ_A, is between the aerodynamic lift vector, L_A, and the sound field dynamic lift vector, L_S.

By decomposing the total lift into two components, namely the sound component, L_S, and aerodynamic component, L_A, it is possible to show where the dominant sources of lift originate from. Figure 5.7 is a plot of the three lift components determined during acoustic resonance. Only the lift forces during acoustic resonance are decomposed, since the lift force due to sound is very small outside the lock-in range. At the onset of acoustic resonance, the total lift amplitude, L_T, is greater than either of the aerodynamic or sound components. At the beginning of the lock-in range, although there is a phase shift, the lift force induced by the sound field does not oppose the aerodynamic lift force, see figure 5.6(a). The phase shift between the

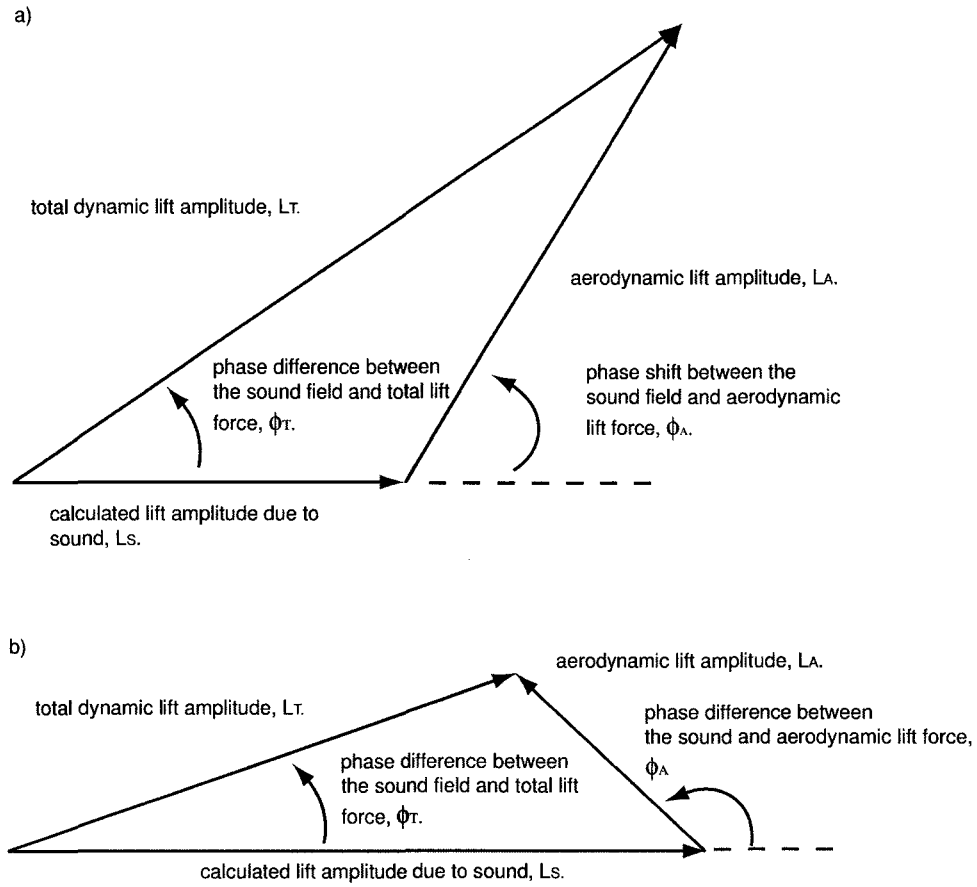

Figure 5.6: Vector representation of the dynamic lift forces during acoustic resonance for the square tube array with $P/D = 3.37$ at $V_g = 66$ m/s, figure (a), $V_g = 76$ m/s, figure (b).

sound and aerodynamic components ranges from 30 to 100 degrees over the lock-in range up to 74 m/s. As the acoustic pressure reaches a maximum value, shown in figure 5.2 at nearly 76 m/s (V_g), the total dynamic lift force becomes smaller than the dynamic lift force predicted from the sound field alone. The phase between the sound field and aerodynamic lift increases to 135 degrees in this case. As shown in figure 5.6(b), the aerodynamic lift opposes the lift induced by the sound field and therefore the total lift force becomes smaller than that predicted by the sound wave.

From figure 5.7(c) an important conclusion which is used for design guidelines discussed at the end of this chapter is that the aerodynamic lift coefficient, C_{LA}, increased by a maximum factor of 3. This factor is calculated, from figure 5.7(c), as the ratio between the maximum aerodynamic lift coefficient during acoustic resonance and the lift coefficient estimated at the same velocity in the absence of acoustic resonance. The lift coefficient before the onset of acoustic resonance is extrapolated to the velocity where the maximum aerodynamic lift coefficient during acoustic resonance occurred, at approximately 72 m/s. Before the onset of acoustic resonance the total dynamic lift coefficient, for Reynolds numbers between 5×10^3 and 6×10^4, varied between 0.13 and 0.08, respectively, which agrees well with the lift coefficients reported by Oengören and Ziada (1992) with similar Reynolds numbers and row depth locations.

5.1.2.2 Phase comparison with the literature

A similar investigation by Mohany and Ziada (2006) on tandem and single cylinders is available for comparison. The test section used in that investigation has the same dimensions. In this case, the lift due to the sound field is found to be very small, on the order of a few percent of the total dynamic lift measured. Therefore, the phase measured between the microphone at the top wall and the dynamic lift on the cylinder is essentially the phase shift between the sound field and the aerodynamic lift on the cylinder. The phase shift, ϕ_A, in the present investigation is obtained from the vector diagrams as illustrated in figure 5.6 and is plotted against the gap velocity in figure 5.7(d). The present phase results, for the large array, are compared with those of Mohany and Ziada (2006) in figure 5.8. The abscissa in this figure is the ratio of the acoustic resonance frequency to the natural excitation frequency, f_a/f_v, which is based on the natural Strouhal number during acoustic resonance, which is deter-

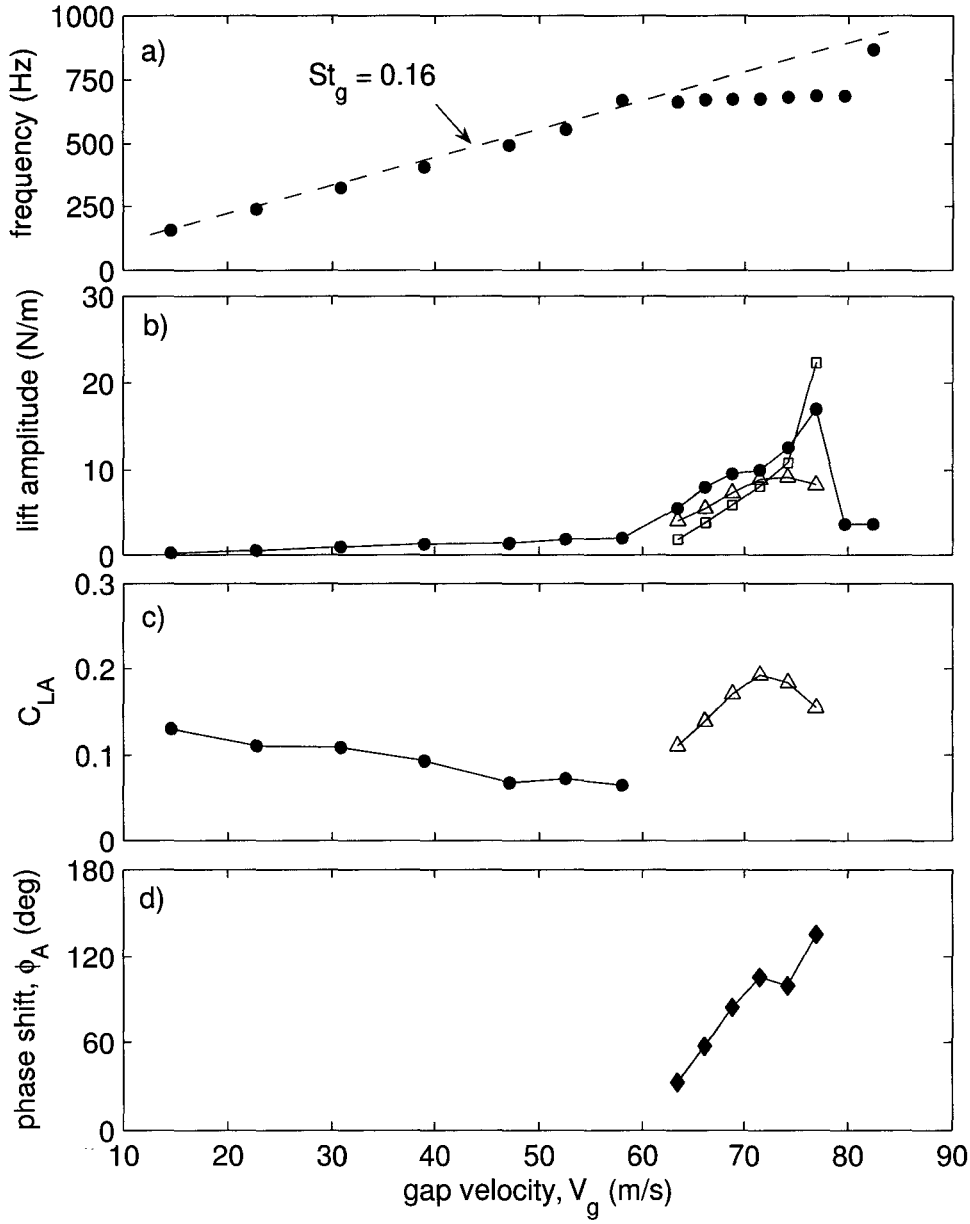

Figure 5.7: Dynamic lift response during acoustic resonance for the large spacing array with $P/D = 3.37$. The frequency response is shown in figure (a). The corresponding total dynamic lift amplitude, •, dynamic lift due to the sound field, □, and the aerodynamic lift, △, is shown in figure (b). The aerodynamic lift coefficient, C_{LA}, is shown in figure (c) using the dynamic lift forces and nomenclature from figure (b). The phase, ϕ_A, between the sound and aerodynamic lift components is shown in figure (d).

mined from figure 5.2(b) to be 0.16. Agreement in the phase shift trend between the present results and those of Mohany and Ziada (2006), shown in figure 5.8, suggests that the flow-acoustic coupling mechanism in widely spaced square arrays is similar to that reported by Mohany and Ziada (2006) for single isolated cylinders. Mohany and Ziada (2006) note that the results obtained for the case of flow-excited acoustic resonance of the single cylinder are similar to the results obtained by Carberry et al. (2001), shown in 2.10 from § 2.3.1.

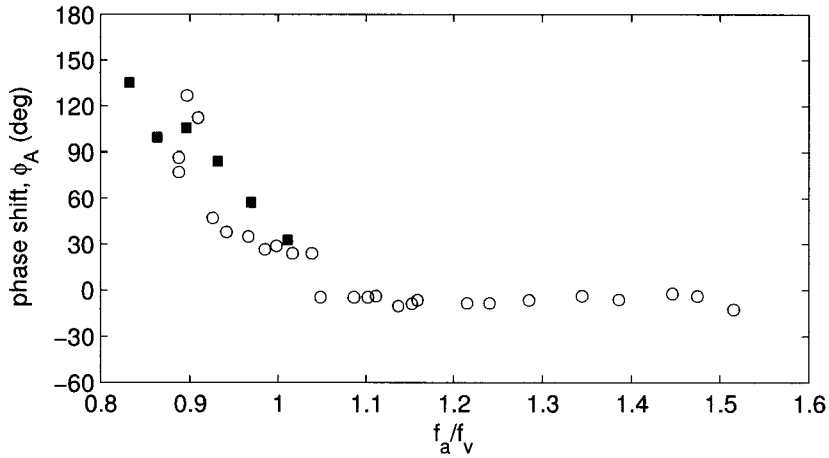

Figure 5.8: Phase shift, ϕ_A, between the aerodynamic lift force and the acoustic pressure field for the present tube array with $P/D = 3.37$, ■, and those of Mohany and Ziada (2006), ○.

5.2 Intermediate spacing square array results

5.2.1 Aeroacoustic response

The aeroacoustic response of the tube array with a spacing ratio of $P/D = 2.18$ is best introduced using a waterfall plot as done previously. In figure 5.9, the *x-axis* defines the frequency of the amplitude spectra (Hz), the *y-axis* defines the flow velocity in terms of gap velocity (m/s), and the *z-axis* is the acoustic pressure level (Pa_{rms}).

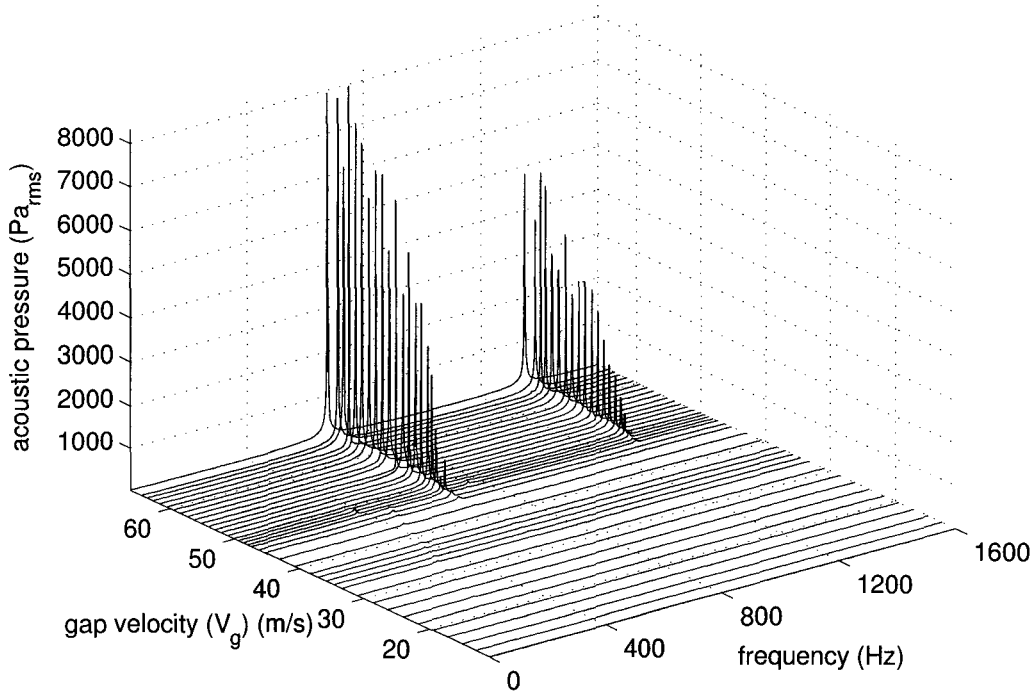

Figure 5.9: Waterfall plot of the aeroacoustic response of the square array with $P/D = 2.18$.

In this experiment, it is evident that the maximum acoustic pressure amplitude is very high, up to nearly 8000 Pa_{rms}, corresponding to 172 dB. Another characteristic

of this array is the modulation in the maximum acoustic pressure amplitude with the flow velocity. It is shown by figure 5.9 that as the velocity is increased, after the onset of acoustic resonance, the general trend is an increase in the acoustic pressures, however, in some cases, the pressure drops. It is not clear what causes the modulation in the pressure response leading to the choppy behavior in the maximum amplitudes. It is conceded that the sound pressures reached are nearly double those of the previous array, and since the amplitudes are highly dependant on the acoustic damping, any disturbances in the flow may effect these measurements. It is also evident from the waterfall plot in figure 5.9 that the lock-in region is very large compared to that shown for the large square array in figure 5.1. It should be noted that the diameter of the tubes for the intermediate array are somewhat larger, with a diameter of 16.67 mm, over the pervious experiments which had a cylinder diameter of 15.08 mm. The effect of a larger tube diameter is discussed by Mohany and Ziada (2005). For tandem cylinders, which exhibit a similar excitation mechanism to that of the intermediate square tube arrays, the cylinder diameter can increase the reattachment length of the shear layer between the cylinders, as well as increase the dynamic head at resonance conditions. For a single cylinder, it is found that during resonance, the associated maximum acoustic pressure increases with the cylinder diameter.

The aeroacoustic response for the square tube array with $P/D = 2.18$ is shown by figure 5.10. A single Strouhal number of 0.164 is identified before the onset of acoustic resonance. This is consistent with the literature available on the topic, such as the results of Ziada (2006) shown by figure 2.16 in §2.4.1. As the frequency of the flow periodicity increases with the flow velocity, acoustic resonance occurs before coincidence of the natural Strouhal number with the acoustic mode frequency. In the case of the large square array, with $P/D = 3.37$, the resonance range seemed to be excited by the natural Strouhal number. Figure 5.2(a) shows that as the frequency

increases, it reaches the acoustic mode frequency, and then locks into this frequency for further flow velocity increases. This is essentially different than the behavior shown in figure 5.10(b) for the intermediate square tube array. This response is, however, observed in the literature, such as in the results of Ziada and Oengören (1990) and Oengören and Ziada (1992b). Oengören and Ziada (1992b) demonstrate that the flow instability causing acoustic resonances is basically different from the symmetrical jet instability that causes constant Strouhal number vorticity shedding in the absence of acoustic resonance. Acoustic resonance occurs due to coupling between the resonant mode and the unstable shear layers formed between the tubes. The shear-layer mode, however, is suppressed at off-resonance conditions.

5.2.2 Aeroacoustic response, comparison with the literature

The experimental results of Ziada and Oengören (1990) are used by Mohany (2006) to explain the dual resonance phenomena observed in the intermediate spaced tandem cylinders. Tandem cylinders can produce similar acoustic resonance characteristics as observed in the inline and square tube arrays, for similar longitudinal spacing. The results of Mohany (2006) for tandem cylinders with $L/D = 2$ and those of Ziada and Oengören (1990) with $X_L/X_T = 2.1/2.5$, are overlaid with the present results with $P/D = 2.18$ in figure 5.11. In order to compare the results with different acoustic mode frequencies, the frequencies are normalized by the acoustic mode frequency in each of the experiments, denoted by f_a. Also, to properly overlay the results, the velocity is presented in terms of the reduced velocity, discussed in some detail in §2.1.1. Essentially, the reduced velocity scales the gap velocity by the acoustic resonance frequency and corresponding cylinder diameter.

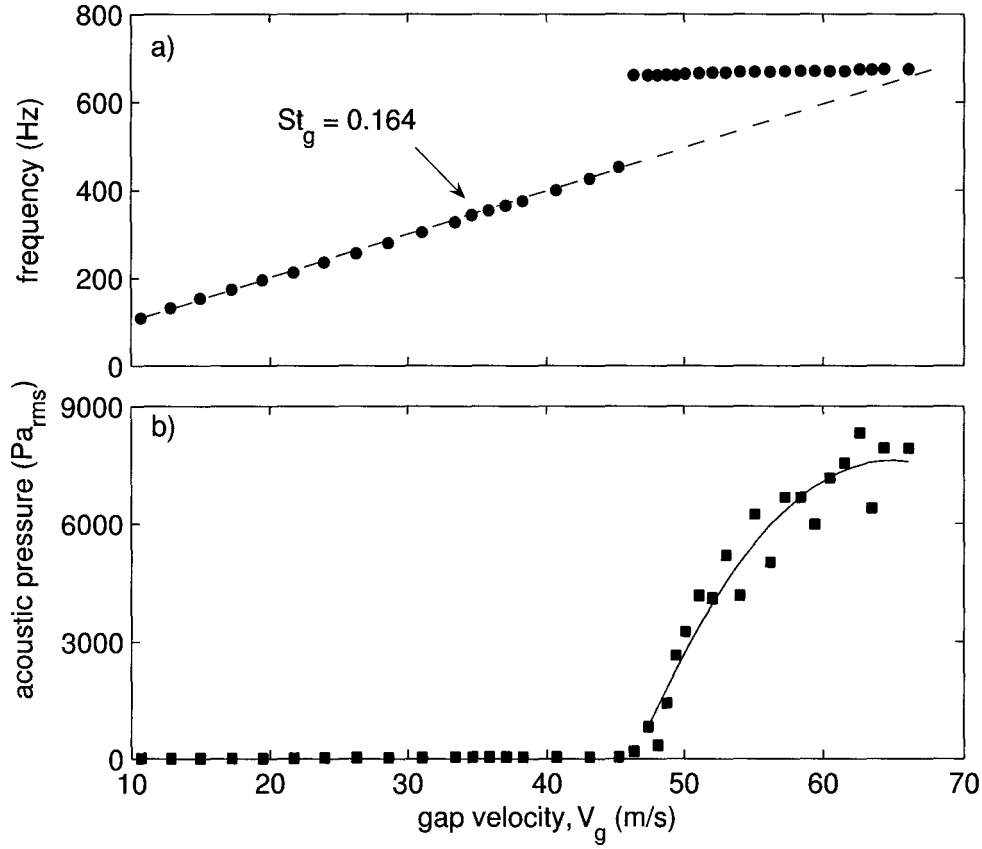

Figure 5.10: Aeroacoustic response for a square tube array with $P/D = 2.18$. Figure (a) shows the frequency response, •; figure (b) shows the acoustic pressure, ■, at the frequency of vortex shedding and with respect to the gap velocity. The solid line in figure (b) shows the general trend in the data.

Figure 5.11 shows that the results of Ziada and Oengören (1990) and Mohany and Ziada (2007) compare well with the present results. The Strouhal number is 0.164 for the present array with $P/D = 2.18$, whereas it is slightly lower at approximately 0.15 for the inline and tandem cylinders. It should be noted that, in these cases, the cylinder diameters, Reynolds numbers, and dynamic heads are different, however the pre-coincidence acoustic resonance is observed in all the three cases. Additionally, the aeroacoustic response depicted in figure 5.11 shows that the sound pressure level during resonance is comparable between the tube arrays. For the tandem cylinders,

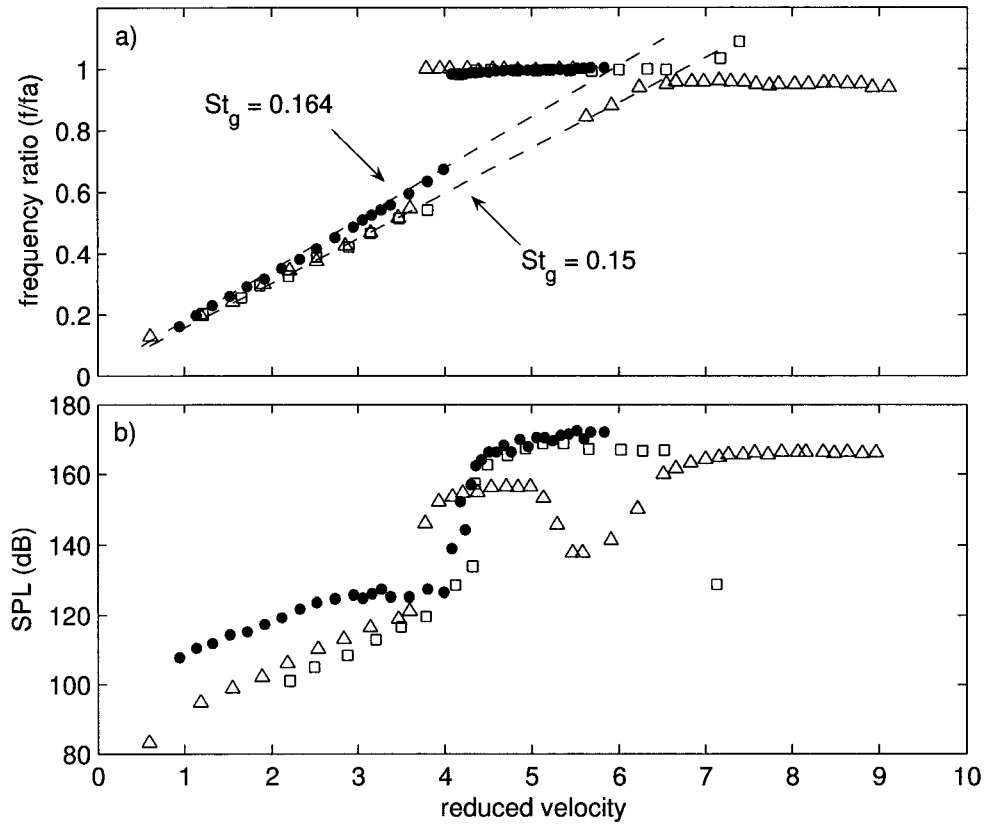

Figure 5.11: Comparison of the frequency response, figure (a), and the acoustic pressure response, figure (b) between the present results and those from the literature. The two figures show the results of a square tube array with $P/D = 2.18$, •, with tandem cylinders with $L/D = 2$, △, (Mohany and Ziada 2007), and an inline tube array with $X_L/X_T = 2.1/2.5$, □, (Ziada and Oengören 1990).

the spacing ratio is slightly smaller than that of the square array, and therefore the results do not align as well.

5.2.3 Dynamic lift response

The dynamic lift on the central cylinder for the intermediate array is measured over the total range of gap velocities that could be achieved with the experimental setup, at both non-resonance and resonance conditions. The waterfall plot shown by

figure 5.12 shows spectra from one of the load cells. The *x-axis* defines the frequency of the amplitude spectra (Hz), the *y-axis* defines the flow velocity in terms of gap velocity (m/s), and the *z-axis* is the amplitude of the dynamic lift (N). Before the onset of acoustic resonance, a linear increase of the Strouhal periodicity is visible, corresponding to that observed in the aeroacoustic response of figure 5.10.

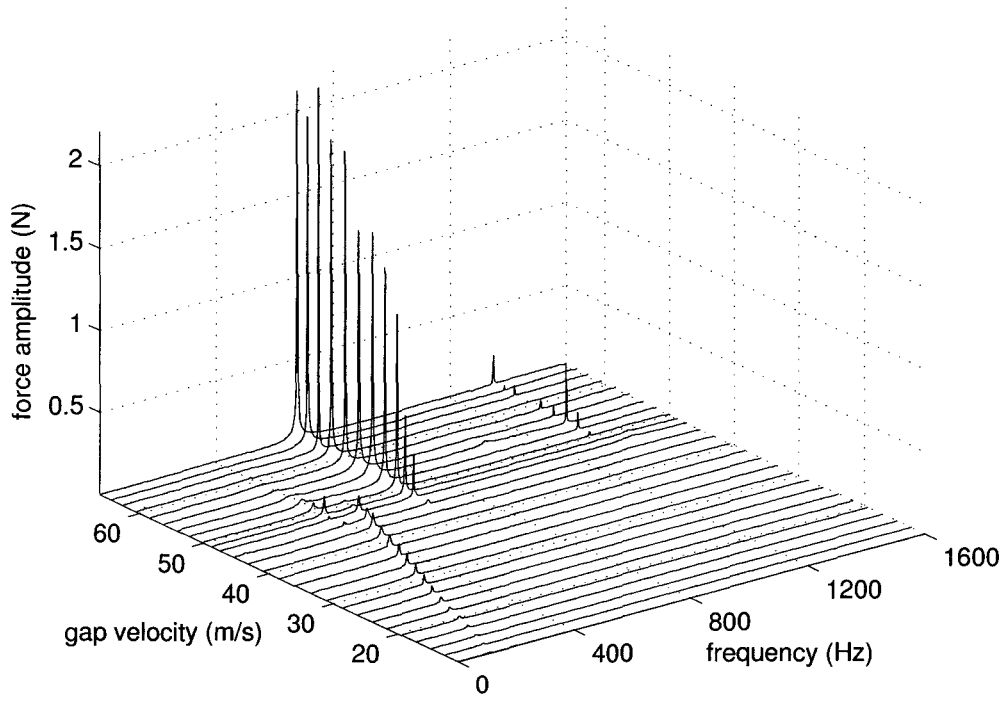

Figure 5.12: Waterfall plot of the dynamic lift amplitude spectra from one load cell in a square tube array with $P/D = 2.18$.

Figure 5.13 shows four amplitude spectra from a single load cell overlaid with the acoustic response measured by the microphone. In figure 5.13(a), at a gap velocity of 21.7 m/s, the vortex shedding frequency is observed in both corresponding spectra. The microphone signal exhibits both the vortex shedding frequency and a higher harmonic of that frequency. This is typical of aeroacoustics testing done in air. The third spectral peak visible in this spectrum is the natural acoustic mode response

of the duct, excited by broadband turbulence of the interstitial flow, at around 672 Hz. As the gap velocity is increases, to 33.4 m/s, shown in figure 5.13(b), the amplitude at the first transverse acoustic mode frequency increases in magnitude. It is, however, not visible in the load measurements. Similar to the large spacing array, the associated sound pressure level at the acoustic mode frequency is low, and therefore the dynamic lift response is very weak, and is not visible in the lift amplitude spectra. At a frequency of approximately 1300 Hz, the second transverse acoustic mode is visible. The mode shape is shown in figure 5.14(c) from the numerical simulation. The frequency prediction by the numerical simulation is in good agreement with that observed in the spectrum from figure 5.13(c). At 45.2 m/s, shown by figure 5.13(c), at the onset of acoustic resonance, both the microphone and dynamic lift measurements show spectral peaks at the natural vortex shedding, and at the first and second transverse acoustic mode frequencies. There is also an additional peak in both the lift amplitude spectrum and the acoustic pressure spectrum just below 400 Hz. Using the numerical simulation, a longitudinal mode at 390 Hz is present which may be the source of this spectral peak, shown in figure 5.14(c). At 54.1 m/s, shown by figure 5.13(d), lock-in is established and both signals exhibit a narrow band peak at the acoustic mode frequency of approximately 672 Hz. For the acoustic pressure response, a higher harmonic of the first mode frequency is observed at $2f_a$, where f_a is the frequency of the first transverse acoustic mode.

The dynamic lift, in terms of peak amplitudes extracted from the amplitude spectra of the load cells, is used to produce the lift amplitude response shown in figure 5.15. The frequency response from figure 5.10 is re-plotted in figure 5.15(a) to compare the dynamic lift response with the frequency response. The frequency of the amplitude peaks corresponds to the frequency value given in figure 5.15(a). A similar choppy behavior is observed in the dynamic lift plotted figure 5.15(b), to that observed in the

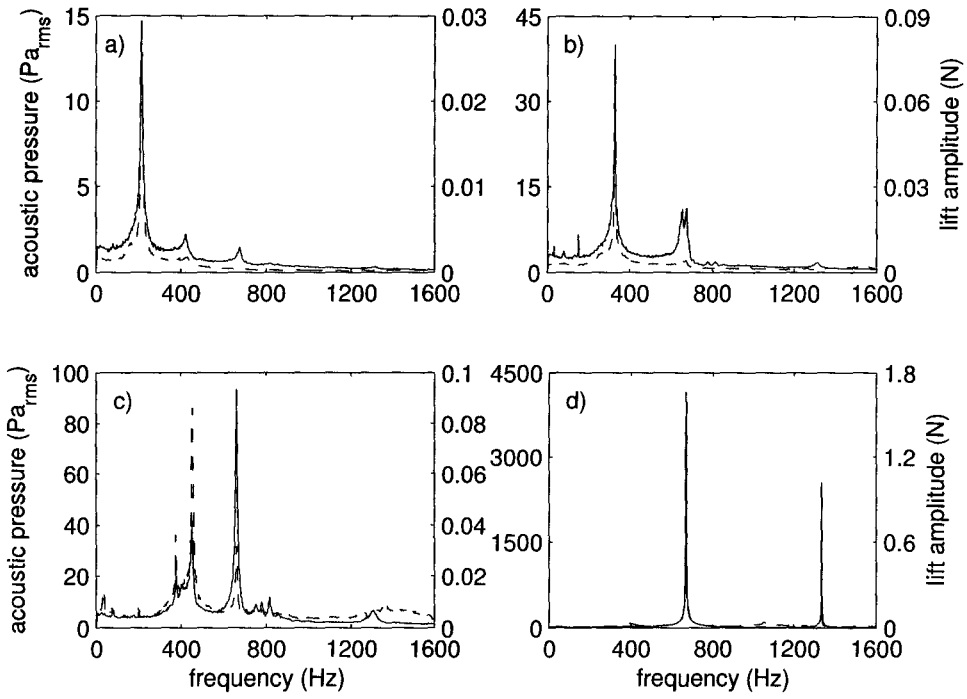

Figure 5.13: Acoustic pressure amplitude spectra, solid lines, and dynamic lift amplitude spectra, dashed lines, at four gap velocities for the square array with $P/D = 2.18$; (a), 21.7 m/s; (b), 33.4 m/s; (c), 45.2 m/s; (d), 54.1 m/s.

acoustic pressures shown in figure 5.10. The acoustic pressures in the lock-in region from figure 5.10(b) are used with the experimental results from chapter 4 to determine the dynamic lift amplitude due to sound alone and are plotted with the total dynamic lift in figure 5.15(b). In this case, the total measured dynamic lift on the cylinder is always greater than that induced by the sound pressure field alone. The total lift force is presented as a dynamic lift coefficient in figure 5.15(c). Oengören and Ziada (1992) report lift coefficients of approximately 0.1 for the intermediate square array with $P/D = 1.95$, which agree well with the present results before the onset of acoustic resonance. During acoustic resonance, the lift coefficient, C_{LT}, increases by an order of magnitude.

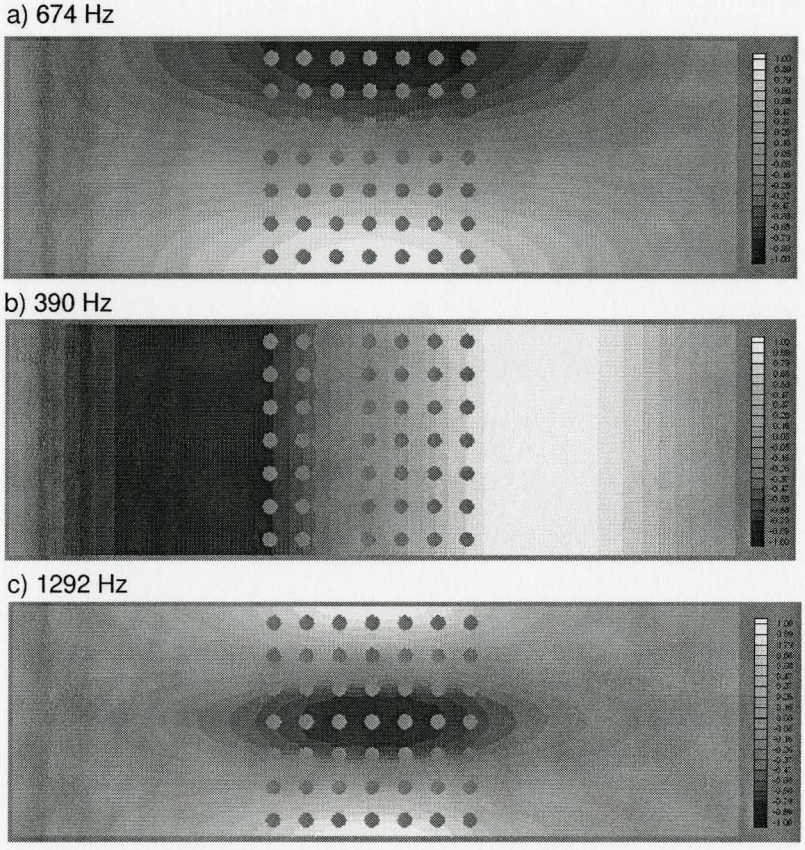

Figure 5.14: Acoustic mode shape of the first transverse mode, figure (a) at 674 Hz, a longitudinal mode, figure (b) at 390 Hz, and the second transverse acoustic mode, figure (c) at 1292 Hz.

5.2.3.1 Phase measurements

Measurements of the phase shown in figure 5.15 (d) confirms that the phase difference between the sound field and the total lift force is small, it ranges between only ± 5 degrees. This indicates that the dynamic sound and aerodynamic lift forces are acting nearly in-phase to generate the total dynamic lift measured. For this reason, the total dynamic lift is nearly the sum of the aerodynamic lift and the dynamic lift forces generated due to the sound field.

Measurement of the phase between the sound field and the total dynamic lift force make it possible to determine the phase between the aerodynamic and sound field

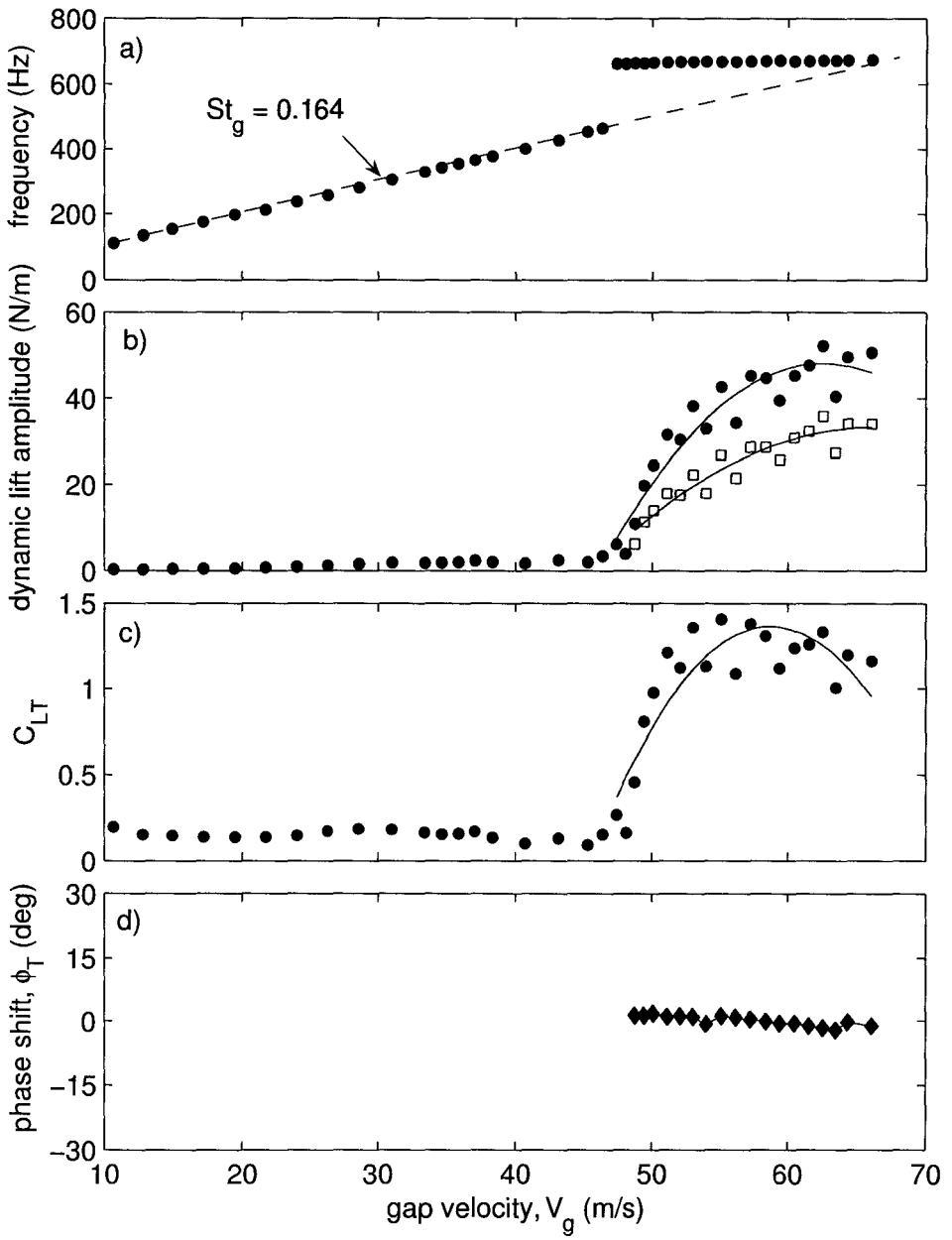

Figure 5.15: Dynamic lift response for a square tube array with $P/D = 2.18$. The frequency response is shown in figure (a). The corresponding total dynamic lift amplitude, •, and lift due to the sound field at resonance, □, at the frequency of vortex shedding is shown in figure (b), with solid lines representing the general trend in the data. The total dynamic lift coefficient, C_{LT}, is shown in figure (c). The phase shift, ϕ_T, between the sound field and total dynamic lift is shown in figure (d).

induced lift, and also makes it possible to calculate the magnitude of the aerodynamic lift. A vector plot of the calculated aerodynamic lift and phase is shown in figure 5.16. This is a typical result, showing the effect of a small phase angle. The main characteristic emphasized is the small phase angle between the sound field dynamic lift and the aerodynamic lift, which leads the total lift measured directly by the load cells to be greater in magnitude than either of the other two components. With such a small phase angle, when the magnitudes of the vectors are directly summed, the resultant exhibits little difference, less than a few percent, from that calculated from the vectors.

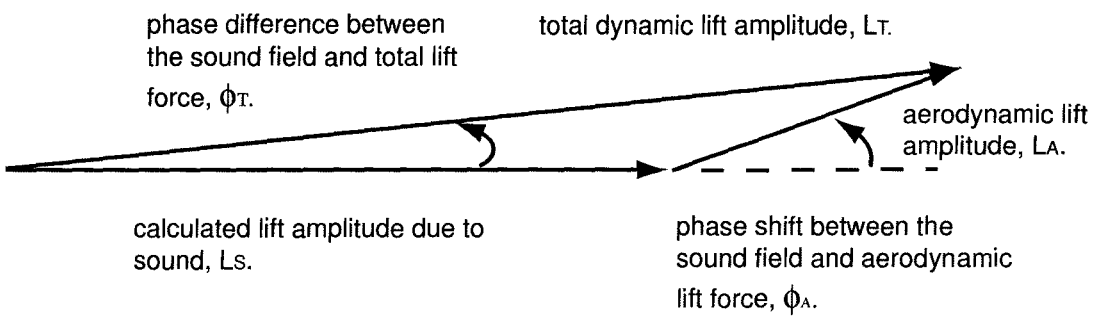

Figure 5.16: Vector representation of the dynamic lift during acoustic resonance for a typical result from the square array with $P/D = 2.18$.

The total dynamic lift force is decomposed into aerodynamic and sound induced lift components, together with the phase shift, ϕ_A, as shown by figure 5.17. This emphasizes the point made previously of the nearly additive quality of the magnitudes of the components with small phase differences. The lift coefficient, C_{LA}, in figure 5.17(c), is determined from the total dynamic lift before the onset of acoustic resonance. During acoustic resonance, the lift coefficient is determined from the aerodynamic lift, L_A. Figure 5.17(c) is used to determined the ratio of enhancement of the aerodynamic lift coefficient during acoustic resonance. The ratio between the en-

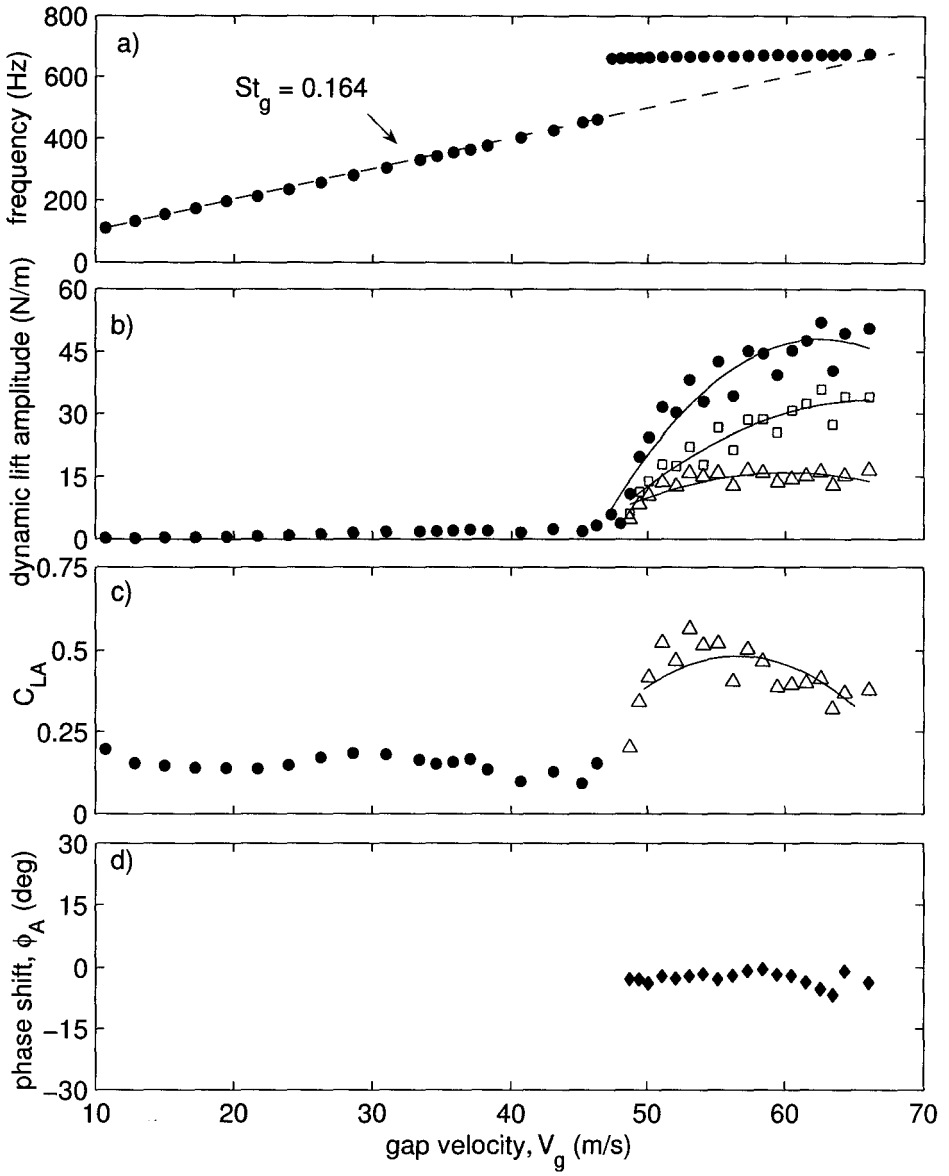

Figure 5.17: Dynamic lift response during acoustic resonance for the intermediate spacing array with $P/D = 2.18$. The frequency response is shown in figure (a). The corresponding total dynamic lift amplitude, •, dynamic lift due to the sound field, □, and the aerodynamic lift, △, is shown in figure (b). The aerodynamic lift coefficient, C_{LA}, is shown in figure (c) using the dynamic lift forces and nomenclature from figure (b). The phase shift, ϕ_A, between the sound and aerodynamic lift component is shown in figure (d).

hanced aerodynamic lift coefficient, and the un-enhanced aerodynamic lift coefficient at the same corresponding velocity (which is extrapolated from the lift coefficients measured before the onset of acoustic resonance), is a factor of 6.

It is of interest to review again the plot of the phase difference with respect to the frequency ratio, f_a/f_v. For the present case, this is shown along with the single cylinder results of Mohany and Ziada (2006) in figure 5.18. The results for the present intermediate spacing ratio are distinctly different from those of the large spacing ratio, plotted with the single cylinder results of Mohany and Ziada (2006) in figure 5.8. For the large tube array, resonance is excited by classical Strouhal periodicity. Similar to the results of Carberry et al. (2001), it is found that when the driving frequency and the natural frequency are near, the phase between the dynamic lift forces becomes large. In the present case, the observed acoustic resonance occurs at a frequency much higher than the vortex shedding frequency, referred to as the pre-coincidence resonance range. Thus the value of f_a/f_v is always greater than 1, and predicts a small phase difference. The present phase results agree well with the results of Mohany and Ziada (2006) in figure 5.18.

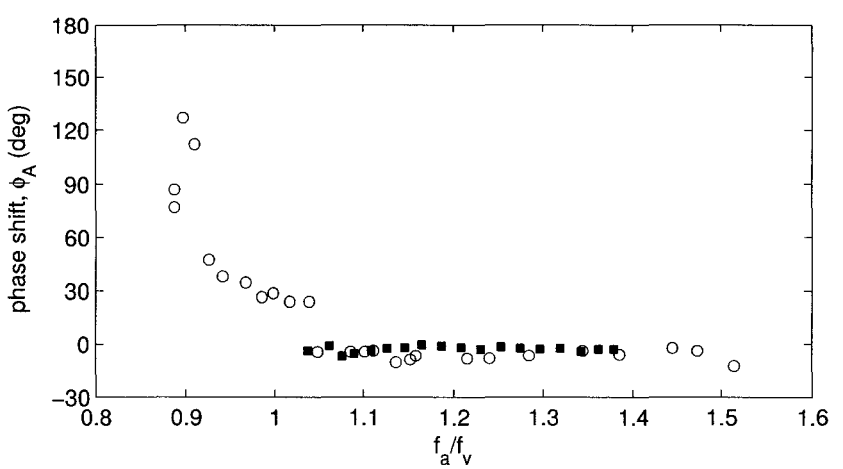

Figure 5.18: Phase shift, ϕ_A, between the aerodynamic lift force and the acoustic pressure field for the square tube array with $P/D = 2.18$, ■, and those of Mohany and Ziada (2006), ○.

5.3 Small spacing array results

5.3.1 Aeroacoustic response

The aeroacoustic response of the small spacing tube array with a spacing ratio of $P/D = 1.58$ is shown in the waterfall plot of figure 5.19. The coordinate system is defined similarly to the large and intermediate spacing ratios. For the small spacing array, the lock-in region occurs at the higher range of the flow velocities possible with this array. It is not possible to investigate further into the lock-in region for this particular array due to limits in the achievable flow velocity. Figure 5.19 clearly shows a linear increase of the vortex shedding component for gap velocities below 40 m/s between 600 and 1200 Hz in the spectra. During the acoustic resonance range observed in the present experiment, the maximum acoustic sound pressure reached just over 1200 Pa_{rms}. In the range of 1300 Hz, two frequency peaks are visible. One is a higher harmonic of the first mode, and the other is the second transverse mode. This is discussed in further detail in §5.3.3.

The frequency and acoustic pressure response is found by examining the spectra presented in figure 5.19; extracting the vortex shedding frequencies and corresponding acoustic pressures. All the spectra that are plotted in figure 5.19 exhibit a strong broadband turbulence, characteristic of a small spacing tube array. Thus, it is difficult to extract both the vortex shedding frequencies and the corresponding pressures. For this reason, only the acoustic pressure associated with the first mode resonance frequency is presented in the system response plot. As shown in figure 5.20, vortex shedding is observed only at high frequencies. The Strouhal number for the linear region is approximately 0.40. This value is within the range presented in the literature. The empirical relationships by Zukauskas and Katinas (1980) predicts $St_g = 0.29$, and

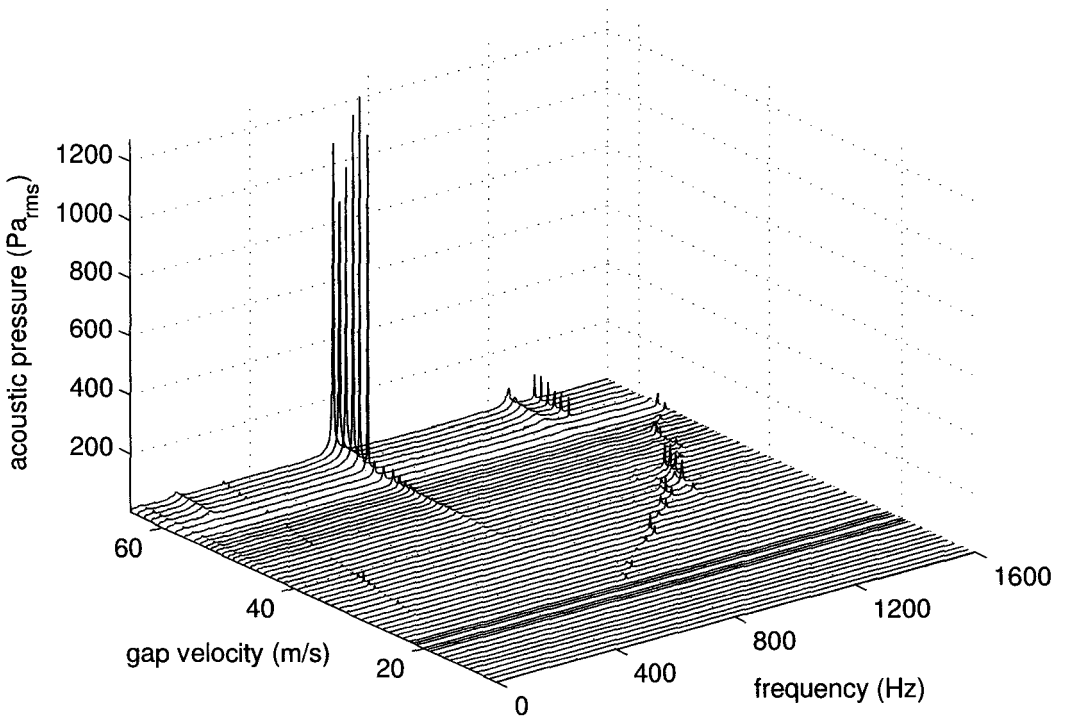

Figure 5.19: Waterfall plot of the aeroacoustic response for the small spacing square array with $P/D = 1.58$.

that of Owen (1965) predicts $St_g = 0.31$. In addition, the data compiled by Weaver and Yeung (1984) in figure 2.16(a) show that a Strouhal number of 0.40 is well within the data compiled from various authors.

For small tube arrays, as discussed in much of the literature, there is an effect of the row depth. Ziada et al. (1989) concludes that in small arrays, at non-resonance flow conditions, vortex shedding is observed primarily in the first tube rows, and is disrupted downstream as the flow becomes highly turbulent. Thus, at lower Reynolds numbers, the observed vortex shedding frequency is often different than that observed at higher Reynolds numbers. From the flow visualizations, it is shown that indeed the vortices are present, but of little energy. Since the measurements of the vortex

shedding frequency in the present experiment were only indirectly determined from the microphone, or from direct measurements on the centrally located tube, it is difficult to discern the vortex shedding frequencies. Another important conclusion from Ziada et al. (1989) is that the flow periodicity causing acoustic resonance is typically not observed at off resonance conditions. The response in figure 5.20(a) shows the absence of a lower frequency component of vortex shedding before the onset of acoustic resonance. When coincidence occurred between the vortex shedding frequency component, corresponding with $St_g = 0.40$, and the acoustic resonance frequency, it locked into the resonance frequency over a small range of flow velocities, however only weakly excited the resonance mode. The acoustic pressure achieved during this coincidence, shown in figure 5.20(b) at 20 m/s, is very small.

Increasing the flow velocity led to a range of Strouhal numbers during lock-in between 0.2 and 0.15 at the maximum velocity achieved by the wind tunnel. Although much of the literature shows dominant Strouhal numbers in the range of 0.3 and above, some authors have identified lower Strouhal numbers, see for example the Strouhal number data by Baylac et al. (1973) which includes Strouhal numbers in the range of 0.11 for small spacing ratios. Ziada (2006) observed similar Strouhal numbers in this range as shown in figure 2.16 from §2.4.1. Weaver et al. (1987) observed in their experiments that the Strouhal numbers identified were not present at all Reynolds numbers, and at lower Reynolds numbers, only an intermediate Strouhal number was identified. Oengören and Ziada (1992b) identify a Strouhal number of 0.15 for the line array with $X_L/X_T = 1.75/2.25$. In the latter case, the Reynolds number is much lower than in the present investigation. In the present study, however, the aim to investigate the dynamic lift and the effects of sound.

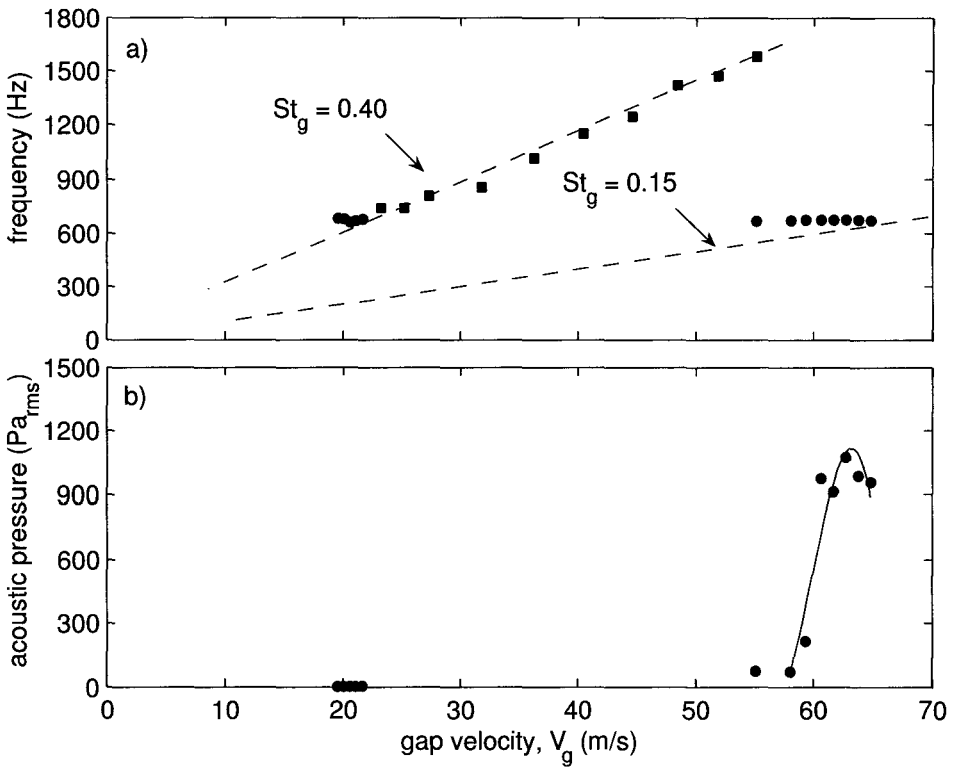

Figure 5.20: Aeroacoustic response for a square tube array with $P/D = 1.58$. Figure (a) shows the frequency response due to a lower Strouhal number, •, and a higher Strouhal number, ■. Figure (b) shows the acoustic pressure response at the frequency of the first acoustic mode. The dashed line in figure (a) shows the frequency trend for an assumed Strouhal number of 0.15 from the results of an inline array of Oengören and Ziada (1992b) for $X_L/X_T = 1.75/2.25$.

5.3.2 Aeroacoustic response, comparison with the literature

The current aeroacoustic response is compared with observations available in the literature with similar geometry. Directly relevant to the present results are those of Mohany and Ziada (2005) and those of Oengören and Ziada (1992b). The results of Mohany and Ziada (2005) for tandem cylinders with $L/D = 1.5$ are considered, since this geometry is close to the present square array geometry with $P/D = 1.58$. Also, the tandem cylinders showed good agreement with the intermediate spacing

square array. Oengören and Ziada (1992b) present results for an inline tube array with spacing ratios of $X_L/X_T = 1.75/2.25$, which has a *reasonably* close stream-wise spacing to the present square array with $P/D = 1.58$. To accomplish this comparison, it is necessary to present the results in dimensionless form. Thus, the frequencies are normalized by the excited acoustic mode frequency, f_a, and the velocities are presented in terms of the reduced velocities as defined in §2.1.1.

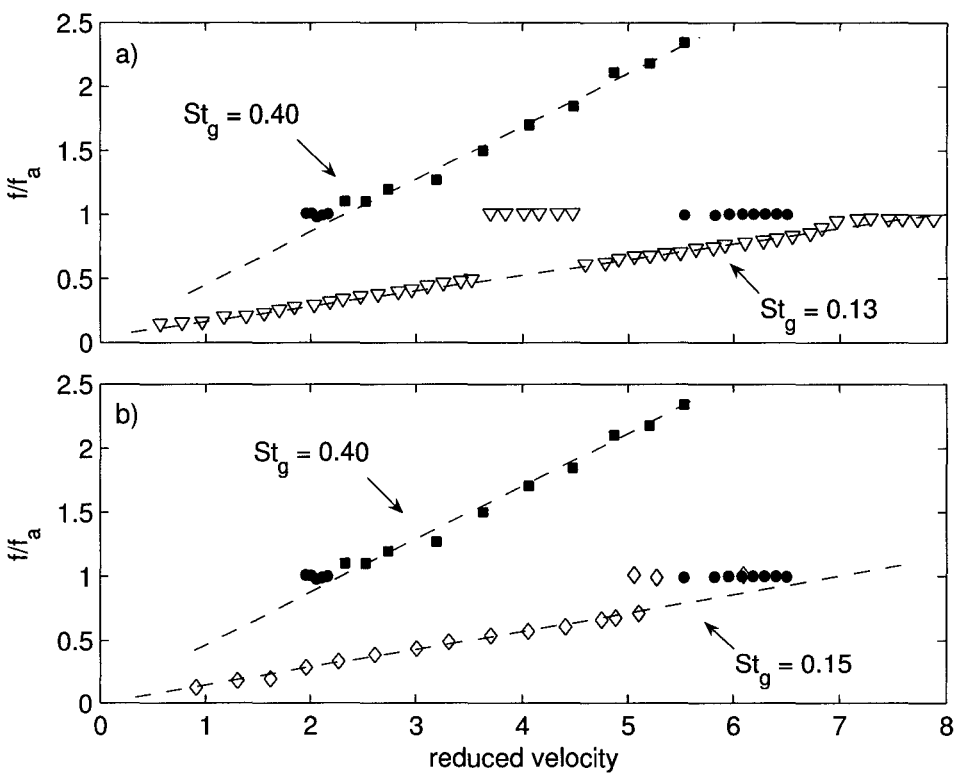

Figure 5.21: Frequency response for a square tube array with $P/D = 1.58$ in comparison with results from the literature. Figure (a) shows the results for a square array with $P/D = 1.58$, •, ■, as defined in figure 5.20; two tandem cylinders, $L/D = 1.5$, ▽, Mohany and Ziada (2005). Figure (b) shows the results of the square array with $P/D = 1.58$, as defined in figure (a) with inline array, ◇, by Oengören and Ziada (1992b) for $X_L/X_T = 1.75/2.25$.

The tandem cylinder results exhibit a pre-coincidence resonance range, as shown in figure 5.21(a), much earlier than that for the present results of the small spacing array. The coincidence resonance range occurs at a higher reduced velocity than the

resonance observed in the present results. For this reason it is suspected that the Strouhal numbers of the small spacing tandem cylinders are removed from those of the small spacing square tube array. The inline array, with $X_L/X_T = 1.75/2.25$, exhibited a Strouhal number of 0.15, slightly higher than that observed by Baylac et al. (1973). It should be noted that this is for a larger spacing than for the small spacing array studied in this section, however, the longitudinal spacing is only on the order of 10% larger. Comparison of the present results with those of Oengören and Ziada (1992b) shows good agreement in the general trend in the data wherein acoustic resonance is excited before coincidence between the natural Strouhal number and the acoustic mode frequency. This indicates that the mechanism of the acoustic resonance is the same as that of the inline array by Oengören and Ziada (1992b). It is concluded that this is indeed a pre-coincidence acoustic resonance, similar to the intermediate case. This conclusion is further validated by the flat phase shift behavior shown later in figure 5.26, typical of pre-coincidence resonance characteristics.

5.3.3 Dynamic lift response

A waterfall plot of the amplitude spectra of the dynamic lift for the total range of flow velocities studied is presented in figure 5.22.

From this figure, it is clearly shown that the dynamic lift of the instrumented central cylinder becomes very large at the onset of acoustic resonance. With small tube spacing ratios, the energy of the vortices shed is expected to be very low, especially for the interior tubes (Ziada et al. 1989). The closely packed tubes produce a highly turbulent flow causing a broadband turbulent response reflected in the turbulence intensity of the interstitial flow. The broadband turbulent response is evident in the spectra presented in figure 5.23. Four pairs of spectra are shown, displaying the acous-

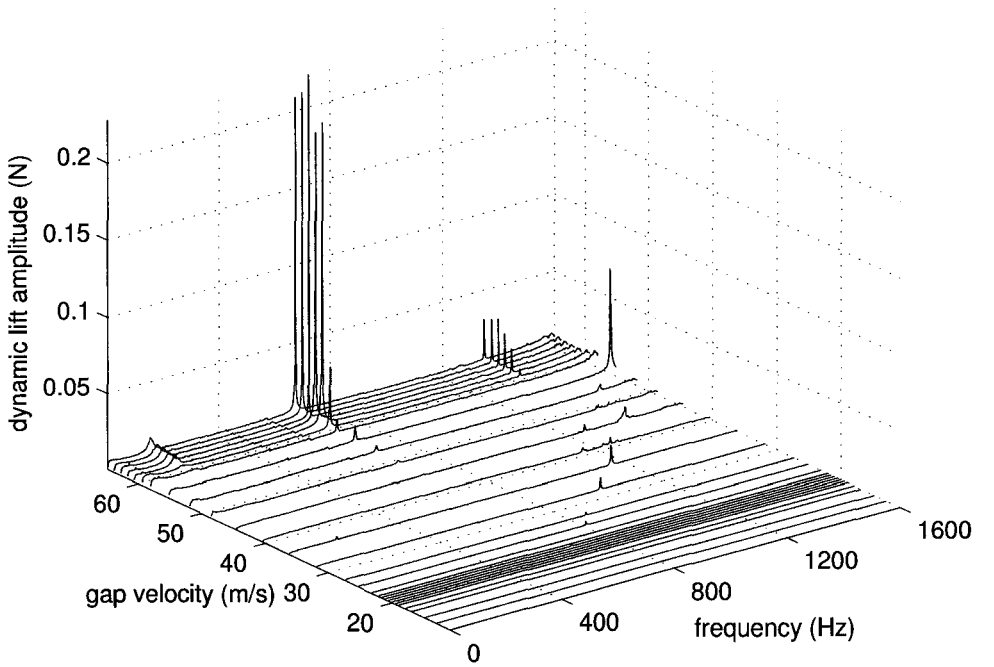

Figure 5.22: Waterfall plot of the dynamic load amplitude spectra from one load cell for a square tube array with $P/D = 1.58$.

tic pressure and dynamic lift amplitude spectra for a single load cell. At lower flow velocities, during off resonance conditions, the response is indeed broadband. As the velocity is increased, there is a weak excitation of the first transverse acoustic mode, around 670 Hz, also a small peak corresponding to the second transverse acoustic mode can be identified at 1280 Hz from figure 5.23(b). The first transverse acoustic mode shape is shown in figure 5.24(b), the second transverse acoustic mode shape is shown in figure 5.24(c). At higher flow velocities, vortex shedding can be identified in both the dynamic lift amplitude spectra and acoustic response shown in figure 5.23(c) at approximately 1150 Hz. In these spectra, a low frequency component slightly less than 200 Hz is observed. This is likely due to a low frequency longitudinal mode. One such mode is identified in figure 5.24(a). Since the simulated domain does not account for the parabolic contraction and the diffuser at the exit, this mode could

exist at a lower frequency than calculated for the current geometry. A peak in the spectra of figure 5.23(c) at 1280 Hz also exists, which appears to originate from the second transverse acoustic mode. When acoustic resonance occurs, there is a narrow band peak with a high amplitude for both spectra in figure 5.23(d) and also a peak at $2f_a$, a higher harmonic. Consistent with these results are the findings of Ziada et al. (1989), who reported that during resonance, the structure of the flow changes, and using flow visualization, strong vortex shedding is observed throughout the tube array, unlike the off resonance case. One last frequency component is observed near 1550 Hz at a gap velocity of approximately 50 m/s in figures 5.19 and 5.22. The numerical simulation predicts an acoustic mode at 1534 Hz, that may be responsible for this spectral peak. This acoustic mode is shown in figure 5.24(d).

5.3.3.1 Dynamic lift force decomposition

The total dynamic lift force measured by the load cells is decomposed into the aerodynamic lift force and the lift force induced by the acoustic standing wave. The latter is determined from the acoustic sound pressure levels shown in figure 5.20. By means of the phase measurements between the acoustic pressure field and the total dynamic lift, it is possible to extract the aerodynamic lift as well as the phase between the aerodynamic lift and the sound field as explained previously in §5.1.2.1 and §5.2.3.1.

Figure 5.25 shows the final results for the small square tube array. The frequency response in figure 5.25(a) is the same as that presented in figure 5.20, and is re-plotted to define the frequency at which the points in parts (b), (c) and (d) are measured. Figure 5.25(b) shows that the total dynamic lift force is greater than either the lift force induced by the sound field, and that of the aerodynamic lift component. The

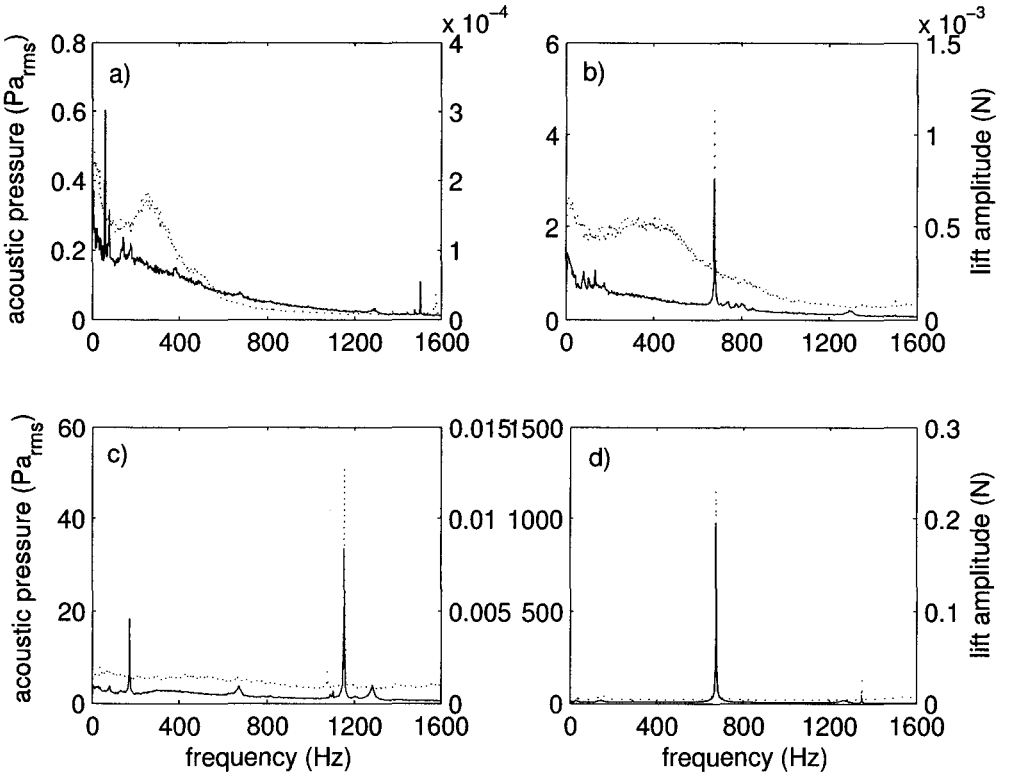

Figure 5.23: Acoustic pressure amplitude spectra, solid lines, and dynamic lift amplitude spectra, dashed lines, at four gap velocities for the square array with $P/D = 1.58$; (a), 13.1 m/s; (b), 21.6 m/s; (c), 36.2 m/s; (d), 60.6 m/s; based on the gap velocity.

total dynamic lift force, similar to the intermediate spacing ratio, can be computed by summing the force vectors induced by the sound field and the aerodynamic lift force. The phase between the total dynamic lift force and sound field, ϕ_T, is used to compute the phase difference between the aerodynamic lift and the sound field, ϕ_A. The calculated phase, ϕ_A, is shown by figure 5.25(d). Comparison of the phase with the results of Mohany and Ziada (2006) are given in figure 5.26. The lift coefficient based on the aerodynamic component is given in figure 5.25(c). It is observed to increase by a factor of 12 as the resonance progresses into the lock-in region. The lift coefficient at the onset of resonance is small. Oengoren and Ziada (1998) report similar values ranging from 0.025 to 0.06 in a parallel triangular array with a spacing

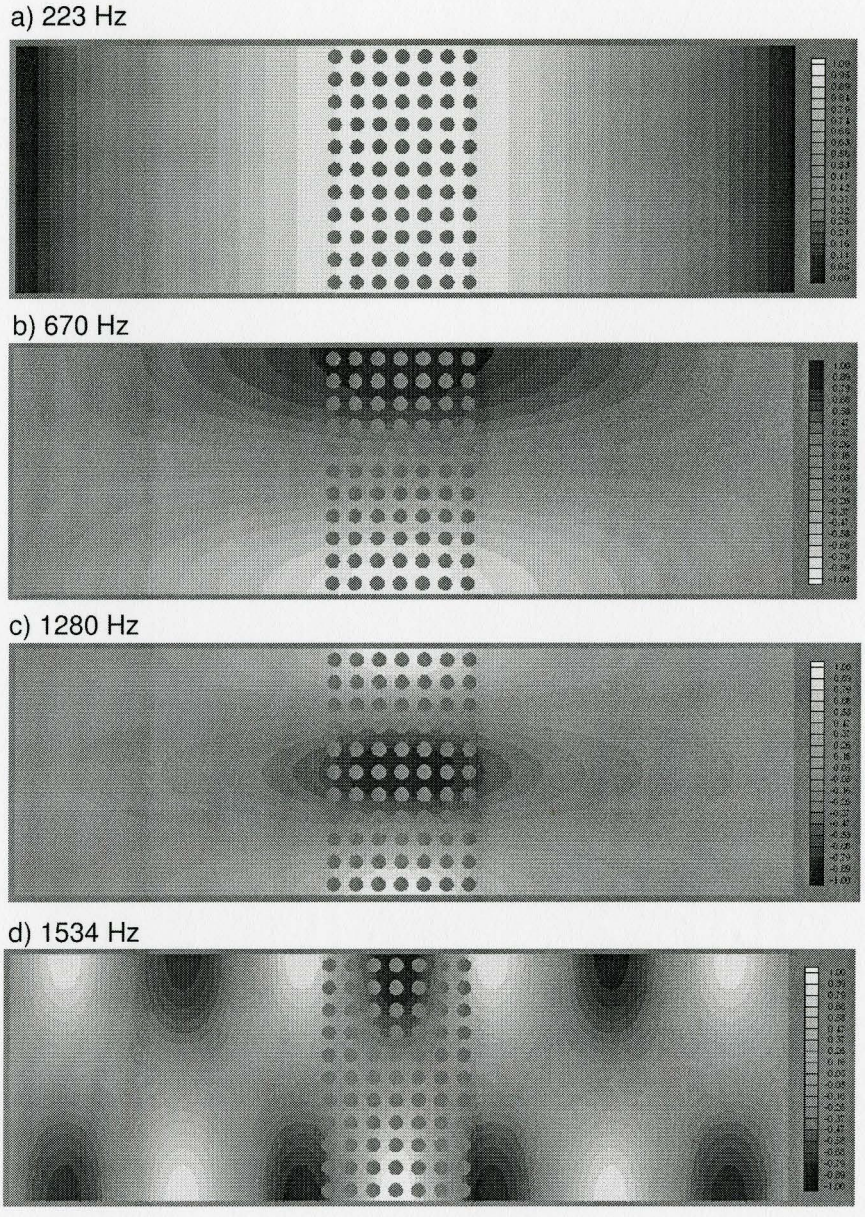

Figure 5.24: Acoustic mode shape of a longitudinal mode at 223 Hz (a), the first transverse acoustic mode at 670 Hz (b) and the second transverse acoustic mode at 1280 Hz (c) for the array with P/D = 1.58. A high frequency mode is shown in figure (d) at 1534 Hz. Note that the color bar in figure (a) is between 1 and 0, and between -1 and 1 in figure (b), (c) and (d).

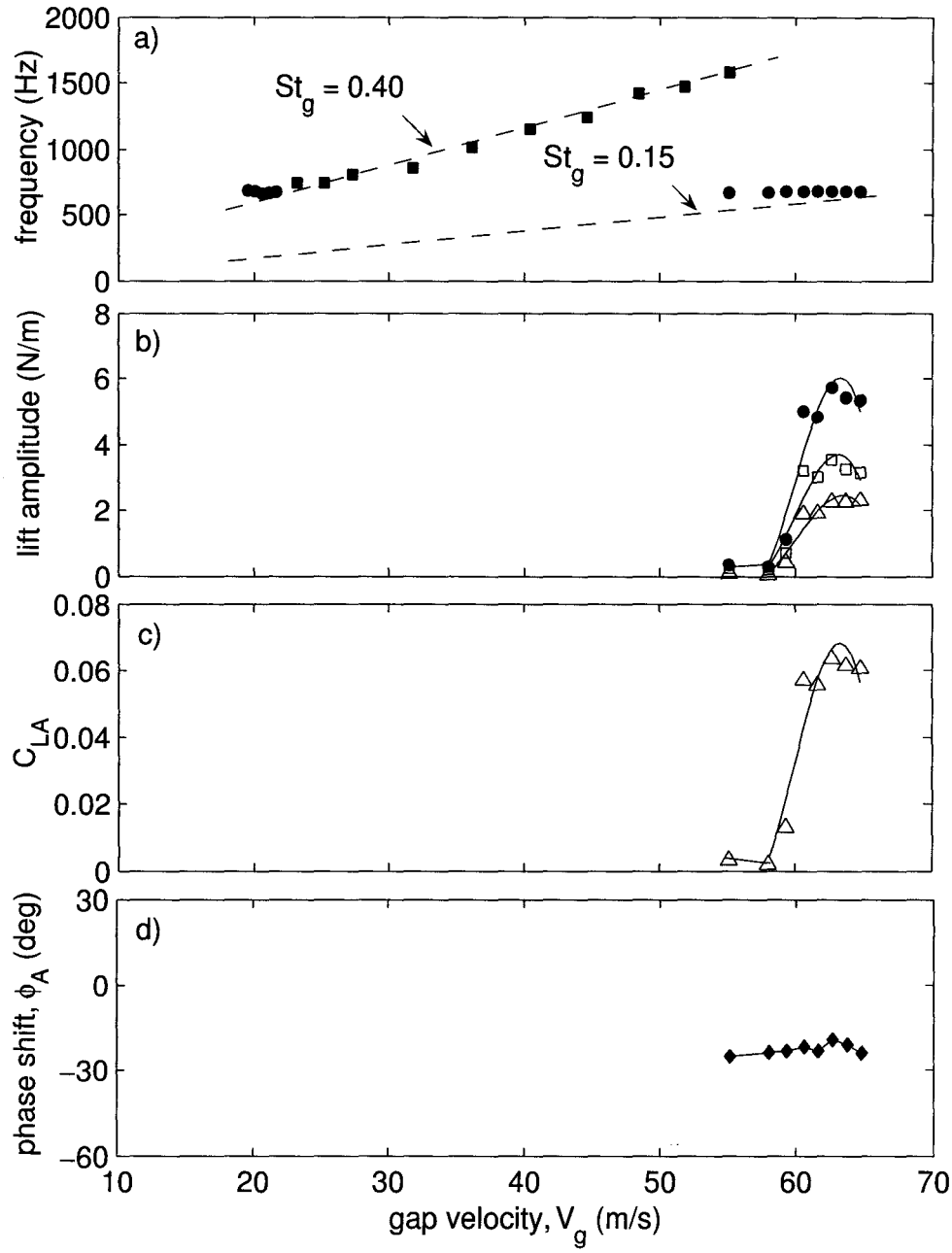

Figure 5.25: Dynamic lift response during acoustic resonance for the small spacing array with $P/D = 1.58$. The frequency response is shown in figure (a). The corresponding total dynamic lift amplitude, •, dynamic lift due to the sound field, □, and the aerodynamic lift, △, is shown in figure (b). The aerodynamic lift coefficient, C_{LA}, is shown in figure (c) using the dynamic lift forces and nomenclature from figure (b). The phase shift, ϕ_A, between the sound field and aerodynamic lift component is shown in figure (d).

ratio of 1.61. In small inline arrays, vortex shedding has been observed in the absence of acoustic resonance, however, due to the tight packing of the tubes, the highly turbulent flow exhibits vortices with very little strength as discussed in §2.4.1.

In the small tube array, only a higher flow periodicity is identified in the frequency response. Figure 5.20 shows a dashed line with a Strouhal number of 0.15 from Oengören and Ziada (1992b), and shows good agreement with the assumed pre-coincidence resonance. The results of Oengören and Ziada (1992b) for the inline tube array with a spacing ratio of $X_L/X_T = 1.75/2.25$ overlays well with the present frequency response as demonstrated in figure 5.21. Since this Strouhal number of 0.15 seems to be a reasonable assumption for the unidentified lower Strouhal number, this Strouhal number is used in the comparison of the phase shift with the frequency ratio, f_a/f_v, shown in figure 5.26 along with the results of Mohany and Ziada (2006). The present phase results, using a Strouhal number of 0.15 reported by Oengören and Ziada (1992b), show the flat phase response reported by Mohany and Ziada (2006).

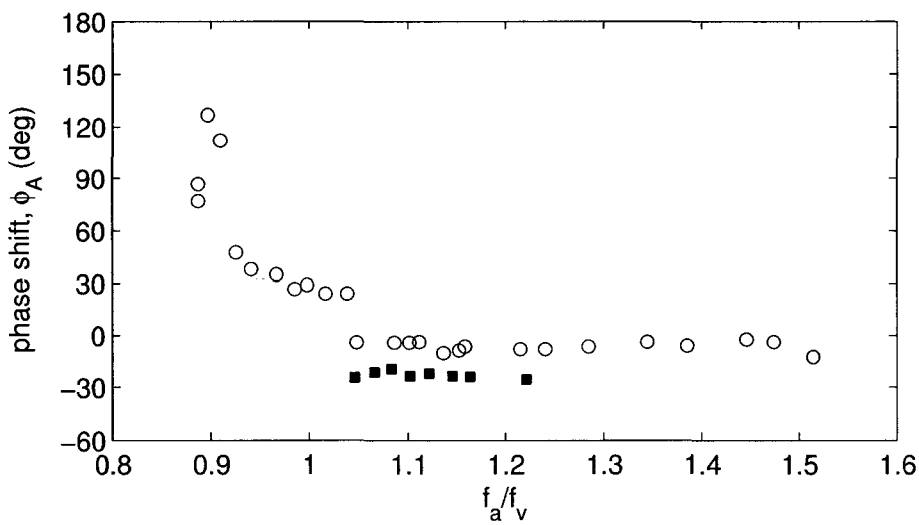

Figure 5.26: Phase shift, ϕ_A, between the aerodynamic lift force and the acoustic pressure field, for the present tube array with $P/D = 1.58$, ■, using $St_g = 0.15$. Results of Mohany and Ziada (2006) are identified by, ○.

5.4 Discussion

Acoustic resonance can cause abrupt increase in the total dynamic lift force on a tube in an array. This chapter investigated the effect of acoustic resonance on the total dynamic lift. It is shown that the total dynamic lift during flow-excited acoustic resonance is composed of an aerodynamic lift component generated by unsteady periodic flow over the cylinders and a component due to the acoustic sound field induced during resonance. The results from chapter 4 show the origin and amplitude of dynamic lift due to an acoustic pressure field. The results of chapter 4 are extended to a larger range of diameter to wavelength ratios and for several spacing ratios by means of experimentally validated numerical simulation. To increase the applicability of the present investigation, it is useful to discuss in further detail the results of chapter 4 and chapter 5.

Small and intermediate inline arrays are unique from the large spacing square array in that they typically exhibit a pre-coincidence acoustic resonance. This type of resonance, explained in §2.4.2, is characterized by an acoustic resonance occurring at flow velocities much less than that where coincidence of the natural vortex shedding frequency with the acoustic mode of the test section occurs. A key feature discovered for small and intermediate tube arrays is a small phase shift between the acoustic field and the aerodynamic lift, shown in §5.2.3.1 and §5.3.3 for the intermediate and small tube spacing arrays respectively. The small phase difference allows simple amplitude summation of the acoustic lift and aerodynamic lift to approximate the total dynamic lift during acoustic resonance with only small over-estimation of the actual total dynamic lift. As discussed earlier, from figure 5.17 and 5.25, any small phase difference will only reduce the actual total dynamic lift, thus, simple summation of amplitude will be conservative.

To determine the total dynamic lift, two things must be determined when extending the present results to other diameter ratios, or tube spacings. The first is the aerodynamic lift coefficient at velocities corresponding to the point where maximum acoustic resonance is expected. These lift coefficients are available in the present results, as well as in the literature. Weaver (1993) presents an excellent review of the literature pertaining to the topic. Once a lift coefficient is selected in the absence of acoustic resonance, an enhancement factor must be selected. A summary of the enhancement factors are given by table 5.1. During acoustic resonance the lift coefficient due to the aerodynamic lift, caused by the flow over the cylinder, increased by a factor of 12 in the small spacing array, and by a factor of 6 in the intermediate spacing array. Therefore, increasing the natural lift coefficient by a suitable factor can estimate the aerodynamic lift component during acoustic resonance.

Table 5.1: Summary of the enhancement factors of C_{LA}

Array	Class	Enhancement factor
$P/D = 3.37$	large	3
$P/D = 2.18$	intermediate	6
$P/D = 1.58$	small	12

The dynamic lift force due to the acoustic pressure field can be calculated from the results presented in chapter 4. As shown in figure 4.9, a constant ratio exists between the lift due to the acoustic pressure field calculated by the validated numerical simulation and that obtained by the sine wave distribution method. The results shown in figure 4.9 indicate that the ratio between the predictions of the two methods is constant over a wide range of $D/lambda_{1/2}$ for a given tube spacing ratio. Three tube spacing ratios were tested, $P/D = 3.37, 2.18$ and 1.58. Figure 4.10 demonstrates that the lift ratio is dependant on the spacing between the tubes. It is found that decreasing the tube spacing caused a decrease in the ratio between the lift forces

calculated from the numerical simulation and from the sine wave distribution. To estimate the lift force due to sound for a given $D/lambda_{1/2}$ and spacing ratio, a linear interpolation between the array spacings would give a good approximation of the lift due to sound. This ratio multiplied by the lift due to sine wave distribution for the array of interest would give the amplitude of the dynamic lift force per unit length for the normalized first transverse acoustic mode. Thus, the force per unit length due to the sound field on the tube is realized by multiplying this new factor by the maximum sound pressure amplitude in Pascals.

To determine the dynamic lift force due to sound, the maximum sound pressure level is required. Blevins and Bressler (1993) presents estimates of the maximum sound pressure level shown in equation 5.1, where V_g is the gap velocity, C is the speed of sound in the array and Δp is the pressure drop across the tube array. Also, Blevins and Bressler (1993) show maps of the maximum sound pressure levels predicted for various tube arrays. This equation, and the sound pressure level maps only estimate the maximum sound pressure level and therefore a factor of safety is required to ensure conservative design. The maximum sound pressure level achieved during acoustic resonance is dependant on the level of acoustic damping in the system and can vary between different boilers and heat exchangers. Therefore, the lift due to the sound field should be chosen conservatively.

$$SPL_{\max} = 12.5\frac{V_g}{C}\Delta p \tag{5.1}$$

To summarize, the total dynamic lift amplitude can be calculated by summing the aerodynamic lift and the acoustic dynamic lift. For the large spacing inline array, these values cannot be added directly due to the phase relationship shown by figure 5.7. Acoustic resonance occurs due to excitation of the acoustic mode by observed Strouhal numbers in the flow. The mechanism is essentially different from

that of the small and intermediate spacing arrays. For the large spacing array, the phase difference between the aerodynamic lift and the sound field is non-zero, and varies with flow velocity. Thus, a different approach is needed to the estimate of the total dynamic lift.

For the large array, the aerodynamic lift force per unit length, due to the flow over the tubes, can be calculated similarly as discussed for the small and intermediate spacing ratios. The ratio between the lift coefficient during acoustic resonance and in the absence of resonance is approximately 3, as show in figure 5.7(d). The lift due to the acoustic pressure field can be calculated using the method discussed for the small and intermediate spacing arrays. Predicting the sum of these two components requires more consideration.

During acoustic resonance, using the ratio of the calculated aerodynamic lift and the lift due to the acoustic pressure field can aid in choosing a method to combine the results. If a large factor exists between the amplitude of the two results, direct addition will predict the total dynamic lift rather well with some conservatism. If the results are with comparable magnitude, it would be necessary to know the phase shift, as shown in figure 5.8, to determine a good approximation of maximum total dynamic lift amplitude. Experimental results for a wide range of heat exchangers and boilers are limited, therefore detailed measurements of the phase relationships are also limited. A foreknowledge of the natural Strouhal number and acoustic mode frequency can allow comparison with figure 5.8 to determined the approximate phase shift necessary to complete the vector addition of the results. Simple amplitude summation of the aerodynamic lift and the acoustic lift forces will give a conservative total dynamic lift estimate during acoustic resonance.

Chapter 6

Conclusions

Dynamic lift on a central tube in a square tube array with three different pitch ratios, $P/D = 3.37$, 2.18 and 1.58 is investigated during flow-excited acoustic resonance. The dynamic lift is found to consist of two components. The first is an aerodynamic lift component, generated by the unsteady periodic flow though the tube array. This component exists before the onset of resonance, but is enhanced by the sound field when acoustic resonance is initiated. The second component of the total dynamic lift during flow-excited acoustic resonance is due to the acoustic pressure field that occurs during resonance.

Numerical simulations of the acoustic pressure distributions, in the absence of flow, show that the ratio of the dynamic lift amplitude produces a constant ratio when compared with the sine wave distribution for a given tube array. The significance of this result is that since this ratio is now known for the square tube arrays, a simple calculation of the lift amplitude can be determined from the sine wave distribution and multiplied by the ratio to yield the actual dynamic lift due to the acoustic pressure field at a given level.

For the large square array, a classical Strouhal excited acoustic resonance is observed, wherein resonance occurs at coincidence of the vortex shedding frequency and the acoustic mode. In this case the phase shift between the aerodynamic lift and the sound field can increase up to 130 degrees. For the small and intermediate spacing square arrays, the mechanism of acoustic resonance is inherently different from that

observed for the large spacing array. For the small and intermediate spacing arrays, pre-coincidence acoustic resonance is observed. During pre-coincidence resonance, the phase shift between the aerodynamic lift and the sound field is small. These two mechanisms of acoustic resonance, coincidence and pre-coincidence, require specific considerations for determining the total dynamic lift.

A method to obtain conservative estimates of the total dynamic lift during acoustic resonance is presented at the end of chapter 5. For the small and intermediate spacing arrays, the direct summation of the calculated magnitudes of the enhanced aerodynamic and sound dynamic lift components yields a slightly conservative estimate of the total dynamic lift during resonance. For the large spacing array, direct summation of the magnitudes of these components may yield a result that is overly conservative due to the large phase shift. The degree of conservatism is dependant on the ratio of magnitudes of two dynamic lift components. With a foreknowledge of the Strouhal number and acoustic mode frequency, it is possible to estimate the phase shift thereby determine more accurate estimates. It should be noted that a factor of safely should be chosen to cover the uncertainty in the sound pressure levels and the ratio of aerodynamic lift enhancement during acoustic resonance.

References

Axisa, F., Antunes, J., Villard, B., & Wullschleger, M. 1988, Random excitation of heat exchanger tubes by cross-flow. Chicago, IL, USA, pp. 23 – 46.

Baylac, G., Bai, D., & Gregoire, J. P. 1973, Study of flow and acoustic phenomena in a tube-bank. Modern Concrete, 36 – 42.

Bearman, P. & Wadcock, A. 1973, The interaction between a pair of circular cylinders normal to a stream. Journal of Fluid Mechanics, 61, 499 – 511.

Bishop, A. 1964, A review of vortex streets, periodic wakes and induced vibration phenomena. Proceedings of the Royal Society of London. Series A, Mathematical and Physical Sciences *277*(1368), 51 – 75.

Blake, W. 1986. *Mechanics of Flow-induced Sound and Vibration.* Acedemic Press, New York.

Blevins, R. 1985, The effect of sound on vortex shedding from cylinders. Journal of Fluid Mechanics, 161, 217 – 237.

Blevins, R. 1990. *Flow-Induced Vibration (Second Edition).* Van Nostrand Reinhold, New York.

Blevins, R. & Bressler, M. 1987, Acoustic resonance in heat exchanger tube bundles. ii. prediction and suppression of resonance. Transactions of the ASME. Journal of Pressure Vessel Technology *109*(3), 283 – 8.

Blevins, R. & Bressler, M. 1993, Experiments on acoustic resonance in heat exchanger tube bundles. Journal of Sound and Vibration *164*(3), 502 – 534.

Carberry, J., Sheridan, J., & Rockwell, D. 2001, Forces and wake modes of an oscillating cylinder. Journal of Fluids and Structures, 15, 523 – 532.

Chen, S. S. & Jendrzejczyk, J. A. 1987, Fluid excitation forces acting on a square tube array. Journal of Fluids Engineering, Transactions of the ASME *109*(4), 415 – 423.

Chen, Y. 1968, Flow-induced vibration and noise in tube banks of heat exchangers due to von karman streets. ASME Journal of Engineering for Industry, 90, 134 146.

Curle, N. 1955, The influence of solid boundaries upon aerodynamic sound. Proceedings of the Royal Society of London *231*(series A), 505 – 514.

Eisinger, F. 1980, Prevention and cure of flow-induced vibration problems in tubular heat exchangers. Transactions of the ASME. Journal of Pressure Vessel Technology *102*(2), 138 – 45.

Etkin, B., Korbacher, G., & Keefe, R. 1957, Acoustic radiation from a stationary cylinder in a fluid stream (aeolian tones). The Journal of the Acoustical Society of America, 29, 30 – 36.

Feenstra, P., Weaver, D., & Eisinger, F. 2005, Acoustic resonance in a staggered tube array: Tube response and the effect of baffles. Journal of Fluids and Structures, 21, 89 – 101.

Fitz-Hugh, J. 1973, Flow-induced vibration in heat exchangers. In *Intl. Symp. on Vibration Problems in Industry*, Number 427, Keswick, England, UK, pp. 1 – 17. Atomic Energy Authority, Windscale and Natl. Physical Lab.

Fitzpatrick, J. & Donaldson, I. 1977, A preliminary study of flow and acoustic phenomena in tube banks. ASME Journal of Fluids Engineering, 99, 681 – 686.

Fitzpatrick, J. A. 1985, Prediction of flow-induced noise in heat exchanger tube arrays. Journal of Sound and Vibration *99*(3), 425 – 435.

Gerrard, J. 1961, An experimental investigation of the oscillating lift and drag of a circular cylinder shedding turbulent vorticies. Journal of Fluid Mechanics, 2, 244 – 256.

Grotz, B. & Arnold, F. 1956. Flow induced vibration in heat exchangers. Department of Mechanical Engineering Technical Report 31, Stanford University.

Hall, J., Ziada, S., & Weaver, D. 2003, Vortex-shedding from single and tandem cylinders in the presence of applied sound. Journal of Fluids and Structures *18*(6), 741 – 758.

Hanson, R., Mohany, A., & Ziada, S. 2006, Flow excited acoustic resonance of two side-by-side cylinders in cross flow. ASME PVP, Vancouver.

Igarashi, T. 1981, Characteristics of the flow around two circular cylinders arranged in tandem - 1. Bulletin of the JSME *24*(188), 323 – 331.

Inada, F., Yoneda, K., Yasuo, A., & Nishihara, T. 2007, A study on fluid excitation forces acting on a rotated square tube bundle of 7/d=3.1 in cross-flow. Journal of Pressure Vessel Technology, Transactions of the ASME *129*(1), 162 – 168.

Kim, H. & Durbin, P. 1988, Investigation of the flow between a pair of circular cylinders in the flopping regime. Journal of Fluid Mechanics, 196, 431 – 48.

Kinsler, L., Frey, A., Coppens, A., & Sanders, J. 2000. *Fundamentals of Acoustics (Fourth Edition)*. John Wiley and Sons, Inc.

Koopmann, G. H. 1967, The vortex wakes of vibrating cylinders at low Reynolds numbers. Journal of Fluid Mechanics, 28, 501 – 512.

Lienhard, J. 1966, The synopsis of lift, drag and vortex frequency for rigid circular cylinders. Washington State Univeristy Bullenton, 300.

Zdravkovich, M. 1985, The effects of interference between circular cylinders in cross-flow. Journal of Fluids and Structures, 1, 239 – 261.

Ziada, S. 2006, Vorticity shedding and acoustic resonance in tube bundles. Journal of the Brazilian Society of Mechanical Sciences and Engineering *28*(2), 186 – 199.

Ziada, S. & Oengören, A. 1990, flow-induced acoustical resonance of in-line tube bundles. Sulzer Technical Review, 1, 45 47.

Ziada, S. & Oengören, A. 1993, Vortex shedding in an in-line tube bundle with large tube spacings. Journal of Fluids and Structures, 7, 661 – 687.

Ziada, S. & Oengören, A. 2000, Flow periodicity and acoustic resonance in parallel triangle tube bundles. Journal of Fluids and Structures *14*(2), 197 – 219.

Ziada, S., Oengören, A., & Bühlmann, E. 1989, On acoustical resonance in tube arrays: Part i. experiments. Journal of Fluids and Structures, 3, 293 – 314.

Zukauskas, A. & Katinas, V. 1980, Flow-induced vibration in heat exchanger tube banks. Proceedings of the IUTAM-IAHG Symposium on Practical Experiences with Flow-Induced Vibrations, 188 – 196.